

Investigation of Magneto-Electric Rectification at the Molecular Level

by

Gregory Smail

A dissertation submitted in partial fulfillment
of the requirements for the degree of
Doctor of Philosophy
(Applied Physics)
in the University of Michigan
2023

Doctoral Committee:

Professor Stephen Rand, Chair
Professor Pallab Bhattacharya
Professor Anthony Grbic
Professor Karl Krushelnick
Dr. John Whitaker

Gregory Smail

smail@umich.edu

ORCID iD: [0000-0002-4673-7927](https://orcid.org/0000-0002-4673-7927)

© Gregory Smail 2023

DEDICATION

To my family: Mom, Dad, Irene, and Ben
And also Cinnamon, Charlotte, and Margaret
And most of all
To Mackenzie

ACKNOWLEDGMENTS

First, I would like to thank my advisor, Professor Stephen Rand. From day one, he has been my advocate and has helped me realize my potential as a researcher and a scientist. The fact that I have found my graduate school experience to be so rewarding is a testament to his scientific enthusiasm and insight. I am also grateful to my committee, Professor Pallab Bhattacharya, Professor Anthony Grbic, Professor Karl Krushelnick, and Dr. John Whitaker for their mentorship and assistance in refining my thesis. I have been fortunate to do my research at an institution like the University of Michigan where such talented researchers can be found. In particular, I have worked closely with Dr. Whitaker during the course of my thesis research and his assistance and advice throughout have been invaluable. To this list of mentors I also want to add Professor Herbert Winful and John Nees. Both have taken the time to provide helpful feedback and suggestions, and for that I am grateful.

A graduate student does not get far without the support of their colleagues. Luckily, my colleagues have been amazing. Tuan, Krish, and Ayesheshim took me under their collective wing when I joined the Rand lab and have been excellent role models. Long has always been around when I have had a question or needed to bounce an idea off of somebody. Laura and I shared an office, and her friendship has meant a great deal to me (although sometimes I wish she had left her coffee machine behind after she graduated!).

The administrative staff at CUOS have also been wonderful. Amy, Car, and Gaylene have put in so much work to make sure that I and the other students in optics can focus on their research without worrying about the nuts and bolts of the operation, and that has been a great relief. I also want to thank the Applied Physics program for their support.

I could not have done this without my friends and family. My parents, Dan and Kathleen, raised me to be curious about the world and have supported me as I have followed that curiosity to its logical extent. I have looked up to my siblings Ben and Irene my whole life and they have always guided me well. I am deeply thankful to my entire family for helping me get this far. My friends - including Sonya, Joey, Addison, Andrea, Jeff, Alex, Josh, Nick, among others - have been there for me when I have needed support, encouragement, or anything else. I should also mention my cats, Cinnamon, Charlotte, and Margaret. Though frequently mischievous, few things can cheer you up better after a bad day than a fluffy pet.

More than anything, I want to thank my wife, Mackenzie. She has been a true partner to me. I would not be where I am today without her unconditional love and support, through the good times and the bad.

PREFACE

Some of the work in this thesis were performed in collaboration with other researchers. The classical theory in Chapter 2 was originally developed by previous members of the group and collaborators, including W.M Fisher, A.A. Fisher, P.M. Anisimov, and E.F.C Dreyer. The quantum theory and theoretical analysis of the rectification moment was done by me. The classical model described in Chapter 3 was originally developed by E.F.C Dreyer and was modified by me to perform simulations of pulsed excitation. The quantum model was my work alone. The second harmonic generation experiment in Chapter 3 was performed in collaboration with M.T Trinh, K. Makhal, and D.S. Yang. The experimental setup was built by M.T. Trinh and K. Makhal, while the sample was fabricated by D.S. Yang. Alignment, data collection, and analysis was shared between M.T Trinh and myself. The birefringence experimental setup and theory was done by me. Analysis of the experimental results in Chapter 4 was shared between M.T Trinh and myself, while Sections 4.2 and 4.3 on the computational results are exclusively my analysis.

Some of the work in this thesis has been previously published. The classical computational model described in Chapter 3 was published in "Optical magnetization, part III: theory of molecular magneto-electric rectification" (1). The second harmonic generation experiment and results from Chapters 3 and 4 were published in "Observation of magneto-electric rectification at non-relativistic intensities" (2).

TABLE OF CONTENTS

DEDICATION	ii
ACKNOWLEDGMENTS	iii
PREFACE	v
LIST OF FIGURES	viii
LIST OF TABLES	xiii
LIST OF APPENDICES	xiv
ABSTRACT	xv
CHAPTER	
1 Introduction	1
1.1 Background	3
1.1.1 Relativistic Magnetic Effects	3
1.1.2 Magnetic Materials at Optical Frequencies	4
1.1.3 Linear M-E Interactions	5
1.1.4 Metamaterials	6
1.1.5 Ultrafast Demagnetization	7
1.2 Previous Work on M-E Nonlinearities	8
2 Theory	14
2.1 Classical Coupled Oscillator Model of M-E Interactions	14
2.1.1 Electron Oscillator in a Magnetic Field	15
2.1.2 Coupling to a Rigid Rotor Model of a Molecule	18
2.2 Density Matrix Model of M-E Interactions	20
2.2.1 Three Level Model of M-E Interactions	20
2.2.2 Density Matrix Analysis	21
2.3 Theoretical Form of the Rectification Nonlinearity	29
3 Methods	32
3.1 Second Harmonic Generation Induced by M-E Rectification	32
3.1.1 Crossed Beam Pump-Probe Geometry	33

3.1.2	Pulse-Front Tilt for Temporal Resolution	34
3.1.3	Experimental Setup	35
3.1.4	Alignment of the Experimental Setup	37
3.1.5	Isolating the M-E SHG Signal	38
3.2	Birefringence Induced by M-E Rectification	40
3.2.1	Theory of M-E Induced Birefringence	41
3.2.2	Experimental Setup	43
3.2.3	Alignment of the Experimental Setup	44
3.2.4	Calibration of the Experimental Setup	45
3.2.5	Isolation of the M-E Induced Birefringence	48
3.3	Computer Simulations of M-E Rectification	50
3.3.1	Classical Model of M-E Rectification	51
3.3.2	Density Matrix Model of M-E Rectification	53
4	Results	55
4.1	SHG Experiment	55
4.1.1	Sample Properties	55
4.1.2	Observation of M-E Induced Second Harmonic Generation	56
4.2	Time Dependence from the Coupled Oscillator Simulations	61
4.3	Time Dependence from the Density Matrix Simulations	67
4.4	Comparison of Simulation Results	73
5	Conclusion	78
5.1	Summary of Results	78
5.2	Future Work	81
5.2.1	Ultrafast Photonic Switching at Right Angles	82
5.2.2	Terahertz Generation	82
5.2.3	Energy Conversion in Insulators	83
	APPENDICES	85
	BIBLIOGRAPHY	101

LIST OF FIGURES

FIGURE

1.1	Plot of simulated electron position in y vs x as it is accelerated by an intense laser source. The color axis shows electron energy. Reprinted from Ref. (12).	4
1.2	Measured transmission of a probe beam through a sample versus the time duration of a driving pulse. The black line was generated by a numerical simulation of the populations of ground and excited state. Reprinted from Ref. (17).	5
1.3	Diagram of (a) circular and (b) rectangular split ring resonators. Reprinted from Ref. (30).	7
1.4	Intensity of magnetic dipole scattered light plotted vs input intensity. The black data points show the magnitude of the magnetic dipole scattered light, while white data points show the ratio in intensity between magnetic scattered light and electric scattered light. Reprinted from Ref. (43).	9
1.5	Scattering data for gadolinium gallium garnet. (a) Intensity of magnetic dipole scattered light plotted vs incident polarization. The black data points show the magnitude of the magnetic dipole scattered light, while white data points show the magnitude of the electric dipole scattered light. Dashed circles show fits to the unpolarized contribution to the scattering intensity while solid lines show $\sin^2(\theta)$ fits to the polarized contribution. The residuals show that this combination of unpolarized scattering and dipole scattering is an excellent fit to the data. (b) Intensity of the unpolarized electric dipole (white) and magnetic dipole (black) scattered light versus incident optical intensity. Inset: plot of polarized electric dipole and magnetic dipole scattering versus incident intensity. Reprinted from Ref. (48).	10
1.6	Longitudinal polarization moment versus time generated by a classical model of M-E nonlinearities. (a) Output when $\frac{I_{\perp}}{I_{\parallel}} = 1$. (b) Output when $\frac{I_{\perp}}{I_{\parallel}} = 1000$. Reprinted from Ref. (1).	11
1.7	Normalized spectra of scattered light arise from electric dipole (red) and magnetic dipole (blue) scattering. The differences between the electric dipole and magnetic dipole spectra are shown in the black curve. Transition frequencies of rotational and vibrational features are shown by the green and red bars respectively. Inset: the electric dipole spectrum overlaid with the laser spectrum. Reprinted from Ref. (52).	12
2.1	Classical electron oscillator. The electron, in red, is attached to a static restoring point by a spring-like force and excited by an electromagnetic field.	15
2.2	Rigid rotor model of a diatomic molecule. The time evolution of angles θ_{\perp} and θ_{\parallel} describe the rotational motion of the molecule.	18

2.3	Coupled oscillator model of M-E nonlinearities. The restoring point of the electron oscillator is attached to the rigid rotor model. The electron motion induced by the incident field drives molecular rotations.	20
2.4	Diagram of the three-state quantum model of a molecular system. ω_ϕ is equal to the molecular rotational frequency ω_{13}	22
3.1	Diagram of the co-linear (a) and crossed beam (b) geometries. The pump beam is shown in red and the probe beam is shown in blue. The plane of polarization of the pump and probe are shown by the red and blue planes respectively.	34
3.2	Use of tilted pulse fronts to improve temporal resolution (a) Plot of the SFG intensity as a function of relative delay between pump and probe beams. Diagram of the pump-probe interaction when pulse fronts are (b) flat, (c) tilted by 45° , or (d) tilted by -45° . The experiment uses case (c) to maximize the temporal resolution. Reprinted from Ref. (2).	35
3.3	Experimental setup for the SHG experiment. The pulse front of the beam is tilted and then passes through a beamsplitter to generate the pump and probe beams. The pump beam is chopped and sent through an adjustable delay stage before it travels to the sample. After the probe beam passes through the sample, light at the laser wavelength of 800 nm is filtered out and the remaining light at the second harmonic wavelength of 400nm is collected by the PMT.	37
3.4	Experiment setup for alignment of the SHG setup. Second harmonic radiation is generated at the surface of the gallium arsenide wafer when the pump and probe beams spatially and temporally overlap. The second harmonic light is radiated perpendicular to the sample surface, where is it sent to the PMT for measurement.	38
3.5	Geometry of the pump-probe interaction at the pentacene thin film sample. The lab axes are shown in the bottom right. The pump travels along the \hat{z} direction while the probe travels along the \hat{x} direction. The probe is polarized at an angle α from the \hat{y} axis.	39
3.6	Concept of the M-E induced birefringence experiment. The probe beam is linearly polarized at 45° by the first $\lambda/2$ waveplate. The presence of the M-E rectification field in the sample modifies the probe polarization state by adding ellipticity. The $\lambda/4$ waveplate converts this ellipticity into a linear polarization rotation. The horizontal and vertical components of the pump beam are separated and the difference in power between them is measured.	43
3.7	Diagram of the experimental setup for the M-E induced birefringence experiment. After passing through the sample, the probe beam was focused into a polarization maintaining fiber (PMF) which was coupled into an in-line polarized beamsplitter. The two polarization components then travelled through 1 m of PMF to the two input ports of the balanced photodetector and the amplified difference between the photocurrent generated in each port is sent to the lock-in amplifier.	44
3.8	Diagram of the two-photon alignment setup. The pump and probe beam temporally and spatially overlap in the Rhodamine 6G solution in methanol. The pump output port is used to collect the two-photon fluorescence (shown by green arrows). The pump beam at 800 nm is filtered out by a narrow band pass filter centered at the fluorescence wavelength.	45

3.9	Concept of the calibration setup. The experimental setup is shown on top while the modifications made for calibration are shown on the bottom. For a pump-induced phase delay in the experimental sample of δ , the lock in voltage signal will be proportional to $\sin(\delta)$. Replacing the sample and the $\lambda/4$ waveplate with a second $\lambda/2$ waveplate at an angle α from 22.5° results in a voltage signal proportional to $\sin(4\alpha)$.	46
3.10	Plot of the voltage signal from the lock-in amplifier as a function of the angle of the second $\lambda/2$ waveplate. The experimental data is shown in black, while a linear fit $ax + b$ is shown in red with fitting parameters $a = -1.57 \cdot 10^{-3}$ and $b = 1.9 \cdot 10^{-7}$. A linear fit is appropriate given the small angles involved. The error bars on the experimental data correspond to the X_{noise} value calculated by the lock-in amp.	48
3.11	Sensitivity of the signal to direction of polarization rotation. If phase delay is accumulated on the \hat{x} -polarized component of the probe beam as shown on the left, the polarization will undergo clockwise rotation. For phase delay that accumulates on the \hat{z} -polarized component of the probe, the polarization is rotated in a counterclockwise direction	50
3.12	Stability of the classical model for pulsed excitation for 100 fs (black) pulses and 200 fs (red) pulses. For values of the ratio $\frac{I_{\perp}}{I_{\parallel}}$ below 20, the residual energy in the system rises sharply. For larger values of $\frac{I_{\perp}}{I_{\parallel}}$, the residual energy levels off at a low value.	52
4.1	(a) AFM height image of the 400 nm thick pentacene film deposited on glass. The scan size is $5 \times 5 \mu\text{m}^2$ and the scale bar in the image corresponds to $1 \mu\text{m}$. The individual crystallites have a size between 100 nm and 200nm. (b) The absorption spectrum of the sample. The absorption of the sample is very low at the laser wavelength of 800 nm, and relatively low at the second harmonic wavelength of 400 nm.	56
4.2	(a) Intensity of second harmonic radiation versus delay time between pump and probe beams. There are two distinct components: the static background SSHG and the pump-induced signal Δ SHG. The black curve shows a convolution of the simulated M-E rectification field using the classical model and the instrumental response. (b) Intensity of the static background versus probe beam power.	58
4.3	Dependence of the second harmonic radiation on probe polarization. (a) Intensity of second harmonic radiation versus delay time for different probe polarization angles. The angles for the red, blue, and black curves were $\alpha = 90^\circ$, $\alpha = 40^\circ$, and $\alpha = 0^\circ$. (b) Peak second harmonic radiation intensity versus the probe polarization angle α . The red and blue data points show the peak experimental signal for the pump-induced signal and the static background respectively. The red and blue dashed lines show a $\sin^2(\alpha)$ fit to the pump-induced signal and a $\sin^4(\alpha)$ fit to the background signal.	59
4.4	Dependence of the second harmonic radiation on the pump beam. The red data points show experimental data. (a) Peak second harmonic radiation intensity versus pump power. The red dashed line shows a quadratic fit to the data. (b) Peak second harmonic radiation versus pump polarization angle.	61
4.5	Evolution of charge separation (red curve) versus time in the coupled oscillator model when driven by a 100 fs excitation pulse (gray curve). Each curve was individually normalized. All parameters were set to the values specified in Table 4.1.	62

4.6	Coupled oscillator model simulations of charge separation versus time for different values of the electronic damping rate γ_e . Rates for the blue (dashed), black (solid), and red (dotted) curves were $\gamma = 0.015\omega_0$, $\gamma = 0.15\omega_0$, and $\gamma = 0.5\omega_0$ respectively. All parameters except γ_e were set to the values specified in Table 4.1. Each curve was individually normalized.	63
4.7	Peak magnitude of the rectification moment versus the electronic damping rate γ_e . All parameters except γ_e were set to the values specified in Table 4.1.	64
4.8	Coupled oscillator model simulations of the charge separation field versus time for different values of rotational damping rate γ_m . Frequencies for the black, red, and yellow curves were $\gamma_m = 0.05\omega_m$, $\gamma_m = 0.1\omega_m$, and $\gamma_m = 0.5\omega_m$, respectively. All parameters except γ_m were set to the values specified in Table 4.1. Each curve was individually normalized.	64
4.9	Coupled oscillator model simulations of the charge separation field versus time for different values of rotation frequency ω_m . Frequencies for the blue (dashed), black (solid), and red (dotted) curves were $\omega_m = 5 \cdot 10^{-5}\omega_0$, $\omega_m = 5 \cdot 10^{-3}\omega_0$, and $\omega_m = 1 \cdot 10^{-2}\omega_0$, respectively. All parameters except ω_m were set to the values specified in Table 4.1. Each curve was normalized to the dashed blue curve	65
4.10	Peak value of the rectification moment versus molecular rotational frequency. All parameters except ω_m were set to the values specified in Table 4.1.	66
4.11	Magnitude of the rectification dipole moment versus detuning for different values of τ_p . The steady-state response is also shown for comparison. All parameters except τ_p and ω were set to the values specified in Table 4.1.	66
4.12	Evolution of charge separation versus time in the density matrix model when driven by a 100 fs excitation pulse. All parameters were set to the values specified in Table 4.2.	68
4.13	Peak magnitude of charge separation versus the decoherence rate Γ_{12} in the density matrix model. All parameters other than Γ_{12} were set to the values specified in Table 4.2.	69
4.14	Evolution of charge separation versus time in the density matrix model for different values of the decoherence rate Γ_{13} . Decoherence rates for the black, red, and yellow curves were $\Gamma_{13} = 5 \cdot 10^{11}$ rad/s, $\Gamma_{13} = 1 \cdot 10^{12}$ rad/s, and $\Gamma_{13} = 5 \cdot 10^{12}$ rad/s respectively. All parameters other than Γ_{13} were set to the values specified in Table 4.2. Each curve was individually normalized.	70
4.15	Evolution of charge separation versus time in the density matrix model for different values of the rotational frequency ω_{13} . Decoherence rates for the black, red, and yellow curves were $\omega_{13} = 0.26$ GHz, $\omega_{13} = 3.9$ GHz, and $\omega_{13} = 13$ GHz respectively. All parameters other than ω_{13} were set to the values specified in Table 4.2. Each curve was individually normalized.	71
4.16	Peak magnitude of charge separation versus the detuning Δ_{12}/ω_{12} . All parameters other than ω were set to the values specified in Table 4.2.	71
4.17	Evolution of charge separation versus time in the density matrix model for different pulse widths τ_p . The pulse widths for the black, red, and yellow curves were $\tau_p = 40$ fs, $\tau_p = 100$ fs, and $\tau_p = 250$ fs respectively. All parameters other than τ_p were set to the values specified in Table 4.2. Each curve was individually normalized.	72

4.18	Evolution of charge separation versus time in the density matrix model for steady state excitation. All parameters were set to the values specified in Table 4.2. The driving field was assumed to be $V(t) = -\frac{\hbar\Omega}{2}e^{i\omega(t-t_0)}$	73
4.19	Comparison between the coupled oscillator and density matrix model predicts for the rectification field. All parameters were set to the values specified in Tables 4.1 and 4.2 except for $\Gamma_{13} = 7 \cdot 10^{12}$ rad/s.	76
4.20	Evolution of charge separation versus time in the density matrix model for steady state excitation. All parameters were set to the values specified in Table 4.2 except for $\Gamma_{13} = 7 \cdot 10^{12}$ rad/s. The driving field was assumed to be $V(t) = -\frac{\hbar\Omega}{2}e^{i\omega(t-t_0)}$	77
5.1	Simulated rectification moment from coupled oscillator model. Inset: Frequency composition of the rectification signal obtained via a Fast Fourier Transform.	83

LIST OF TABLES

TABLE

4.1	Standard input parameters for the coupled oscillator model.	62
4.2	Standard input parameters for the density matrix model.	68
4.3	Analogous parameters between the coupled oscillator and density matrix models. . . .	74

LIST OF APPENDICES

A Calculation of M-E Induced Birefringence	85
B Coupled Oscillator Model	88
C Density Matrix Model	97
D Effects of the Different Form of Coupled Oscillator and Density Matrix Models . . .	99

ABSTRACT

The role of the optical magnetic field in light-matter interactions is often neglected due to its relative weakness with respect to the optical electric field. However, the magnetic field of light can interact strongly with matter in magneto-electric interactions where it acts jointly with the optical electric field to drive optical nonlinearities. The inclusion of the magnetic field dynamically breaks parity-time symmetry, so magneto-electric interactions can take place even in materials where static symmetry prohibits all-electric second order interactions. This thesis further advances the understanding of these magneto-electric nonlinearities, with a focus on magneto-electric rectification.

Experimental and computational methods were used to characterize the magneto-electric rectification moment. The first experimental observation of magneto-electric rectification is reported. Time-resolved pump-probe experiments show a strong, ultrafast pump-induced second harmonic radiation signal in a sample with inversion symmetry. It is shown that magneto-electric rectification is the only process that is consistent with the experimental results. The design of a second experiment based on measuring magneto-electric rectification induced birefringence is presented that would offer improved sensitivity and permit a measurement of the magnitude of the rectification field.

A classical model of magneto-electric interactions is used to simulate the magneto-electric response of a material to an optical pulse. The role of two enhancement mechanisms, parametric resonance and molecular torque, are analyzed in detail. These enhancement mechanisms allow the observation of nonlinear relativistic magnetic effects at non-relativistic intensities. A generalized time-dependent density matrix theory is presented that predicts the intensity, frequency, and polarization dependence of the rectification effect. This quantum theory is used to create a second computational model of magneto-electric rectification. Simulation results of the predicted rectification magnitude from both the classical and quantum models are presented and discussed. Both models predict an ultrafast timescale for the rectification moment and show the dependence of the duration and magnitude of the simulation output on molecular properties. The temporal characteristics predicted by the models are in excellent agreement with the experimentally observed rectification signal.

The results presented in this thesis show the first experimental observation of magneto-electric

rectification as well as the first computational analysis of the temporal characteristics of the rectification moment. Future research into magneto-electric nonlinearities could provide direct measurements of the magnitude of the rectification field. This measurement could be accomplished by using the induced birefringence experimental design. Applications of this work include ultrafast all-optical switching, new methods of terahertz generation, and energy conversion.

CHAPTER 1

Introduction

There is considerable interest in interactions between the optical magnetic field and matter. If the magnetization or permeability of a material could be controlled by an optical field to the same extent that polarization can be controlled, that control could be used in applications such as negative index materials [3; 4], optical cloaking [5], superlenses [6; 7], and negative refraction [8]. There are however two inherent limitations in nature that have prevented these applications from being universally realized. The first is that the optical magnetic field is much weaker than the optical electric field. For a plane wave in vacuum, the magnitude of the optical magnetic field is related to the magnitude of the optical electric field by the equation

$$|B_0| = \frac{k}{\omega}|E_0| \quad (1.1)$$

Given the dispersion relation $k = \frac{\omega}{c}$, it can be seen that the magnitude of the optical magnetic field is a factor of the speed of light smaller than the optical electric field. On its own, this perhaps could be overcome - electric field interactions with matter can be greatly enhanced if the frequency of the optical field is close to an electronic resonance frequency in the material. However, the second limitation is that the resonance frequencies for magnetic transitions are almost exclusively found in the microwave region of the spectrum. Thus the responsibility for inducing strong magnetic interactions with matter falls to the creativity of scientists. One method of doing so is through the use of nonlinear magneto-electric (M-E) interactions mediated by the Lorentz force. These nonlinearities are driven jointly by the optical electric and magnetic fields in molecular media. Because of their unique resonance and geometry properties, M-E nonlinearities can occur in almost any dielectric material, and the strength of the interaction can approach that of all-electric interactions.

The goal of this thesis is to advance the understanding of interactions of the magnetic field of light with matter. To that end, an investigation of the M-E rectification nonlinearity in molecules using experimental and computational methods is presented. The first experimental observation of M-E rectification is reported. The theory of two enhancement mechanisms that account for relativistic effects at non-relativistic intensities will be discussed.

The organization of this thesis is as follows. Chapter 1 provides an overview of the history of research into the magnetic field of light. Although the optical magnetic field is much weaker than the optical electric field, there are scenarios in which the effect of the magnetic field can be enhanced. For high optical intensities that can accelerate electrons to relativistic velocities, the effect of the optical magnetic field is comparable with that of the optical electric field. Enhancement of magnetic field interactions can occur at lower intensities if the interaction medium has a magnetic resonance near the frequency of light. Some unique materials do have magnetic dipole transitions in the optical frequency range, although for most materials magnetic resonances are strong only at microwave frequencies. Strong magnetic effects can also be obtained in materials where the electric field can directly drive material magnetization without the involvement of an optical magnetic field, though this too is mostly limited to microwave frequencies. Artificial materials can also be fabricated to have unique optical properties including magnetic enhancement at optical frequencies. Magnetic effects can also be caused by ultrafast transfer of angular momentum even if the optical magnetic field is not involved. Previous work on the family of M-E nonlinearities to which the M-E rectification nonlinearity belongs is reviewed.

Two theoretical models of M-E nonlinearities are presented in Chapter 2, with an emphasis on M-E rectification. The first model is a classical model based on a pair of coupled oscillators. One oscillator models the response of a bound electron to an electromagnetic field, while the second models the rotational dynamics of a diatomic molecule. The two models are coupled to allow the electromagnetic field to drive molecular rotations. Two enhancement mechanisms are identified - a parametric resonance that seeds the M-E nonlinearities, and molecular torque which further enhances the magnitude of the M-E polarization and magnetization moments. The second theoretical model is derived from quantum mechanical density matrix theory applied to a three level system in which rotational states are mixed with electronic states. The mixing of states allows a magnetic dipole transition to take place at nearly the same frequency as an electric dipole transition through a magnetic-field mediated exchange of orbital angular momentum for rotational angular momentum. The implications of these theoretical models for the rectification moment is discussed.

The experimental and computational methods used in this thesis are presented in Chapter 3. An experimental setup to detect M-E rectification through induced second harmonic generation was developed. This setup was based on a crossed-beam pump-probe geometry in which the pump and probe beams were oriented at right angles. This unique geometry was necessary due to the longitudinal orientation of the M-E rectification field. This crossed-beam geometry necessitated the use of tilted pulse fronts to maintain an ultrafast temporal resolution. The design of a second experimental setup to detect M-E rectification by measuring induced birefringence is also presented. This second experiment could be calibrated using waveplates to directly measure the magnitude of

the induced rectification moment. Details of the computational implementations of the theoretical models of Chapter 2 are discussed as well.

Chapter 4 covers the experimental and computational results of this thesis. Data from the induced second harmonic generation experiment is presented. A clear pump-induced second harmonic signal is observed. The second harmonic radiation signal dependence on the power and polarization of both the pump and probe beams is analyzed to show that the experimental results are consistent with the theory of M-E rectification. Other possible sources of second harmonic generation are discussed and ruled out. Computational results from both the classical and density matrix models are shown and analyzed. The similarities and differences of the two models are explained. Chapter 5 summarizes the results and presents the main conclusion of this thesis. The ultrafast signal measured in the second harmonic generation experiment is found to be uniquely consistent with M-E induced second harmonic generation, and as such represents the first experimental observation of the M-E rectification moment. Results from the two computational models showed the role of the electronic and molecular properties of the interaction medium on the timescale and magnitude of the generated rectification moment. The computational results were consistent with the experimentally measured results. Future avenues of work are discussed, along with potential applications of the M-E rectification nonlinearity.

1.1 Background

This section covers related work on the interaction between the optical magnetic field and matter. Areas of research in which material magnetization is affected by the optical electric field are also included.

1.1.1 Relativistic Magnetic Effects

Despite the inherent weakness of the optical magnetic field, magnetic effects become significant at high optical intensities due to relativistic electron motion. For intensities above $I \approx 10^{12}$ W/cm², matter is ionized to form a plasma. Plasma electrons subject to these high-intensity beams can be accelerated to energies of 1 GeV and higher corresponding to a Lorentz factor $\gamma > 2000$ [9; 10]. At these energies, the contribution of the optical magnetic field to particle motion through the Lorentz force becomes comparable to that of the optical electric field. Under these conditions a quasi-static longitudinal electric field forms in the wake of the high intensity pulse as electrons are ejected from the beam, leaving behind only the positively charged ions [11]. The field strength of this longitudinal polarization is on the same order as the electric field from the laser. There is also direct laser acceleration of electrons along the direction of beam propagation caused by the

$\vec{v} \times \vec{B}$ component of the Lorentz force [12; 13]. The path followed by these accelerated electrons is shown in Fig. 1.1.

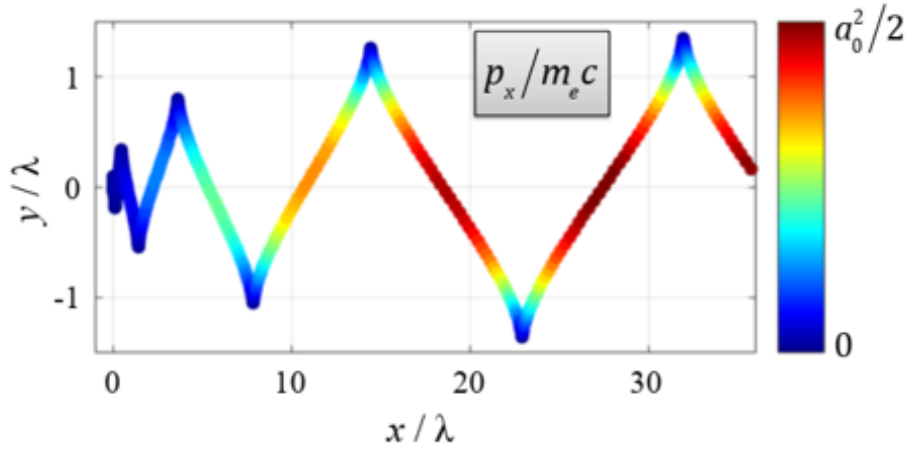


Figure 1.1: Plot of simulated electron position in y vs x as it is accelerated by an intense laser source. The color axis shows electron energy. Reprinted from Ref. [12].

While these high energy effects show the power of the optical magnetic field, these effects are only relevant for free electrons and are not directly applicable to work at intensities below the ionization threshold. Researchers looking to take advantage of the optical magnetic field in non-plasma matter must therefore find other enhancement mechanisms.

1.1.2 Magnetic Materials at Optical Frequencies

The most obvious way of enhancing the effect of the optical magnetic field is to use media that interact strongly with magnetic fields at the desired frequency. These materials are easily found when working at microwave frequencies, as the energy of microwave radiation is close to the energies of magnetic dipole transitions between magnetic sublevels of an electron orbital. However very few materials exhibit magnetic resonances at optical frequencies. Some rare earth ions exhibit optical frequency magnetic dipole transitions, such as the lanthanide series and in particular europium [14; 15; 16]. These optical frequency transitions occur because the intra-configurational transitions of the lanthanides often do not require a change in the radial quantum number. Hence transitions which only change the projection of the orbital angular momentum quantum number - magnetic dipole transitions - are sometimes allowed for linearly polarized light in these heavy elements. The first direct measurement of the strength of a magnetic dipole transition in europium ions was made in 2017 [17]. Measurements of the Rabi oscillation frequency were made by measuring the transmission of a probe beam through the sample and calculating the period between

adjacent peaks in the probe transmission as shown in Fig. 1.2. The magnetic dipole transition matrix element μ was calculated using the equation

$$\Omega = \frac{B\mu}{\hbar} \quad (1.2)$$

where Ω is the measured Rabi frequency and B is the magnitude of the optical magnetic field.

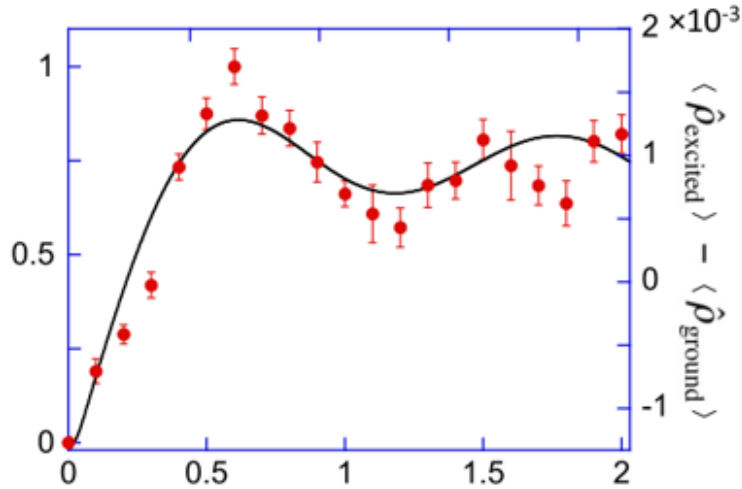


Figure 1.2: Measured transmission of a probe beam through a sample versus the time duration of a driving pulse. The black line was generated by a numerical simulation of the populations of ground and excited state. Reprinted from Ref. [17].

Rabi flopping can only occur if the incident field is strong enough to drive the transition at a rate faster than the rate of decay or dephasing of the system. Later work demonstrated spectral hole burning and electromagnetically induced transparency on the same magnetic dipole transition in europium, both of which require similarly strong interaction strengths [18]. The observation of these strong-field effects demonstrated that strong interactions between the optical magnetic field and matter are possible in materials which naturally possess magnetic dipole transitions at optical frequencies.

1.1.3 Linear M-E Interactions

Another way of obtaining strong magnetic effects is to bypass the magnetic field entirely and use the electric field of light to directly generate magnetic effects. Interactions in which the optical electric field induces magnetic effects (or vice versa) are called magneto-electric interactions [19]. By expanding the polarization and magnetization of a material in powers of the electric and mag-

netic field, the magneto-electric susceptibilities are found to be:

$$P_i(\vec{E}, \vec{H}) = P_i^S + \epsilon_0 \epsilon_{ij} E_j + \alpha_{ij} H_j + \frac{1}{2} \beta_{ijk} H_j H_k + \gamma_{ijk} H_j E_k + \dots \quad (1.3)$$

$$M_i(\vec{E}, \vec{H}) = M_i^S + \mu_0 \mu_{ij} H_j + \alpha_{ij} E_j + \beta_{ijk} E_j H_k + \frac{1}{2} \gamma_{ijk} E_j E_k + \dots \quad (1.4)$$

where P_i^S and M_i^S are the static polarization and magnetization moments respectively. Most research into these magneto-electric interactions is focused on the linear magneto-electric effect controlled by the α_{ij} tensor. An illustrative example of one such application of this effect is the development of magnetization in a material that is simultaneously piezoelectric and magnetostrictive [20]. If such a material is subjected to an electric field, the piezoelectric response will induce mechanical stress. This mechanical stress will then induce a magnetization through the magnetostrictive response, so the net effect is to induce a material magnetization through the application of an electric field. The linear magneto-electric response does exhibit enhancement when the frequency of the applied electric or magnetic field is tuned close to an existing magnetic resonance [21] or electromechanical resonance [22; 23; 24; 25]. In most cases, these resonances occur at microwave frequencies up to 9.3 GHz [22] although magneto-electric resonances in the THz frequency range have been reported [26].

1.1.4 Metamaterials

Magneto-electric coupling between an electric field and a magnetic response is also the approach used in metamaterials research. Metamaterials are fabricated materials in which the nanostructure of the material is carefully designed such that the optical electric field induces optical frequency magnetism in the material [27; 28]. These materials are an attempt to create a negative index material, predicted by V. Veselago to possess lossless refractive at negative angles relative to normal refraction [29]. Similar to the study of the linear magneto-electric effect, these materials offer an alternate approach to manipulating the magnetic permeability μ in a broad class of materials. The classic example of a metamaterial is a patterned series of circular nanoscale metal rings called split-ring resonators [28], shown in Fig. 1.3.

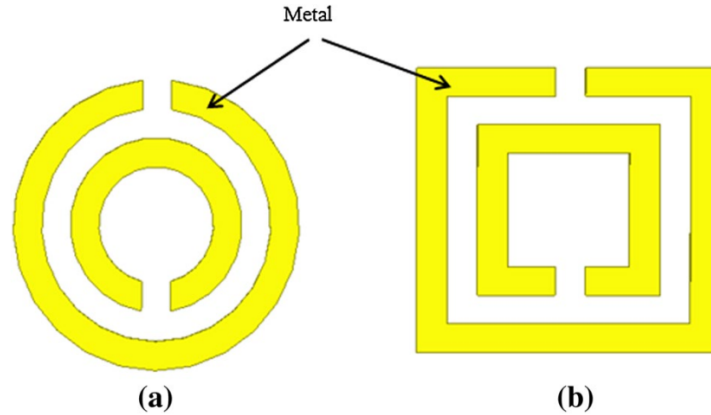


Figure 1.3: Diagram of (a) circular and (b) rectangular split ring resonators. Reprinted from Ref. [30].

When illuminated, conduction electrons in the metal respond quickly to the optical electric field, and the circular structure forces current to flow around the ring. Because of the small scale of the ring with respect to the incident wavelength, the circular current flow can be treated as a material magnetization. Similar enhancement can be found in small dielectric spheres, where enhanced magnetization occurs at specific frequencies that are functions of particle size and shape due to Mie scattering [31]. Because these materials are fabricated, the precise dimensions and properties of the material can be chosen to obtain a desired operation frequency. Inhomogeneous metamaterials, where the type of nanostructure varies within the material itself, can also be designed [32; 33]. These structures offer unprecedented control over the manipulation of light and designs can even be programmatically generated to perform dedicated applications [34; 35].

1.1.5 Ultrafast Demagnetization

While not strictly involving the optical magnetic field, light can induce magnetization changes in magnetized materials on ultrafast timescales through the transfer of angular momentum. Ultrafast magnetization dynamics have been shown to take place in magnetized ferromagnetic nickel film illuminated by intense ultrafast pulses [36]. After illumination, the net material magnetization as measured by the magneto-optic Kerr effect decreases rapidly within 1 ps and gradually returns to its original value on a much longer timescale. Demagnetization has since been observed in a variety of metallic materials [37]. The dynamics of this interaction are well described by a phenomenological three temperature model that predicts the transfer of energy from hot electrons excited by the optical field to the electron spins and the lattice. However while the three temperature model can accurately describe the transfer of energy between electrons, spins, and the lattice, it does not provide a mechanism for the transfer of angular momentum away from the spin system [38].

There are competing explanations of the dominant mechanism for angular momentum transfer including spin-flip scattering where angular momentum is transferred to a phonon during the spin-flip process [38], spin-orbit torque induced by spin-orbit coupling [39], and direct coherent light-spin interactions [40]. Regardless of the exact mechanism responsible for the transfer of angular momentum, it has been shown through X-ray diffraction experiments that the angular momentum from the spin system is ultimately transferred to the lattice through the generation of circularly polarized phonons at an ultrafast timescale [41; 42].

1.2 Previous Work on M-E Nonlinearities

Research into the family of M-E nonlinearities which includes M-E rectification first began in 2007 with experimental work performed by S. Oliveira [43]. Scattering experiments on molecular liquids found that strong magnetic dipole scattering could take place in isotropic liquids such as CCl_4 when illuminated by laser light at visible and near-IR wavelengths [43; 44]. The origin of the scattered light was determined by detecting the scattered light at exactly 90° from the incident laser pulse. At this angle, photons that were scattered by an electric dipole process were vertically polarized in the lab frame while photons scattered by a magnetic dipole process were horizontally polarized. A polarizer with a high extinction ratio was placed in front of the detector. By rotating the polarizer to pass only vertical (electric dipole) or horizontal (magnetic dipole) polarization, the type of scattered light that reached the detector could be isolated. The total intensity of both electric and magnetic dipole scattering was measured for all values of the incident polarization. The laser intensities used in these scattering experiments were around $I \approx 10^8 \text{ W/cm}^2$ to $I \approx 10^{10} \text{ W/cm}^2$ which were well below the relativistic limit. Despite using samples that were traditionally assumed to be non-magnetic due to compositions based on non-magnetic constituent atoms, significant amounts of magnetic dipole scattering were detected. The intensity of this magnetic scattering was found to have a quadratic dependence on the input intensity as seen in Fig. 1.4, and the ratio of the intensities of magnetically scattered light to electric dipole scattered light was determined to be as high as $\frac{1}{4}$. This experiment provided the first evidence of nonlinear magnetic dynamics that could take place at optical frequencies.

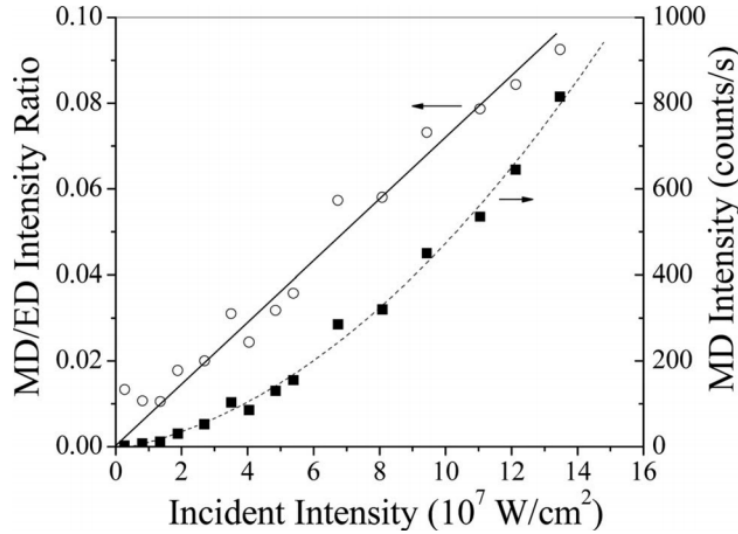


Figure 1.4: Intensity of magnetic dipole scattered light plotted vs input intensity. The black data points show the magnitude of the magnetic dipole scattered light, while white data points show the ratio in intensity between magnetic scattered light and electric scattered light. Reprinted from Ref. [43].

A quantum theory of these M-E interactions based on density matrix theory for specialized rare earth transitions with no change of principal quantum number was introduced in 2009 by S.C. Rand [45], and a classical theory developed by W. Fisher followed soon after in 2011 [46]. These theories both described atomic M-E dynamics in which nonlinearities could be jointly driven by the optical electric and magnetic field. The density matrix analysis predicted three distinct M-E nonlinearities. The first, enhanced optical frequency magnetism, was the cause of the strong magnetic dipole scattering observed in Refs. [43; 44]. The second and third nonlinearities induced the development of quasi-static and frequency doubled longitudinal polarization moments parallel to the direction of laser propagation. These nonlinear effects are similar to those observed in free electrons driven at relativistic intensities, but occur instead at non-relativistic intensities in solid and liquid media with bound electrons. Quantum theory of M-E interactions was later refined as will be shown below. A time-dependent density matrix theory of M-E nonlinearities is described further in Chapter 2. The classical theory from Ref. [46] simulated the motion of a bound electron in response to both the electric and magnetic fields of an incident optical field. The action of the optical magnetic field perturbs the motion of bound electrons causing enhanced magnetization. The perturbed electron path also induces a pair of polarization moments parallel to the optical wavevector; one frequency doubled moment and one quasi-static rectification moment. Thus the classical theory also predicted the existence of the same three distinct magneto-electric polarization and magnetization moments as the density matrix theory. The dynamics thought to be responsible

for the large magneto-electric nonlinearities were revealed to be a parametric resonance that coupled energy from electron motion parallel to the electric field to longitudinal electron motion [47]. However, while these theories did qualitatively explain enhanced magnetism at the optical driving frequency, they could not completely account for the large magnitude of experimentally measured magnetic dipole scattering in molecular liquids or the time dependence of these phenomena.

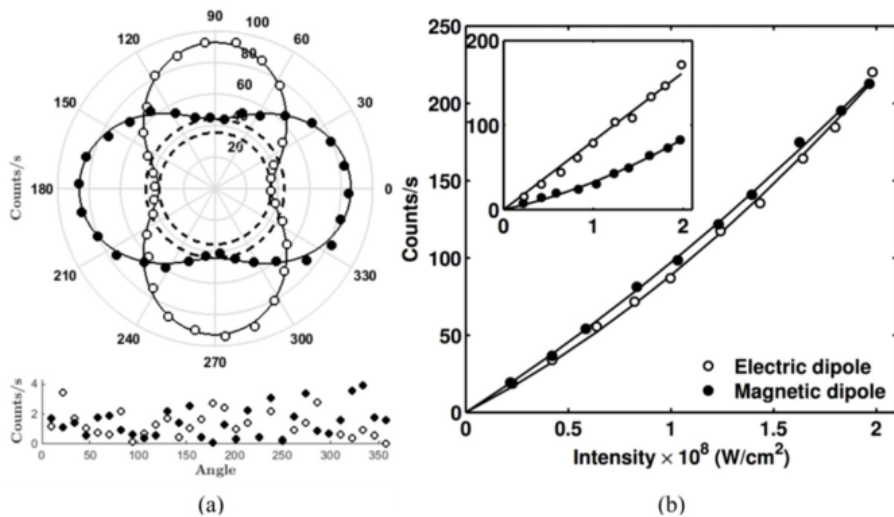


Figure 1.5: Scattering data for gadolinium gallium garnet. (a) Intensity of magnetic dipole scattered light plotted vs incident polarization. The black data points show the magnitude of the magnetic dipole scattered light, while white data points show the magnitude of the electric dipole scattered light. Dashed circles show fits to the unpolarized contribution to the scattering intensity while solid lines show $\sin^2(\theta)$ fits to the polarized contribution. The residuals show that this combination of unpolarized scattering and dipole scattering is an excellent fit to the data. (b) Intensity of the unpolarized electric dipole (white) and magnetic dipole (black) scattered light versus incident optical intensity. Inset: plot of polarized electric dipole and magnetic dipole scattering versus incident intensity. Reprinted from Ref. [48].

A breakthrough in the understanding of M-E nonlinearities was achieved when it was realized that there was an additional enhancement mechanism that relied on a magnetic field mediated exchange of orbital angular momentum for molecular angular momentum [49; 50; 1]. This transfer of angular momentum from the electron to the molecular is similar to the Einstein de Haas effect which found that electron spin could be converted into macroscopic rotational angular momentum, but in this case the transfer of angular momentum is ultrafast [51]. This second enhancement mechanism was capable of explaining the large relative intensity of magnetic dipole scattering compared to electric dipole scattering that had been experimentally observed in liquids and, for the first time, in solids by A. Fisher [48]. The experimentally measured magnetic dipole scattering and electric dipole scattering in one such solid, gadolinium gallium garnet, is shown in Fig. 1.5. The ratio of the electric and magnetic dipole scattered light is close to unity despite the fact that

the gadolinium gallium garnet sample was unmagnetized. Similar results were obtained in other strictly non-magnetic solids. This experimental result was accompanied by additional theoretical work that sought to develop a molecular theory of M-E nonlinearities. A dressed state quantum theory was developed that provided a full description of molecular M-E nonlinearities [49]. In this updated quantum theory, the role of the magnetic interaction was to convert the motion initiated by the electric field into molecular motion. This mechanism can occur in any dielectric molecule.

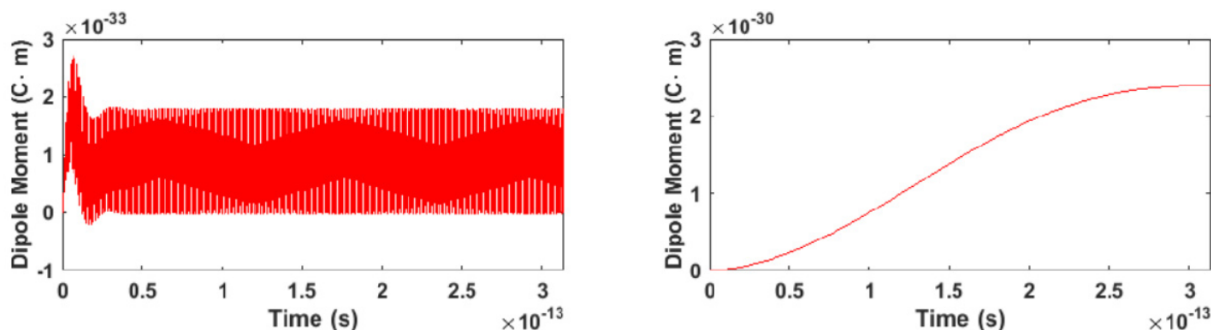


Figure 1.6: Longitudinal polarization moment versus time generated by a classical model of M-E nonlinearities. (a) Output when $\frac{I_{\perp}}{I_{\parallel}} = 1$. (b) Output when $\frac{I_{\perp}}{I_{\parallel}} = 1000$. Reprinted from Ref. [1].

A classical model of molecular magneto-electric effects was also developed [1]. The model of an electron oscillator in a magnetic field from Ref. [46] was modified by allowing electron motion to drive diatomic molecular motion. The intensity of the M-E polarization and magnetization moments was found to depend strongly on the molecular properties of the system under investigation. The molecular torque enhancement factor was found to be proportional to the ratio of moments of inertia $\frac{I_{\perp}}{I_{\parallel}}$ for rotational motion perpendicular and parallel to the internuclear axis, respectively. This ratio represents the efficiency of converting electron motion to molecular torque. The effect of molecular torque is shown in Fig. 1.6. For low values of $\frac{I_{\perp}}{I_{\parallel}}$ such as those used in generating the results shown in Fig. 1.6(a), the overall magnitude of M-E polarization was low. The polarization nonlinearity was dominated by motion at the second harmonic frequency while the magnitude of the quasi-static rectification was low. The M-E polarization generated when $\frac{I_{\perp}}{I_{\parallel}}$ is increased is shown in Fig. 1.6(b). The overall magnitude of the polarization is increased due to the additional efficiency of the torque exchange mechanism, and the quasi-static M-E rectification field forms the bulk of the response. This classical model is further described in Chapter 2. The discovery of torque enhancement meant that both the classical and quantum theory could accurately predict the intensity of the magnetic dipole scattering observed in Refs. [43; 44; 48].

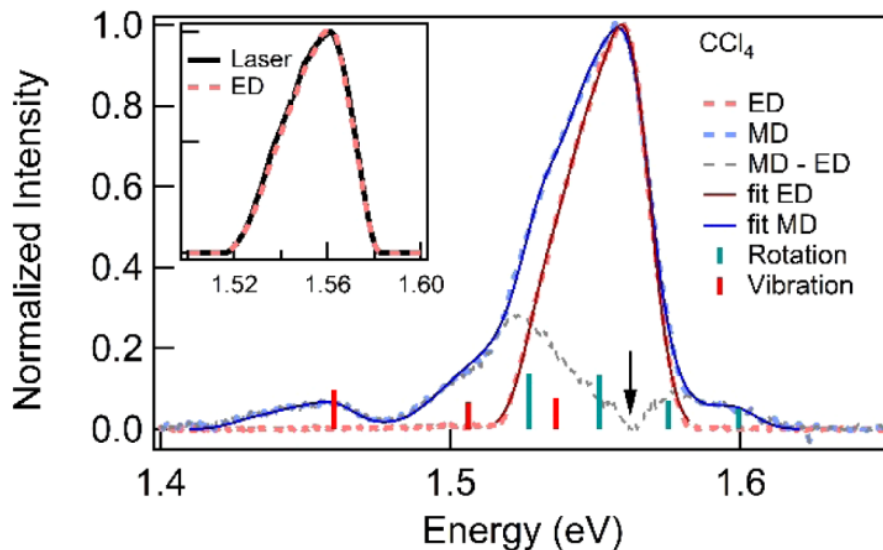


Figure 1.7: Normalized spectra of scattered light arise from electric dipole (red) and magnetic dipole (blue) scattering. The differences between the electric dipole and magnetic dipole spectra are shown in the black curve. Transition frequencies of rotational and vibrational features are shown by the green and red bars respectively. Inset: the electric dipole spectrum overlaid with the laser spectrum. Reprinted from Ref. [52].

Further experimental evidence for the role of molecular dynamics in M-E interactions was obtained in 2019 by T. Trinh [52]. In this work, scattering experiments were performed on CCl_4 similar to those detailed in Refs. [43; 44; 48]. The scattered light was analyzed with a spectrometer, and the spectra of the electric dipole scattered light and magnetic dipole scattered light are shown in Fig. 1.7. The spectrum of the electric dipole scattered light was indistinguishable from that of the laser, as expected for Rayleigh scattering. However the spectrum of magnetic dipole scattered light deviated significantly from the the laser spectrum, as several additional spectral features were observed. The difference of the normalized spectra showed that the placements of these spectral features were in excellent agreement with the frequency of Raman shifts due to rotational and vibrational excitations. The scattered light was therefore evidence that the laser was inducing molecular rotational motion in the liquid sample. Because these features only appeared in the magnetic dipole spectrum, the induced molecular motion could only be caused through interaction with the optical magnetic field. The observation of magnetic field induced molecular rotations thus confirmed the previous theoretical predictions of molecular M-E nonlinearities.

While significant work has been done in the field of nonlinear M-E scattering, work to date on the M-E rectification moment has consisted of theoretical predictions with both classical and quantum models as well as computational simulations based on the classical model. In all of these cases, the driving field was assumed to be a steady state field so no study of the temporal

characteristics of M-E rectification has been performed. To date, there has been no experimental work performed to observe the M-E rectification moment. The work in this thesis aims to address these limitations by providing the first experimental measurement of the M-E rectification field. This experimental work has been published in Ref. [2]. In addition, two computational models of M-E rectification are presented that can simulate the time-dependent M-E response of a material to pulsed illumination. This includes an extension of the classical model presented in Ref. [1] as well as for the first time a time-dependent quantum model of M-E rectification based on density matrix theory. The classical and quantum theories are outlined in Chapter 2. A description of the experimental and computational methods used in this thesis can be found in Chapter 3. An experimental setup was designed to detect the M-E rectification moment through induced second harmonic generation in a sample with inversion symmetry. Because even a small rectification field would break inversion symmetry and allow second harmonic generation, this setup provided a highly sensitive method of detecting the presence of the M-E rectification field. Additionally, a second experiment was designed to detect M-E induced birefringence that could directly measure the magnitude of the M-E rectification field. Details of the computational models are presented, including a discussion of modifications made to the theory from Chapter 2 to allow for efficient simulation. The results of the experimental and computational work are presented in Chapter 4, as too is a discussion of the results. Finally, a summary of the results of the work in this thesis along with a discussion of potential future avenues of research can be found in Chapter 5.

CHAPTER 2

Theory

This chapter discusses the theory of M-E optical nonlinearities in molecules. Two models of a molecular system are used. The first, described in Section 2.1, is a classical approach that models the system as a coupled pair of oscillators. One oscillator tracks the response of an electron to an applied optical field, while the other tracks molecular rotation. The two oscillators are coupled allowing electron motion to drive molecular motion. Two enhancement mechanisms are identified, parametric resonance and molecular torque, that allow the M-E response to exhibit relativistic characteristics at non-relativistic intensities. In the second method, the molecular system is modelled as a three-state quantum system. This approach is detailed in Section 2.2. The response of the quantum system to an optical field is calculated using the density matrix. A perturbative solution is found up to second order. Both the coupled oscillator and density matrix models exhibit M-E effects arising from the joint action of the optical electric and magnetic fields. The forms of the M-E nonlinearities predicted by the two models are broadly consistent with the previously obtained experimental evidence of M-E nonlinearities described in Chapter 1. A detailed discussion of M-E rectification is presented in Section 2.3. Each model has similar predictions for the dynamics of M-E rectification.

The theory presented in this chapter assumes the molecular system is driven by a plane wave and focuses on steady state behavior. This allows analytic results to be obtained and makes the underlying physics of M-E nonlinearities more clear. However, both the coupled oscillator and density matrix models can be analyzed numerically to reveal the transient response of the system to a laser pulse with fewer simplifying assumptions. The techniques used to produce these numerical solutions are presented in Chapter 3, and the simulation results can be found in Chapter 4.

2.1 Classical Coupled Oscillator Model of M-E Interactions

The classical model describes a molecular system illuminated by light as a pair of coupled oscillators, the first of which models the linear motion of an electron driven by an electromagnetic

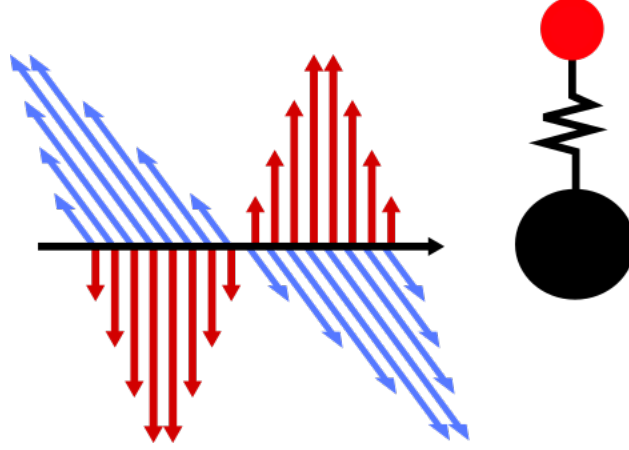


Figure 2.1: Classical electron oscillator. The electron, in red, is attached to a static restoring point by a spring-like force and excited by an electromagnetic field.

field while the second models the rotational motion of the molecule. The electron model is based on the classical Lorentz electron oscillator model where the effect of the optical magnetic field is included. The inclusion of magnetic effects makes the electron motion three dimensional and generates the M-E nonlinearities. The electron model is then coupled to a rigid rotor model of a molecule. The coupling is accomplished by letting the restoring point of the electron model rotate around the center of mass of the molecule. This coupling allows the electron motion to drive molecular rotations. The computational model of the coupled oscillator system is described in Section 3.3.1, and the simulation results can be found in Chapter 4.

2.1.1 Electron Oscillator in a Magnetic Field

The first component of the coupled oscillator model is the electron oscillator model. This model describes the response of an electron to an applied optical field. The electron is modelled as a point charge attached to a restoring point by a spring-like force, as shown in Fig. 2.1. The interaction between a plane wave and the electron is considered by letting the electric and magnetic fields of the plane wave drive electron motion through the Lorentz force $\vec{F} = q\vec{E} + q(\vec{v} \times \vec{B})$. This gives a set of equations of motion for the electron in Cartesian coordinates.

$$\ddot{x} + \gamma\dot{x} + \omega_0^2x = \frac{q}{m}E_x + \frac{q}{m}\dot{y}B_z - \frac{q}{m}\dot{z}B_y \quad (2.1)$$

$$\ddot{y} + \gamma\dot{y} + \omega_0^2y = \frac{q}{m}E_y + \frac{q}{m}\dot{z}B_x - \frac{q}{m}\dot{x}B_z \quad (2.2)$$

$$\ddot{z} + \gamma\dot{z} + \omega_0^2z = \frac{q}{m}E_z + \frac{q}{m}\dot{x}B_y - \frac{q}{m}\dot{y}B_x \quad (2.3)$$

Here γ is the damping rate of the electron motion, ω_0 is the resonant frequency of the electron

oscillator, and m is the electron mass. If the incident field is weak, the magnetic terms on the right hand sides of Eqns. 2.1 - 2.3 are assumed to be negligible and the electron motion in each direction can be calculated independently. However, for strong driving fields these magnetic field terms couple the equations of motion through a parametric resonance, so all three dimensions of electron motion must be considered simultaneously[53]. While an analytic solution to the coupled equations of motion is generally impossible to obtain, applying a perturbative approach reveals the characteristics of the M-E nonlinearities driven by the magnetic terms. If the incident optical field is assumed to be a plane wave with $\vec{E} = E_0 \cos(\omega t) \hat{x}$, $\vec{B} = B_0 \cos(\omega t) \hat{y}$ with a wavevector $\vec{k} = k_0 \hat{z}$, the equations of motion simplify to

$$\ddot{x} + \gamma \dot{x} + \omega_0^2 x = \frac{q}{m} E_0 \cos(\omega t) - \frac{q}{m} \dot{z} B_0 \cos(\omega t) \quad (2.4)$$

$$\ddot{y} + \gamma \dot{y} + \omega_0^2 y = 0 \quad (2.5)$$

$$\ddot{z} + \gamma \dot{z} + \omega_0^2 z = \frac{q}{m} \dot{x} B_0 \cos(\omega t) \quad (2.6)$$

The electron is assumed to be initially at rest at the origin. Because there is no initial velocity, to first order the electron motion depends only on the electric field.

$$\ddot{x} + \gamma \dot{x} + \omega_0^2 x = \frac{q}{m} E_0 \cos(\omega t) \quad (2.7)$$

This has the well known solution

$$x = \frac{qE_0}{m} \frac{1}{\sqrt{(\omega_0^2 - \omega^2) + \gamma^2 \omega^2}} \cos(\omega t + \tan^{-1}(\frac{\gamma \omega}{\omega_0^2 - \omega^2})) \quad (2.8)$$

If the electron is driven on resonance so $\omega = \omega_0$, the solution simplifies further

$$x = \frac{qE_0}{m\gamma\omega} \sin(\omega t) \quad (2.9)$$

$$\dot{x} = \frac{qE_0}{m\gamma} \cos(\omega t) \quad (2.10)$$

Returning to Eqn. 2.6, this first order solution for the electron position and velocity drives a magnetic contribution to the \hat{z} equation of motion in second order.

$$\begin{aligned} \ddot{z} + \gamma \dot{z} + \omega_0^2 z &= \frac{qE_0}{m\gamma} \cos(\omega t) \frac{qB_0}{m} \cos(\omega t) \\ &= \frac{1}{2} \frac{q^2 E_0 B_0}{m^2 \gamma} (1 + \cos(2\omega t)) \end{aligned} \quad (2.11)$$

The driving force for the \hat{z} equation of motion thus has two terms with different time dependencies

which can be treated separately. The $\cos(2\omega t)$ term results in a contribution to the electron motion that looks similar to Eqn. 2.8.

$$z_{2\omega} = \frac{1}{2} \frac{q^2 E_0 B_0}{m^2 \gamma} \frac{1}{\sqrt{9\omega^4 + 4\gamma^2 \omega^2}} \cos(2\omega t + \tan^{-1}(\frac{2\gamma}{3\omega})) \quad (2.12)$$

For the static term, it is sufficient to look only at the steady state dynamics of the electron motion. The steady state static contribution is thus simply

$$z_0 = \frac{1}{2} \frac{q^2 E_0 B_0}{m^2 \gamma \omega_0^2} \quad (2.13)$$

The combined second order solution valid under steady state conditions is

$$\begin{aligned} z &= z_0 + z_{2\omega} \\ &= \frac{1}{2} \frac{q^2 E_0 B_0}{m^2 \gamma \omega_0^2} + \frac{1}{2} \frac{q^2 E_0 B_0}{m^2 \gamma} \frac{1}{\sqrt{9\omega^4 + 4\gamma^2 \omega^2}} \cos(2\omega t + \tan^{-1}(\frac{2\gamma}{3\omega})) \end{aligned} \quad (2.14)$$

The position and linear momentum of the electron can be directly calculated in the form shown in Eqns. 2.8 and 2.14. However, the three dimensional nature of the electron motion means that it is possible for the electron to have angular momentum as well as linear momentum. The angular momentum is defined relative to the electron rest position as

$$\vec{L} = \vec{x} \times m\vec{v} = m(z\dot{x} - x\dot{z})\hat{y} \quad (2.15)$$

Using Eqns. 2.8 and 2.14, this becomes

$$L_y = \frac{1}{2} \frac{q^3 E_0^2 B_0}{m^2 \gamma^2} \left(\frac{\cos(\omega t)}{\omega^2} + \frac{-\cos(\omega t + \tan^{-1}(\frac{2\gamma}{3\omega})) + 3\cos(-3\omega t + \tan^{-1}(\frac{2\gamma}{3\omega}))}{2\sqrt{9\omega^4 + 4\gamma^2 \omega^2}} \right) \quad (2.16)$$

The position and momentum of the electron correspond to the polarization and magnetization moments induced by the optical field. The electric dipole moment of the electron \vec{p} is proportional to its displacement from its restoring point, while the magnetic dipole moment $\vec{\mu}$ is proportional to the electron angular momentum L .

$$\vec{p} = -e\vec{x} \quad (2.17)$$

$$\vec{\mu} = \frac{-e}{2m} \vec{L} \quad (2.18)$$

Here e is the charge of the electron and m is the electron mass. Three distinct polarization and mag-

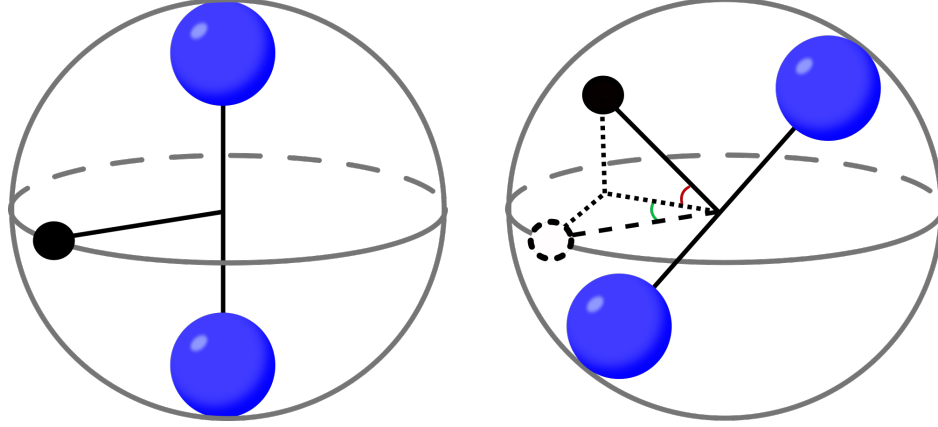


Figure 2.2: Rigid rotor model of a diatomic molecule. The time evolution of angles θ_{\perp} and θ_{\parallel} describe the rotational motion of the molecule.

netization moments arise from the parametric resonance created by the addition of the magnetic contribution to the Lorentz force. Two M-E polarization moments develop due to the longitudinal electron motion caused by the coupling of linear motion in the \hat{x} and \hat{z} directions. The first is the time-dependent term from Eqn. 2.12 which oscillates at twice the optical driving frequency. This represents M-E second harmonic generation. The second is a quasi-static rectification term from Eqn. 2.13 that does not oscillate. Both of these polarization moments are proportional to the product of E_0 and B_0 and so are quadratic nonlinearities. The third effect is the magnetization caused by the angular momentum seen in Eqn. 2.16. In this classical analysis, the magnetization has a cubic dependence on the driving field and is proportional to $E_0^2 B_0$. As shown later on in Section 2.2, this dependence is augmented by a quadratic dependence when formulated quantum mechanically. These M-E nonlinearities are directly seen when the optical magnetic field is included in calculations of the electron response to a driving field.

2.1.2 Coupling to a Rigid Rotor Model of a Molecule

The second component of the complete molecular model of M-E rectification is a rigid rotor model of a molecule. The rigid rotor model tracks the angular displacement of a torsional oscillator while assuming that the moment of inertia of the rotational motion is constant. The equations of motion for a torsional oscillator have a similar form to the linear oscillator but with the angular position and its time derivatives replacing the linear position.

$$\ddot{\theta} + \gamma_m \dot{\theta} + \omega_m^2 \theta = \frac{T}{I} \quad (2.19)$$

Here T is the driving torque and I is the moment of inertia of the molecule. The simplest possible system is a homonuclear diatomic molecular, which has two distinct moments of inertia for rotation parallel and perpendicular to the intermolecular axis. Thus two copies of Eqn. 2.19 are needed to track rotational motion for each rotational mode.

$$\ddot{\theta}_{\parallel} + \gamma_m \dot{\theta}_{\parallel} + \omega_m^2 \theta_{\parallel} = \frac{T_{\parallel}}{I_{\parallel}} \quad (2.20)$$

$$\ddot{\theta}_{\perp} + \gamma_m \dot{\theta}_{\perp} + \omega_m^2 \theta_{\perp} = \frac{T_{\perp}}{I_{\perp}} \quad (2.21)$$

The electron oscillator is coupled to the torsional oscillator by placing the restoring point of the electron model on the surface of the rigid rotor model, as diagrammed in Fig. 2.3. The initial position of the restoring point relative to the center of mass of the molecule is defined as \vec{r}_0 and the instantaneous position is \vec{r} . Because the position of the restoring point is no longer fixed to a specific position, the force that the electron exerts on the restoring point by Newton's Third Law can no longer be neglected. This force exerts torque on the molecular system which drives angular motion as described by Eqns. 2.20 and 2.21.

$$\vec{T} = m\omega_0^2(\vec{x} \times \vec{r}) \quad (2.22)$$

The equations of motion of the combined system include the two torsional oscillator equations of motion from Eqns. 2.20 and 2.21 in addition to the electron oscillator equations of motion from Eqns. 2.1 - 2.3.

$$\ddot{x} + \gamma\dot{x} + \omega_0^2 x = \frac{q}{m} E_x + \frac{q}{m} \dot{y} B_z - \frac{q}{m} \dot{z} B_y \quad (2.23)$$

$$\ddot{y} + \gamma\dot{y} + \omega_0^2 y = \frac{q}{m} E_y + \frac{q}{m} \dot{z} B_x - \frac{q}{m} \dot{x} B_z \quad (2.24)$$

$$\ddot{z} + \gamma\dot{z} + \omega_0^2 z = \frac{q}{m} E_z + \frac{q}{m} \dot{x} B_y - \frac{q}{m} \dot{y} B_x \quad (2.25)$$

$$\ddot{\theta}_{\parallel} + \gamma_m \dot{\theta}_{\parallel} + \omega_m^2 \theta_{\parallel} = \frac{(m\omega_0^2(\vec{x} \times \vec{r}))_{\parallel}}{I_{\parallel}} \quad (2.26)$$

$$\ddot{\theta}_{\perp} + \gamma_m \dot{\theta}_{\perp} + \omega_m^2 \theta_{\perp} = \frac{(m\omega_0^2(\vec{x} \times \vec{r}))_{\perp}}{I_{\perp}} \quad (2.27)$$

Together, these equations constitute a full description of the molecular dynamics involved in M-E nonlinearities. The addition of magnetic-field induced torque exchange to the electron oscillator enhances the magnitude of the rectification motion as will be shown in Section 2.3.

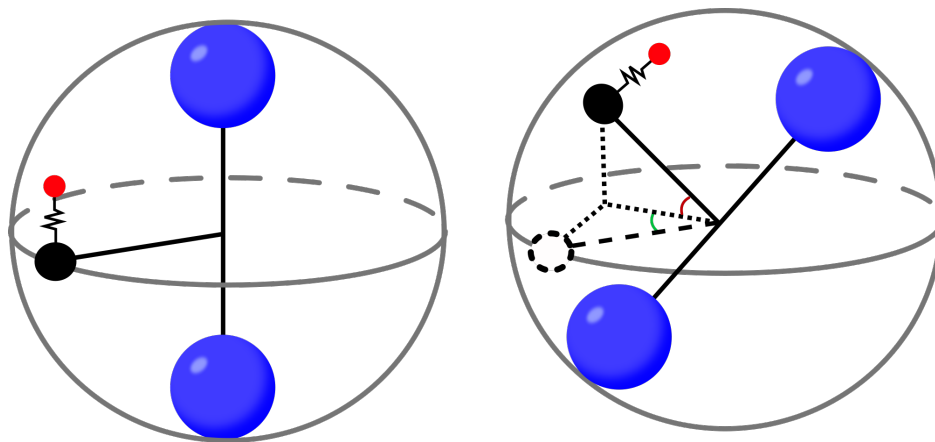


Figure 2.3: Coupled oscillator model of M-E nonlinearities. The restoring point of the electron oscillator is attached to the rigid rotor model. The electron motion induced by the incident field drives molecular rotations.

2.2 Density Matrix Model of M-E Interactions

An alternative, quantum mechanical formulation of M-E dynamics treats the molecule as a three level quantum system and uses the density matrix to calculate the interaction between an optical field and the molecule. The three level system described in Section 2.2.1 is the simplest quantum system that can exhibit M-E effects. Coupling between molecular rotations and the electronic states allows magnetic dipole transitions to take place at optical frequencies. The populations of the states and the coherences that develop between the states are calculated using the density matrix. Much like the coupled oscillator model, exact analytic solutions are difficult or impossible to obtain, so a perturbative approach is used. By iteratively calculating successive orders of perturbation up to second order, the nonlinear polarization and magnetization moments of the system can be found. While there are higher order corrections, calculating up to second order is sufficient to observe M-E rectification and magnetization. A computational model of the density matrix equations of motion is described in Section 3.3.2, and the simulation results can be found in Chapter 4.

2.2.1 Three Level Model of M-E Interactions

The density matrix model treats the molecule as a three level system, the details of which are described here. A diagram of this system is shown in Fig. 2.4. Two sets of basis states were used. The first set of basis states described the electronic structure $|nlm\rangle$ of the state in terms of the principal quantum number n , the orbital angular momentum quantum number l , and the magnetic quantum number m . The electronic ground state $|100\rangle$ and all magnetic sublevels of the first excited state $|210\rangle$, $|211\rangle$, and $|21-1\rangle$ were included. Because the system under investigation

is a molecule, the rotational states of the molecule were also included. The rotational basis states were $|00\rangle$, $|10\rangle$, $|11\rangle$, and $|1-1\rangle$. The three levels of the system shown in Fig. 2.4 were assigned combinations of these basis states depending on the electronic and rotational character of the state.

$$|1\rangle = |100\rangle|00\rangle \quad (2.28)$$

$$|2\rangle = |210\rangle|10\rangle \quad (2.29)$$

$$|3\rangle = |21-1\rangle|11\rangle \quad (2.30)$$

Given the electronic structure of the states, the allowed single-photon transitions between the states can be determined from the selection rules. There are two possible transitions that can occur. An electric dipole transition is permitted between two states if the change in the orbital angular momentum quantum number is $\Delta l = \pm 1$. Because the transitions between states $|1\rangle$ and $|2\rangle$ and $|1\rangle$ and $|3\rangle$ require a change in the orbital angular momentum, electric dipole transitions are allowed on those transitions. A magnetic dipole transition is allowed between states $|2\rangle$ and $|3\rangle$ because $\Delta l = 0$ and $\Delta m = \pm 1$. The energy levels of the three states are chosen such that the energy of state $|3\rangle$ falls between states $|1\rangle$ and $|2\rangle$ and states $|1\rangle$ and $|3\rangle$ are separated by the rotational energy of the molecule. This can occur in molecules due to orbital hybridization and coupling of electronic and rotational states in strong but not necessarily relativistic light fields. The electronic states therefore are not representative of the state energy, but rather the symmetry of the electron orbital. The energy of the electric dipole transition is equal to $\hbar\omega_{12}$, while the magnetic dipole transition energy is $\hbar\omega_{23}$ and the energy of molecular rotation is $\hbar\omega_{13}$. Due to the structure of the energy levels, the state energies are related by the equation $\hbar\omega_{12} = \hbar\omega_{23} + \hbar\omega_{13}$ as seen in Fig. 2.4. This relationship implies that the magnetic dipole transition is detuned from the electronic dipole transition by an energy $\hbar\omega_{13}$. However, at optical frequencies, the energy of molecular rotation is much lower than the energy of the electric dipole transition. Because $\hbar\omega_{12} \gg \hbar\omega_{13}$, it can be assumed that $\hbar\omega_{12} \approx \hbar\omega_{23}$.

2.2.2 Density Matrix Analysis

The populations and coherences of the three level system described above can be found explicitly using semi-classical density matrix theory. The three level system is driven by a classical optical field at a frequency ω . The optical field drives the electric dipole (ED) transition between $|1\rangle$ and $|2\rangle$ and the magnetic dipole (MD) transition between $|2\rangle$ and $|3\rangle$. The detuning on the ED transition is expressed as Δ_{12} and the detuning on the MD transition is Δ_{23} . Because $\hbar\omega_{13} \ll \hbar\omega$, the field-induced coupling between these states $|1\rangle$ and $|3\rangle$ is assumed to be negligible. The molecule is initially in the ground state. When the driving field is turned on, the only possible transition is the

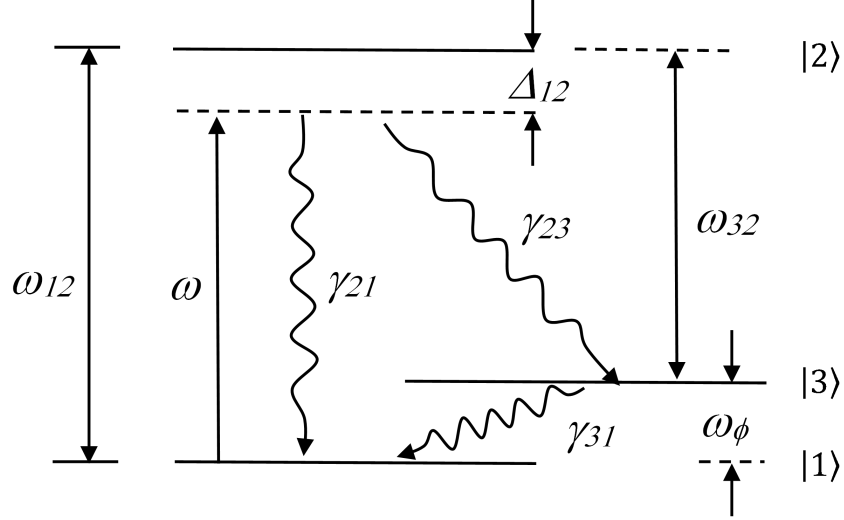


Figure 2.4: Diagram of the three-state quantum model of a molecular system. ω_ϕ is equal to the molecular rotational frequency ω_{13} .

ED transition that couples states $|1\rangle$ and $|2\rangle$ as there is no population or coherence in the system that can interact with the MD transition between states $|2\rangle$ and $|3\rangle$. During this transition the molecule absorbs a photon from the optical field. Because of the symmetry requirements of ED transitions, the excited state gains a quantum of angular momentum and thus has a total angular momentum of $L = 1$. Once the interaction is initiated by the electric field, the MD transition between states $|2\rangle$ and $|3\rangle$ can be driven by the optical magnetic field. During the downwards MD transition a photon is released from the system which conserves the system energy, and the orbital angular momentum is converted to rotational angular momentum which conserves the projection of angular momentum along the axis of quantization. The combination of these two interactions causes a coherence to form between states $|1\rangle$ and $|3\rangle$ from which the nonlinear M-E polarization and magnetization moments can be calculated.

The density matrix ρ takes the form of a 3×3 matrix with diagonal components. The value of the diagonal terms ρ_{ii} correspond to the probability that the system occupies state $|i\rangle$, and the off diagonal terms ρ_{ij} correspond to the coherence that forms between the states $|i\rangle$ and $|j\rangle$. The time evolution of the density matrix depends on the Hamiltonian of the system and the density matrix itself [45; 53].

$$i\hbar\dot{\rho} = [H, \rho] = H\rho - \rho H \quad (2.31)$$

The density matrix equation of motion can be solved analytically under certain simplifying assumptions. Perturbation theory allows each order of the solution to be solved iteratively, with the total solution to each density matrix element being the sum of all contributions. The perturbation

expansion of the density matrix is given by

$$\rho_{ij} = \rho_{ij}^{(0)} + \rho_{ij}^{(1)} + \rho_{ij}^{(2)} + \dots \quad (2.32)$$

Here, $\rho_{ij}^{(0)}$ is the initial value of the density matrix element ρ_{ij} , and $\rho_{ij}^{(n)}$ is the n th order correction term. Initially, the system starts in the ground state with no coherences.

$$\rho_{11}^{(0)} = 1 \quad (2.33)$$

$$\rho_{22}^{(0)} = \rho_{33}^{(0)} = \rho_{12}^{(0)} = \rho_{13}^{(0)} = \rho_{23}^{(0)} = 0 \quad (2.34)$$

The Hamiltonian H is written in the form $H = H_0 + V$ for simplicity. H_0 is the component of the Hamiltonian that has no dependence on the optical field, while the interaction Hamiltonian V is the component of the Hamiltonian that comes from the interaction between the system and the incident optical field. The optical field is assumed to be a plane wave at a frequency that can excite the $|1\rangle \leftrightarrow |2\rangle$ transition through a ED interaction and the $|3\rangle \leftrightarrow |2\rangle$ transition through an MD interaction. Because the $|1\rangle \leftrightarrow |3\rangle$ transition occurs at a much lower energy scale, it is assumed that the optical field cannot excite this transition. The interaction Hamiltonian for this field is

$$\begin{aligned} V &= V_{12}^{(1)}(e^{i\omega t} + e^{-i\omega t}) + V_{32}^{(1)}(e^{i\omega t} + e^{-i\omega t}) \\ &= -\frac{\hbar\Omega_{12}}{2}(e^{i\omega t} + e^{-i\omega t}) - \frac{\hbar\Omega_{32}}{2}(e^{i\omega t} + e^{-i\omega t}) \end{aligned} \quad (2.35)$$

The rotating wave approximation is valid because the detuning Δ_{12} of the $|1\rangle \leftrightarrow |2\rangle$ transition is assumed to be small. Thus the negative frequency terms can be neglected.

$$V = -\frac{\hbar\Omega_{12}}{2}e^{i\omega t} - \frac{\hbar\Omega_{32}}{2}e^{i\omega t} \quad (2.36)$$

The matrix elements then follow the equation of motion

$$i\hbar\dot{\rho} = [(H_0 + V), \rho] + i\hbar\frac{\partial\rho}{\partial t_{rel}} \quad (2.37)$$

The $\frac{\partial\rho}{\partial t_{rel}}$ term accounts for relaxation processes that are proportional only to the magnitude of the density matrix element and have no dependence on the Hamiltonian. The time evolution of each

term is then given by the following differential equations

$$i\hbar\dot{\rho}_{11} = (V_{12}\rho_{21} - \rho_{12}V_{21}) + i\hbar\gamma_{21}\rho_{22} + i\hbar\gamma_{31}\rho_{33} \quad (2.38)$$

$$i\hbar\dot{\rho}_{22} = -(V_{12}\rho_{21} - \rho_{12}V_{21}) - (V_{32}\rho_{23} - \rho_{32}V_{23}) - i\hbar\gamma_{21}\rho_{22} - i\hbar\gamma_{23}\rho_{22} \quad (2.39)$$

$$i\hbar\dot{\rho}_{33} = (V_{32}\rho_{23} - \rho_{32}V_{23}) + i\hbar\gamma_{23}\rho_{22} - i\hbar\gamma_{31}\rho_{33} \quad (2.40)$$

$$i\hbar\dot{\rho}_{12} = -\hbar\omega_{12}\rho_{12} + V_{12}(\rho_{22} - \rho_{11}) + (V_{13}\rho_{32} - \rho_{13}V_{32}) - i\hbar\Gamma_{21}\rho_{12} \quad (2.41)$$

$$i\hbar\dot{\rho}_{13} = -\hbar\omega_{13}\rho_{13} + (V_{12}\rho_{23} - \rho_{12}V_{23}) - i\hbar\Gamma_{31}\rho_{13} \quad (2.42)$$

$$i\hbar\dot{\rho}_{23} = \hbar\omega_{23}\rho_{23} + V_{23}(\rho_{33} - \rho_{22}) + (V_{21}\rho_{13} - \rho_{21}V_{13}) - i\hbar\Gamma_{23}\rho_{23} \quad (2.43)$$

Here γ_{ij} represents the population decay from state $|i\rangle \leftrightarrow |j\rangle$ while Γ_{ij} represents the decay of the coherence of the $|i\rangle \leftrightarrow |j\rangle$ transition. The remaining off diagonal matrix elements can be calculated by making use of the fact that $\rho_{ji} = \rho_{ij}^*$

$$\rho_{21} = \rho_{12}^* \quad (2.44)$$

$$\rho_{31} = \rho_{13}^* \quad (2.45)$$

$$\rho_{32} = \rho_{23}^* \quad (2.46)$$

2.2.2.1 First Order Terms

The first order corrections can be calculated by applying Eqns. 2.38 - 2.43 using the initial conditions and the form of the interaction Hamiltonian. Ignoring terms that are zero due to the initial conditions and rearranging to isolate the first order terms $\rho_{ij}^{(1)}$, the first order contributions are found using the following differential equations

$$\dot{\rho}_{11}^{(1)} = \gamma_{21}\rho_{22}^{(1)} + \gamma_{31}\rho_{33}^{(1)} \quad (2.47)$$

$$\dot{\rho}_{22}^{(1)} = -\gamma_{21}\rho_{22}^{(1)} - \gamma_{23}\rho_{22}^{(1)} \quad (2.48)$$

$$\dot{\rho}_{33}^{(1)} = \gamma_{23}\rho_{22}^{(1)} - \gamma_{31}\rho_{33}^{(1)} \quad (2.49)$$

$$\dot{\rho}_{12}^{(1)} = i\omega_{12}\rho_{12}^{(1)} - \frac{1}{i\hbar}V_{12}^{(1)}\rho_{11}^{(0)} - \Gamma_{21}\rho_{12}^{(1)} \quad (2.50)$$

$$\dot{\rho}_{13}^{(1)} = i\omega_{13}\rho_{13}^{(1)} - \Gamma_{31}\rho_{13}^{(1)} \quad (2.51)$$

$$\dot{\rho}_{23}^{(1)} = -i\omega_{23}\rho_{23}^{(1)} - \Gamma_{23}\rho_{23}^{(1)} \quad (2.52)$$

The first order corrections to the state populations are found by solving Eqns. 2.47 - 2.49. Under steady-state conditions, the solution to Eqn. 2.48 is

$$\rho_{22}^{(1)} = 0 \quad (2.53)$$

Using this result and applying the same logic to Eqns. 2.47 and 2.49, all first order corrections to the state populations are found to be zero.

$$\rho_{11}^{(1)} = \rho_{22}^{(1)} = \rho_{33}^{(1)} = 0 \quad (2.54)$$

In order to solve Eqns. 2.50, the coherence ρ_{12} is assumed to oscillate at the same frequency as the driving optical wave. The rotating wave approximation is valid on this transition, so only the positive $e^{i\omega t}$ term is included.

$$\rho_{12} = \tilde{\rho}_{12} e^{i\omega t} \quad (2.55)$$

where $\tilde{\rho}_{12}$ is a slowly-varying amplitude. On the timescale of the optical cycle, this amplitude is assumed to be constant so the time dependence in Eqn.2.55 is contained entirely in the $e^{i\omega t}$ term. Substituting Eqn.2.55 into Eqn.2.50 gives the first order solution for the slowly varying amplitude $\tilde{\rho}_{12}$

$$i\omega \tilde{\rho}_{12}^{(1)} e^{i\omega t} = i\omega_{12} \tilde{\rho}_{12}^{(1)} e^{i\omega t} - \frac{1}{i\hbar} V_{12}^{(1)} \rho_{11}^{(0)} - \Gamma_{21} \tilde{\rho}_{12}^{(1)} e^{i\omega t} \quad (2.56)$$

Because there are no driving terms in Eqns. 2.51 and 2.52, the solutions to those equations are taken to be $\rho_{13}^{(1)} = \rho_{23}^{(1)} = 0$. Substituting the expression for $V_{12}^{(1)}$ from Eqn. 2.36 into Eqn. 2.50 and simplifying gives the first order contribution to the ρ_{12} coherence.

$$\rho_{12}^{(1)} = \frac{1}{2} \frac{\Omega_{12}}{\Delta_{12} + i\Gamma_{12}} \rho_{11}^{(0)} e^{i\omega t} \quad (2.57)$$

where the detuning $\Delta_{12} = \omega_{12} - \omega$ is defined for simplicity. Thus to first order, the only effect of the optical field is to develop a coherence on the $|1\rangle \leftrightarrow |2\rangle$ electric dipole transition.

2.2.2.2 Second Order Terms

The first order terms derived above can be used in turn to derive the second order contributions to the solution for the density matrix elements. Returning to Eqns. 2.38 - 2.43 and keeping the terms that will add to the second order contribution, the following equations must be solved:

$$\dot{\rho}_{11}^{(2)} = \frac{1}{i\hbar}(V_{12}^{(1)}\rho_{21}^{(1)} - \rho_{12}^{(1)}V_{21}^{(1)}) + \gamma_{21}\rho_{22}^{(2)} + \gamma_{31}\rho_{33}^{(2)} \quad (2.58)$$

$$\dot{\rho}_{22}^{(2)} = -\frac{1}{i\hbar}(V_{12}^{(1)}\rho_{21}^{(1)} - \rho_{12}^{(2)}V_{21}^{(1)}) - \gamma_{21}\rho_{22}^{(2)} - \gamma_{23}\rho_{22}^{(2)} \quad (2.59)$$

$$\dot{\rho}_{33}^{(2)} = \gamma_{23}\rho_{22}^{(2)} - \gamma_{31}\rho_{33}^{(2)} \quad (2.60)$$

$$\dot{\rho}_{12}^{(2)} = i\omega_{12}\rho_{12}^{(2)} - \Gamma_{21}\rho_{12}^{(2)} \quad (2.61)$$

$$\dot{\rho}_{13}^{(2)} = i\omega_{13}\rho_{13}^{(2)} - \frac{1}{i\hbar}\rho_{12}^{(1)}V_{23}^{(1)} - \Gamma_{31}\rho_{13}^{(2)} \quad (2.62)$$

$$\dot{\rho}_{23}^{(2)} = -i\omega_{23}\rho_{23}^{(2)} - \Gamma_{23}\rho_{23}^{(2)} \quad (2.63)$$

Beginning with the second order contributions to the state populations, it is easiest to solve Eqn. 2.59 first as it is independent of the solutions of Eqns. 2.58 and 2.60. Under steady state conditions, the time derivative on the left half of Eqn. 2.59 goes to zero and the remaining terms can be rearranged to obtain:

$$\rho_{22}^{(2)} = \frac{-iV_{12}^{(1)}}{\hbar(\gamma_{21} + \gamma_{23})}(\rho_{21}^{(1)} - \rho_{12}^{(1)}) \quad (2.64)$$

Substituting the known forms of $V_{12}^{(1)}$ and $\rho_{12}^{(1)}$ and making use of Eqn. 2.44 gives

$$\rho_{22}^{(2)} = \frac{\Omega_{12}^2}{4(\gamma_{21} + \gamma_{23})} \frac{2\Gamma_{21}}{\Delta_{12}^2 + \Gamma_{21}^2} \quad (2.65)$$

Once the form for $\rho_{22}^{(2)}$ is found, Eqn. 2.60 can be solved to find

$$\rho_{33}^{(2)} = \frac{\gamma_{23}}{\gamma_{31}}\rho_{22}^{(2)} \quad (2.66)$$

The second order correction to ρ_{11} can be found by noting that the sum of all state populations should equal 1. Because the sum of the initial state populations is equal to one, the sum of all the corrections should equal zero. Using this result, $\rho_{11}^{(2)}$ can be written as

$$\rho_{11}^{(2)} = -\rho_{22}^{(2)} - \rho_{33}^{(2)} \quad (2.67)$$

For the coherences, it can be seen due to the lack of driving field terms that the solutions to Eqns. 2.61 and 2.63 will be zero. The process of solving Eqn. 2.62 is different than the procedure used to solve Eqn. 2.50. Here, the entire time dependence is contained in the $\rho_{12}^{(1)}V_{23}^{(1)}$ term. Using

the full expression for V_{23} from Eqn. 2.35, we find

$$\begin{aligned}\rho_{12}^{(1)} V_{23} &\propto e^{i\omega t} (e^{i\omega t} + e^{-i\omega t}) \\ \rho_{12}^{(1)} V_{23} &\propto (1 + e^{2i\omega t})\end{aligned}\quad (2.68)$$

Using Eqn. 2.68 and neglecting the terms that oscillate at 2ω , the only remaining terms are static and non-oscillatory. The time derivative on the right hand side of Eqn. 2.62 thus goes to zero.

$$0 = i\omega_{13}\rho_{13}^{(2)} - \frac{1}{i\hbar}\rho_{12}^{(1)}V_{23}^{(1)} - \Gamma_{31}\rho_{13}^{(2)}\quad (2.69)$$

Substituting the known forms of V_{23} and $\rho_{12}^{(1)}$, the solution to Eqn. 2.69 is

$$\rho_{13}^{(2)} = \frac{1}{4} \frac{\Omega_{12}\Omega_{32}^*}{(\Delta_{12} + i\Gamma_{12})(\omega_{13} + i\Gamma_{13})}\quad (2.70)$$

By inspection, Eqn. 2.70 can be modified to explicitly show its M-E characteristics.

$$\rho_{13}^{(2)} = \left(\frac{1}{2} \frac{\Omega_{12}e^{i\omega t}}{(\Delta_{12} + i\Gamma_{12})} \right) \left(\frac{1}{2} \frac{\Omega_{32}^*e^{-i\omega t}}{(\omega_{13} + i\Gamma_{13})} \right)\quad (2.71)$$

The left term in Eqn. 2.71 is equal to the coherence induced on the $|1\rangle \leftrightarrow |2\rangle$ transition and represent the electric contribution to the M-E interaction. The term on the right is the magnetic contribution as it arises from the Ω_{32}^* term that represents the optical magnetic field.

2.2.2.3 Calculating the M-E Polarization and Magnetization

The ρ_{13} term calculated above contributes to two M-E nonlinearities. The first is a quasi-static polarization moment orientated along the direction of propagation of the laser. This can be calculated by taking the trace of the density matrix and the electric dipole transition moment between states $|1\rangle$ and $|3\rangle$ and projecting the result along the x axis.

$$P_x^{(2)}(0) = \text{Tr}[\mu^{(e)}\rho] = \{(e\vec{r})_{13}\}_x \rho_{31} + \{(e\vec{r})_{31}\}_x \rho_{13}\quad (2.72)$$

It should be noted that because of the projection of the polarization moment is perpendicular to the \hat{z} and \hat{y} oscillations of the electric and magnetic field, it is non-oscillatory. Recalling the electronic states that make up states $|1\rangle$ and $|3\rangle$, the expectation value of the operator $e\vec{r}$ can be decomposed

$$e\langle 100|\vec{r}|211\rangle = e\langle 100|x|211\rangle\hat{x} + e\langle 100|y|211\rangle\hat{y}\quad (2.73)$$

Assuming a hydrogenic model so the electronic states have the same symmetry properties as the corresponding electronic states of hydrogen, the expectation value can be evaluated directly. This evaluation produces the following value

$$e\langle 100|\vec{r}|211\rangle = ea_0\frac{128}{243}(\hat{x} + i\hat{y}) = \mu_0^{(e)}\frac{\hat{x} + i\hat{y}}{\sqrt{2}} \quad (2.74)$$

The dipole moment $\mu_0^{(e)}$ in the density matrix model is assumed to be equal the transition moment between the s and p states of hydrogen. It shows up in the molecular three-level system because the electronic states are assumed to have the same symmetry properties as the corresponding hydrogen states. Taking the projection along x , the static polarization moment reduces to

$$P_x^{(2)}(0) = \frac{\mu_0^{(e)}}{\sqrt{2}}(\rho_{31} + \rho_{13}) \quad (2.75)$$

The magnetization can be found by taking the y projection of the trace of the density matrix and the M-E dipole moment. The y projection will only include the $e^{-i\omega t}$ oscillation of the optical magnetic field, so it too will oscillate at ω .

$$M_y^{(2)}(\omega) = (\mu_{13}^{em}\rho_{31} + \mu_{31}^{em}\rho_{13})_y \quad (2.76)$$

The M-E moment is the tensorial product of the electric dipole moment on the $|1\rangle \leftrightarrow |2\rangle$ transition and the magnetic dipole moment on the $|2\rangle \leftrightarrow |3\rangle$ transition

$$\mu_{31}^{em} = (e\vec{r})_{12} \left(\frac{\mu_0^{(m)}}{\sqrt{2}} \hat{L}_- \hat{O}_+ \right) \quad (2.77)$$

where $\mu_0^{(m)}$ is equal to the hydrogenic magnetic dipole transition moment on the $|2\rangle \leftrightarrow |3\rangle$ transition, \hat{L}_- is the electronic angular momentum lowering operator and \hat{O}_+ is the molecular angular momentum raising operator. The electric dipole moment $e\vec{r}_{12}$ is orientated along z , so only the magnetic dipole term emerges from a projection of the M-E moment along y . The magnetization thus reduces to

$$M_y^{(2)}(\omega) = \sqrt{2}\mu_{eff}^{(m)}(\rho_{31} + \rho_{13}) \quad (2.78)$$

where $\mu_{eff}^{(m)}$ is defined as the expectation value of $\mu_0^{(m)}\hat{L}_-\hat{O}_+$. Due to torque enhancement, it is shown in Ref. [49] that $\mu_{eff}^{(m)} = \frac{c\mu_0^{(e)}}{2}$. The final expression for the M-E magnetization that arises from the ρ_{13} coherence is

$$M_y^{(2)}(\omega) = \frac{c\mu_0^{(e)}}{\sqrt{2}} (\rho_{31} + \rho_{13}) \quad (2.79)$$

2.3 Theoretical Form of the Rectification Nonlinearity

The theoretical results shown above explicitly yield the intensity, frequency, and polarization dependence of M-E nonlinearities. In both theoretical approaches, the rectification appears as a quadratic M-E process jointly driven by the optical electric and magnetic fields. The joint action of the electric and magnetic field at the same frequency to generate M-E rectification is possible because rotational mixing creates an allowed magnetic dipole transition at the same frequency as the electric dipole transition. The addition of molecular torque in the coupled oscillator model amplifies the rectification moment and changes the rectification timescale to that of the molecular system rather than the electronic system. The density matrix model gives similar predictions, with the sole exception that the magnetization first appears in the second order in the density matrix analysis.

The coupled oscillator model predicts that the rectification nonlinearity is resonant on electric dipole transitions. The full form of Eqn. 2.13 for an arbitrary optical frequency is

$$z_0 = -\frac{1}{2} \frac{q^2 E_0 B_0}{m^2} \frac{\omega}{\sqrt{(\omega_0^2 - \omega^2) + \gamma^2 \omega^2}} \sin(\tan^{-1}(\frac{\gamma\omega}{\omega_0^2 - \omega^2})) \quad (2.80)$$

Based on Eqn. 2.80, z_0 is maximized when the optical frequency is tuned to the electronic resonance frequency ω_0 . The magnitude of the longitudinal displacement is further amplified by the coupling of the electronic motion to molecular rotations. The torque induced on the molecular model by the rectification moment can be directly calculated using Eqn. 2.22. The component of torque that drives rotational motion around the internuclear axis is

$$T_{\parallel} = m\omega_0^2(z_0 r_y) \quad (2.81)$$

It is noted that the y position of the restoring point can be expressed as $r\cos(\theta_{\parallel})$. When Eqn. 2.81 is inserted into Eqn. 2.20 and the differential equation is solved in steady state, the angle of the torsional oscillator is given by the following transcendental equation

$$\omega_m^2 \theta_{\parallel} = \frac{1}{I_{\parallel}} m\omega_0^2 z_0 r \cos(\theta_{\parallel}) \quad (2.82)$$

For small angles, this simplifies to

$$\theta_{\parallel} = \frac{mr}{I_{\parallel}} \frac{\omega_0^2}{\omega_m^2} z_0 \quad (2.83)$$

The z position of the restoring point is equal to $r\sin(\theta_{\parallel})$. The total z displacement of the electron relative to the center of mass of the molecule is then equal to the sum of the z displacement of the restoring point and the z displacement of the electron relative to the restoring point. The small angle approximation can again be taken for θ_{\parallel} .

$$z_{tot} = z_0 + r\sin(\theta_{\parallel}) = \left(\frac{mr^2}{I_{\parallel}} \frac{\omega_0^2}{\omega_m^2} + 1 \right) z_0 \quad (2.84)$$

From Eqn. 2.84, it can be seen that the effect of coupling the electron oscillator model to the rigid rotor model is to amplify the rectification by a factor of $\frac{mr^2}{I_{\parallel}} \frac{\omega_0^2}{\omega_m^2}$. Because I_{\parallel} is the moment of inertia for rotational motion around the internuclear axis, the nuclear masses which lie on that axis will not contribute to I_{\parallel} . The only mass that would contribute to I_{\parallel} is the electron mass at a distance r . The moment of inertia of rotational around the internuclear axis is thus equal to mr^2 , so $\frac{mr^2}{I_{\parallel}} \approx 1$. The $\frac{\omega_0^2}{\omega_m^2}$ term in Eqn. 2.84 is the square of the ratio between the electronic transition frequency and the molecular rotation frequency. In most molecules, this ratio is 10^3 or larger, so the torque enhancement factor shown in Eqn. 2.84 represents a 10^6 enhancement factor relative to the value caused by parametric resonance alone.

The amplification by molecular torque also means that the decay behavior of the rectification moment when the driving field is turned off will more closely match the timescale of the internal molecular motion than the electronic dynamics. If there is no driving field, the equations of motion for the electron and molecule given by Eqns. 2.1 to 2.3 and Eqn. 2.19 simplify to their homogeneous form. The solutions to these second order homogeneous equations are well known.

$$x = x_0 e^{\frac{-\gamma_e \pm \sqrt{\gamma_e^2 - 4\omega_0^2}}{2}} \quad (2.85)$$

$$\theta = \theta_0 e^{\frac{-\gamma_m \pm \sqrt{\gamma_m^2 - 4\omega_m^2}}{2}} \quad (2.86)$$

While the electron oscillator will return to its rest position at a timescale governed by γ_e and ω_0 as seen in Eqn. 2.85, the torsional oscillator will return to its rest position at a slower timescale that comes from γ_m and ω_m . Since the total z displacement of the electron in the coupled oscillator model is largely caused by angular displacement of the torsional oscillator, the rectification moment will decay at this slower timescale of rotational motion. The density matrix model similarly predicts that the rectification field will have a quadratic dependence on the optical field and will decay at a timescale characteristic of molecular motion. The M-E rectification moment arises from

the ρ_{13} coherence from Eqn. 2.70. If the system is driven to steady state and the driving field is then turned off, the free decay of the coherence is described by Eqn. 2.42.

$$i\hbar\dot{\rho}_{13} = -\hbar\omega_{13}\rho_{13} - i\hbar\Gamma_{31}\rho_{13} \quad (2.87)$$

This first order homogenous differential equation has the simple solution

$$\rho_{13}(t) = \rho_{13}(0)e^{i\omega_{13}t - \Gamma_{31}t} \quad (2.88)$$

The coherence will thus decay at a timescale governed by the coherence decay rate Γ_{31} . This decay rate is tied to the timescale of molecular motion that causes the rotationally excited state $|3\rangle$ to decouple from the ground state. Explicit examples of the time dependence of rectification signals are given in Chapter 4 with the results from the computational methods described in Chapter 3.

CHAPTER 3

Methods

In this chapter, the experimental and computational methods used to investigate M-E rectification are described. The experiment described in Section 3.1 and published in Ref. [2] measured the M-E induced second harmonic generation (SHG) in polycrystalline thin films. A novel crossed-beam pump-probe geometry was used that allowed for a highly sensitive measurement with ultrafast temporal resolution. Because all-electric second harmonic generation was prohibited in the sample by spatial inversion symmetry, the only possible source of a pump-induced second harmonic signal was either an electric quadrupole interaction or a pump-induced M-E rectification field. However in Chapter 4 it is shown that the electric quadrupole moment is identically zero, leaving only the magneto-electric possibility. A second experimental design based on the crossed-beam geometry is discussed in Section 3.2 which could directly measure the magnitude of the induced rectification field. In this second experiment, the polarization rotation of a probe beam would be measured to characterize the M-E rectification field produced by the pump beam.

In addition to these two experiments, two computational models were used to assess the effect that different experimental parameters and molecular properties have on the development of the M-E rectification moment. The first was a classical model developed for steady state illumination in Ref. [1] and extended in this thesis to model pulsed illumination, as described in Section 3.3.1. The second model was based on density matrix theory which introduced a semi-classical and time dependent description of magneto-electric interactions as seen in Section 3.3.2. The results from these experimental and computational investigations can be found in Chapter 4.

3.1 Second Harmonic Generation Induced by M-E Rectification

This section details the experimental methods used in the observation of M-E induced SHG. The experiment was designed to observe the M-E rectification field by detecting second harmonic radiation induced by the rectification field in a polycrystalline pentacene thin film sample. This

experiment used a crossed-beam pump-probe geometry with tilted pulse fronts. Tilting the pulse fronts of the pump and probe beams meant high temporal resolution could be achieved even though the pump and probe were not co-linear. A sample was chosen that possessed inversion symmetry on the scale of the optical wavelength. Second harmonic generation is prohibited in materials with inversion symmetry, so the only possible source of second harmonic generation in the bulk of the material would be dynamic symmetry breaking induced by the pump beam. This symmetry breaking made the detection of second harmonic radiation a highly sensitive method of detecting the M-E rectification field, as even a small rectification field would break the symmetry enough to allow second harmonic generation.

It should be noted that all-electric second harmonic generation could occur at the surfaces of the sample as well since inversion symmetry is broken at interfaces. However, the magnitude of the surface second harmonic generation has a different dependence on the polarization of the probe beam. By measuring the dependence of the signal on the probe polarization, the surface second harmonic generation can be distinguished from second harmonic generation arising from dynamic pump-induced symmetry breaking in the bulk of the sample. The portion of the detected signal that comes from the bulk of the sample can be directly attributed to a pump-induced M-E rectification field.

3.1.1 Crossed Beam Pump-Probe Geometry

The crossed beam pump-probe geometry used in the experiment was necessary due to the orientation of the M-E rectification field with respect to the direction of propagation of the incident field. In general, pump-probe experiments work by allowing two beams, the pump beam and probe beam, to travel co-linearly through a sample to achieve maximum overlap, with an adjustable delay between the two beams. The interaction between the pump beam and the sample generates a nonlinear polarization moment. When the probe beam travels through the sample, it interacts with the nonlinear polarization moment induced by the pump. This interaction alters the properties of the probe beam, which can then be measured to determine the properties of the pump-induced polarization moment. However, only the projection of the nonlinear polarization on the probe electric field direction has any effect on the probe.

As shown in Chapter 2, the M-E rectification field develops parallel to the direction in which the optical field is travelling. If the pump and probe are aligned along the same beam path as is usually the case in pump-probe experiments, the pump-induced M-E rectification field will be perpendicular to the plane of the probe polarization. This co-linear geometry would make it impossible for the probe beam to interact with the M-E rectification field. If the pump beam instead travels along a path to the sample that is 90° from the probe beam as shown in Fig. 3.1b, a pump-induced M-E

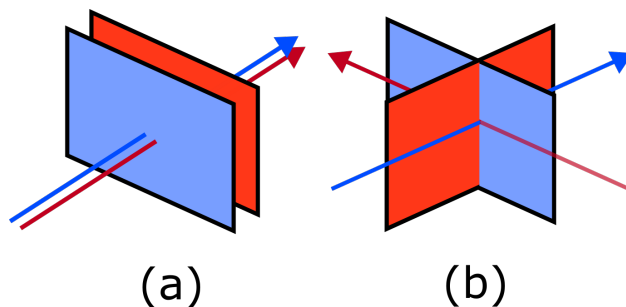


Figure 3.1: Diagram of the co-linear (a) and crossed beam (b) geometries. The pump beam is shown in red and the probe beam is shown in blue. The plane of polarization of the pump and probe are shown by the red and blue planes respectively.

rectification field would be in the same plane as the probe polarization. This new crossed-beam geometry would allow the probe beam to interact with the M-E rectification field, enabling the observation of the M-E rectification field.

3.1.2 Pulse-Front Tilt for Temporal Resolution

While altering the co-linear geometry to the crossed beam geometry allows the the M-E rectification field to interact with the probe beam in order for induced second harmonic generation to be measured, in general it limits the temporal resolution the setup can achieve. The temporal resolution determines how finely the temporal structure of the M-E rectification field can be determined. If the temporal resolution is too coarse, it would not be possible to experimentally observe the rise and decay behavior of the M-E rectification moment.

The temporal resolution of a pump-probe experiment is determined by the amount of delay that needs to be added between the two beams such that they no longer temporally overlap in the sample. This means that in a co-linear pump-probe experiment, the temporal resolution is limited only by the time duration of the pulse. Assuming the pump and probe pulses have the same time duration, delaying the probe pulse by a time equal to the pulse duration will cause the pulses to not overlap temporally in the sample. In a crossed beam geometry, the temporal resolution is instead limited by the transit time it takes the pump and probe beams to cross one another, which in turn is proportional to the diameter of the beam. For an ultrafast laser pulse with a time duration of 100 fs and a beam diameter of several millimeters, the temporal resolution in a crossed beam pump-probe configuration will be over 100 times lower than the temporal resolution in a co-linear configuration. Because the M-E rectification field persists for a time related to the speed of the molecule rotations of the sample as shown in Chapter 2, the entire field decays after a few picoseconds. Thus, flat pulse fronts will be unable to resolve the temporal characteristics of the M-E rectification field.

The decreased temporal resolution caused by using a cross-beam geometry can be overcome

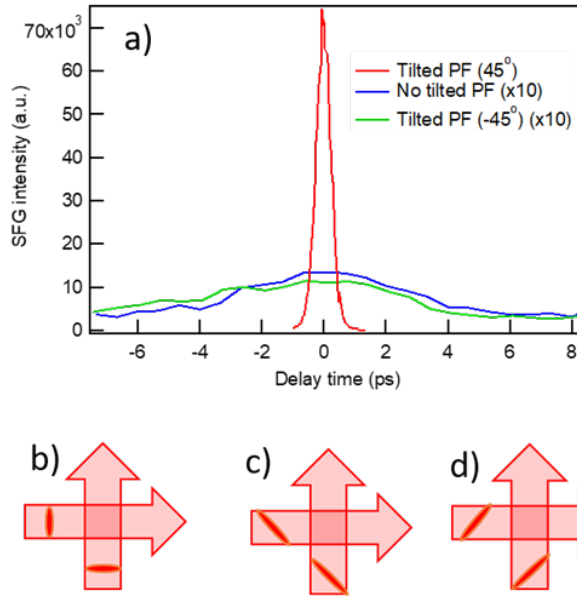


Figure 3.2: Use of tilted pulse fronts to improve temporal resolution (a) Plot of the SFG intensity as a function of relative delay between pump and probe beams. Diagram of the pump-probe interaction when pulse fronts are (b) flat, (c) tilted by 45° , or (d) tilted by -45° . The experiment uses case (c) to maximize the temporal resolution. Reprinted from Ref. [2].

by adding pulse front tilt to the pump and probe beams. Fig. 3.2a shows the temporal resolution of a crossed-beam pump-probe setup for three different values of the pulse front tilt shown in Fig. 3.2b-d. When the pulse front is flat or tilted by -45° , the temporal resolution of the setup is low and the signal is spread out over a long time period. However if the pulse front is tilted by 45° in the correct direction the ultrafast temporal resolution equal to the pulse width is restored. By tilting the pulse front of the pump and probe beams, the crossed-beam pump-probe setup is capable of measuring the M-E rectification field with the high temporal resolution required to observe the rise and decay of the rectification field.

3.1.3 Experimental Setup

A diagram of the experimental setup is shown in Fig. 3.3. The laser used to perform the pump-probe experiment was an ultrafast Ti:Sapphire system with a center wavelength of 800 nm. The laser produced pulses with a 100 fs pulse width and a pulse energy over 0.4 mJ at a 10 kHz repetition rate. The pulse front of the beam was first tilted. This was accomplished by diffracting the beam off of a grating. The first order diffracted beam was picked off by a concave mirror and reflected off of two flat mirrors into the rest of the setup. The diffracted beam then passed through a cylindrical lens. The combination of the concave mirror and cylindrical lens compensated for the

dispersion and chirp induced on the beam by the grating.

After passing through the cylindrical lens, the beam was split into the pump and probe arms. The pump beam was chopped and sent through an adjustable delay stage. Both the pump and probe beams passed through $\lambda/2$ wave plates so the pump and probe polarization could be independently controlled. The beams met at the sample. The inset in Fig. 3.3 shows how the tilted pulse fronts of the pump and probe beams met at the sample. The probe beam, along with any generated second harmonic radiation, then travelled through a bandpass filter centered at 400 nm. The bandpass filter removed any light remaining at the original laser wavelength, leaving only light at the second harmonic frequency of 400 nm. The second harmonic radiation was then detected by a photomultiplier tube (PMT), and the magnitude of the signal from the PMT was recorded along with the position of the delay stage. By moving the delay stage and recording the PMT signal as a function of the delay between the pump and probe, the temporal characteristics of the pump-induced M-E rectification field were resolved.

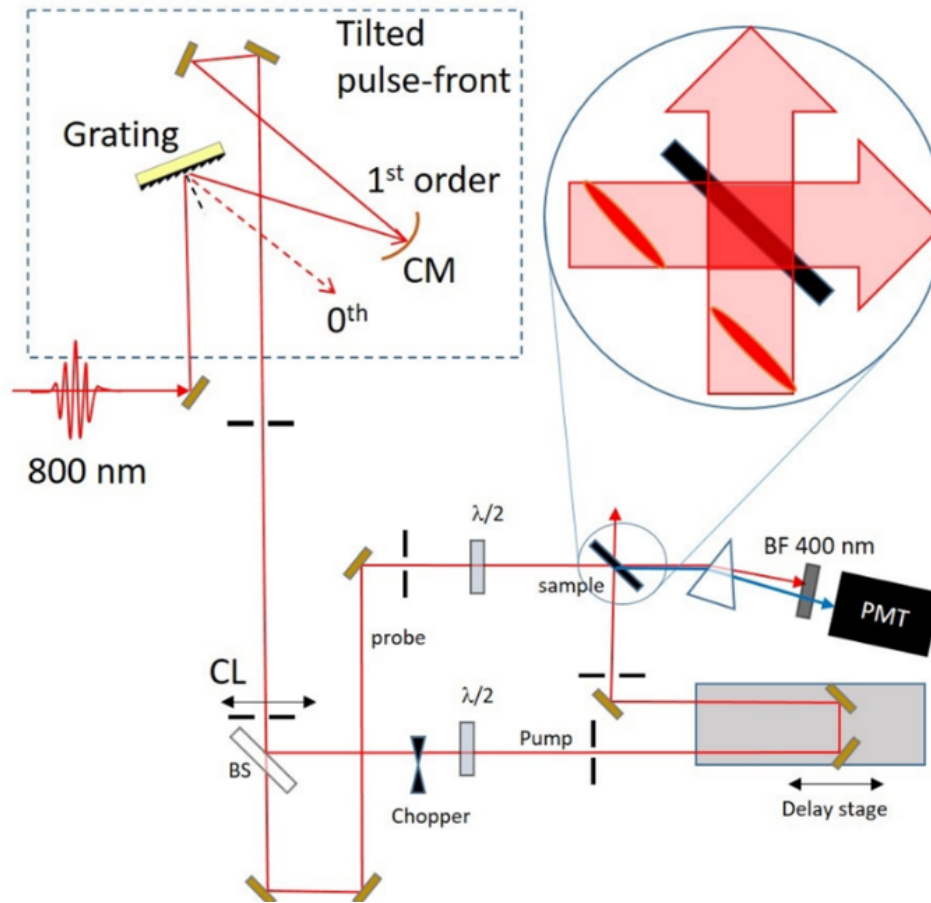


Figure 3.3: Experimental setup for the SHG experiment. The pulse front of the beam is tilted and then passes through a beamsplitter to generate the pump and probe beams. The pump beam is chopped and sent through an adjustable delay stage before it travels to the sample. After the probe beam passes through the sample, light at the laser wavelength of 800 nm is filtered out and the remaining light at the second harmonic wavelength of 400nm is collected by the PMT.

3.1.4 Alignment of the Experimental Setup

Temporal synchronization of the setup was achieved by using a gallium arsenide wafer and measuring the second harmonic radiation generated by the spatial and temporal overlap between the pump and probe beams. Due to the use of tilted pulse fronts and a crossed-beam geometry, the experimental setup was very sensitive to the alignment of the pump and probe beams on the sample. The pump and probe beams must overlap both spatially and temporally for the maximum signal to be achieved. The amount of second harmonic radiation produced through dynamic symmetry breaking of the sample with the M-E rectification field was small, so a gallium arsenide wafer was instead used for alignment. The wafer was placed at the location of the sample in the same orientation. The beams were coarsely aligned by eye to hit the same location on the wafer. The

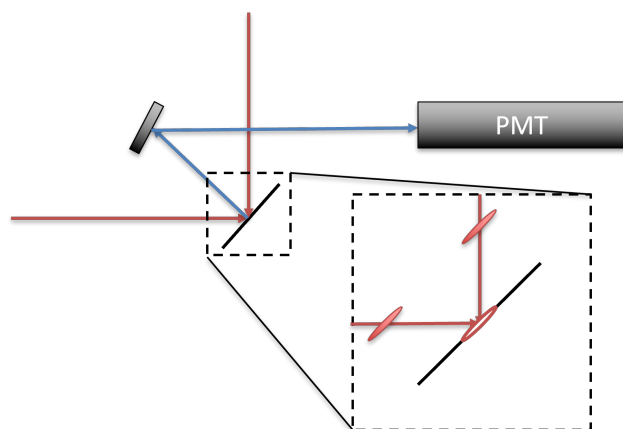


Figure 3.4: Experiment setup for alignment of the SHG setup. Second harmonic radiation is generated at the surface of the gallium arsenide wafer when the pump and probe beams spatially and temporally overlap. The second harmonic light is radiated perpendicular to the sample surface, where it is sent to the PMT for measurement.

delay stage was then scanned over a wide range. When the pump and probe beams spatially and temporally overlapped on the surface of the wafer, second harmonic radiation was generated along a direction perpendicular to the surface of the wafer. The generated light was collected at the PMT. The magnitude of the PMT signal was maximized by finely adjusting the pump and probe beam alignment. When the signal was maximized, the pump and probe had the best possible spatial overlap. The position of the delay stage that generated the best temporal overlap was also recorded. The wafer was then replaced by the sample for data collection.

3.1.5 Isolating the M-E SHG Signal

After the total SHG signal was recorded on the PMT, the component of the signal that was induced by the M-E rectification field was isolated from the component of the SHG signal that arose purely from all-electric surface second harmonic generation. While all-electric SHG was prohibited in the bulk of the material due to the inversion symmetry as will be shown in Chapter 4, the surface of the sample did not possess inversion symmetry for the component of the probe beam that was polarized perpendicular to the sample surface. Previous experiments have shown that second harmonic generation in pentacene is mostly caused by surface effects [54]. So all-electric second harmonic generation was possible at the surface of the sample. The total nonlinear polarization moment generated in the sample was thus a combination of the nonlinear polarization produced by the interaction of the probe with the M-E rectification field and the nonlinear polarization produced by the probe alone at the surface.

The total signal intensity measured by the detector was proportional to the square of the total

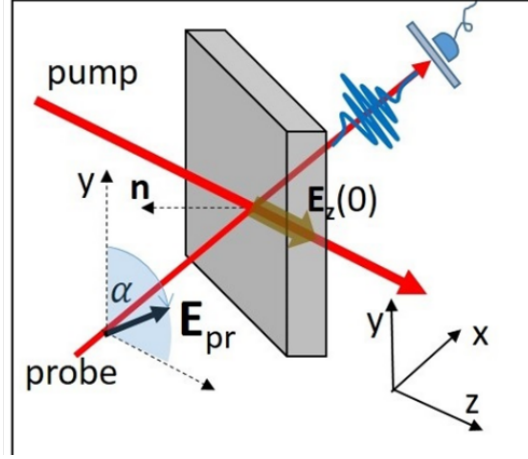


Figure 3.5: Geometry of the pump-probe interaction at the pentacene thin film sample. The lab axes are shown in the bottom right. The pump travels along the \hat{z} direction while the probe travels along the \hat{x} direction. The probe is polarized at an angle α from the \hat{y} axis.

nonlinear polarization moment, which can therefore be written as

$$S_{tot} \propto |P_{tot}|^2 = |P_{surf} + P_{M-E}|^2 = |P_{surf}|^2 + 2|P_{surf} \cdot P_{M-E}|^2 + |P_{M-E}|^2 \quad (3.1)$$

where S_{tot} was the total measured signal, P_{tot} was the total magnitude of the nonlinear polarization of the sample, P_{surf} was the surface component of the nonlinear polarization, and P_{M-E} was the M-E induced component of the nonlinear polarization. The first term in Eq. 3.1 has no dependence on the M-E induced polarization moment, while the second and third terms only appear if there is a M-E induced polarization moment in the sample. The M-E induced signal was distinguished from the surface-only signal by looking at how the signal measured at the PMT varied as the probe polarization was rotated. This was done by analyzing the geometry of the interaction between the pump and probe beams and the sample, as shown in Fig. 3.5 and described below.

The coordinate system was defined so that the pump beam travelled in the \hat{z} direction and the probe beam travelled in the \hat{y} direction. Then the probe polarization was located in the xz plane. As shown in Chapter 2, the M-E rectification field generated by the pump was oriented along its direction of propagation. Then the rectification field takes the form $E_z(0)$. When the rectification field was induced by the pump beam, it dynamically broke the symmetry of the sample along the \hat{z} direction. When the probe beam interacted with the region of broken symmetry, a nonlinear polarization moment was produced at the second harmonic frequency proportional to the rectification field.

$$P_{M-E}(2\omega) \propto E_z(0)E_0^2(\omega) \quad (3.2)$$

E_0 is the electric field of the probe beam. This M-E induced polarization moment is not dependent

on the probe polarization angle.

The surface component of the polarization moment takes a different form. Only components of the probe beam that are polarized perpendicular to the surface experience broken symmetry, and thus only these components contribute to surface SHG. Referring back to Fig. 3.5, the probe beam was always incident on the surface at a 45° angle. Hence the component of the probe beam perpendicular to the surface was

$$E_{\perp}(\omega) = E_0(\omega)\cos(45^\circ)\sin(\alpha) \quad (3.3)$$

where α is the angle between the probe polarization and the \hat{y} axis. The nonlinear polarization moment arising from the surface is proportional to the square of this field.

$$P_{\text{surf}}(2\omega) \propto E_{\perp}^2(\omega) = E_0^2(\omega)\cos^2(45^\circ)\sin^2(\alpha) \quad (3.4)$$

Note that the surface component of the polarization has a $\sin^2(\alpha)$ dependence on the probe polarization angle.

By substituting Eqns. 3.2 and 3.4 into Eqn. 3.1, we can determine the dependence of each term on the probe polarization angle α . The first term $|P_{\text{surf}}|^2$ has a $\sin^4(\alpha)$ dependence on the probe polarization, while the second term $2|P_{\text{surf}} \cdot P_{\text{M-E}}|^2$ has a $\sin^2(\alpha)$ dependence on α . The third term $|P_{\text{M-E}}|^2$ has no dependence on the probe polarization angle. Because these different signal components have different dependencies on the probe polarization, they can be distinguished by measuring the response of the signal to a rotation of the probe polarization. The component of the measured signal that has a $\sin^4(\alpha)$ dependence on the probe polarization cannot be attributed to the M-E rectification field, while signals which are proportional to $\sin^2(\alpha)$ or are independent of the probe polarization may be attributed to the pump-induced M-E rectification field.

3.2 Birefringence Induced by M-E Rectification

While the detection of induced second harmonic generation is a highly sensitive method of detecting the presence of a M-E rectification field, the indirect nature of this approach complicated the full characterization the rectification field. In this section, a more direct technique for observing the magnitude and timescale of the M-E rectification field by measuring induced birefringence is described. This second experimental technique is based on the same experimental structure of a crossed-beam pump-probe experiment with tilted pulse fronts used in the second harmonic generation experiment from Section 3.1. The detection setup was calibrated so that the magnitude of the signal could be directly related to the M-E pump-induced birefringence. The use of an isotropic

sample would rule out most all-electric nonlinearities that could mimic the signal from the M-E rectification field. The M-E induced birefringence could be distinguished from the remaining nonlinear interactions that can occur in isotropic media by looking at the dependence of the signal on the pump beam polarization.

3.2.1 Theory of M-E Induced Birefringence

The quasi-static M-E rectification field can induce birefringence in a sample by dynamically modifying the index of refraction for light polarized parallel to the rectification field. When light passes through a medium, the phase velocity of light inside the medium is given by the equation

$$v = \frac{c}{n} \quad (3.5)$$

where c is the speed of light in vacuum and n is the index of refraction of the medium. The index of refraction is not always constant, and in some materials it can depend on the polarization of the light. When a material has two indices of refraction for two orthogonal directions of polarization, it is said to be birefringent. Birefringence can also be induced in a material by an applied field. For example, when a static electric field is applied to a material, the index of refraction of that material for light polarized parallel to the field will change by an amount proportional to both the electro-optic coefficient of the material and the amplitude of the electric field.

$$\Delta n = \gamma \cdot |\vec{E}| \quad (3.6)$$

The index of refraction along other directions will remain the same, so applying a static field to a material will cause the material to become birefringent. As described in Chapter 2, although the M-E rectification field is ultrafast it does not oscillate at high frequencies and so can be considered quasi-static. The quasi-static rectification field can thus induce birefringence in a material.

$$\Delta n_{ME} \propto E_{ME}(0) \quad (3.7)$$

More precisely, the rectification field can interact with a beam $E(\omega)$ travelling through a material to generate a nonlinear polarization moment that oscillates with frequency ω

$$P_{NL}(\omega) = \chi_{NL}\epsilon_0 E_{ME}(0)E(\omega) \quad (3.8)$$

where χ_{NL} is the value of the nonlinear susceptibility. The total polarization in the material that oscillates at ω is equal to the sum of the linear and nonlinear contributions.

$$P_{tot}(\omega) = P_L(\omega) + P_{NL}(\omega) \quad (3.9)$$

Because the linear contribution P_L and P_{NL} are both proportional to $\epsilon_0 E(\omega)$, $P_{tot}(\omega)$ can be rewritten to see that the magneto-electric induced polarization moment changes the effective linear susceptibility.

$$P_{tot}(\omega) = (\chi_L + \chi_{NL} E_{ME}) \epsilon_0 E(\omega) = \chi_{eff} \epsilon_0 E(\omega) \quad (3.10)$$

Assuming the nonlinear polarization is small and that the material magnetization is negligible, the induced birefringence can be found by calculating the refractive index from χ_{eff} and subtracting the unperturbed index of refraction.

$$\Delta n_{ME} = \frac{1}{2} \chi_{NL} E_{ME}(0) = \frac{1}{2} \chi_{ME} E H^* \quad (3.11)$$

For more details, see Appendix A.

The M-E induced birefringence can be measured by using a probe pulse to compare the original index of refraction to the modified index of refraction. The presence of the rectification field will modify the index of refraction for only the component of the probe beam polarized parallel to the rectification field. If part of the probe pulse is linearly polarized parallel to the rectification field and part is linearly polarized perpendicular to the rectification field, the two polarization components will travel at different speeds through the material when the rectification field is present. This difference in speeds means that the polarization component parallel to the rectification field will acquire a delay relative to the other polarization component. For any given point along the path of the probe beam, one polarization component will arrive before the other. This will cause the polarization of the beam to appear to rotate. In effect, the original linear polarization is converted into elliptical polarization by an amount proportional to the amount of induced delay between the two polarization components. The amount of ellipticity introduced to the probe polarization can then be measured to determine the magnitude of the induced delay, which in turn can be used to calculate the magnitude of the M-E rectification field. In this way, the measurement of the M-E induced birefringence permits a direct calculation of the magnitude of the M-E rectification field. The 90° cross-beam geometry used in this experiment is not normally used in birefringence experiments - the pump and probe beam are either co-linear [55; 56] or cross at a small angle [57]. The birefringence induced by M-E rectification thus cannot significantly affect the signal measured in these experiments as the co-linear or nearly co-linear geometry does not allow the rectification field to interact with the probe beam.

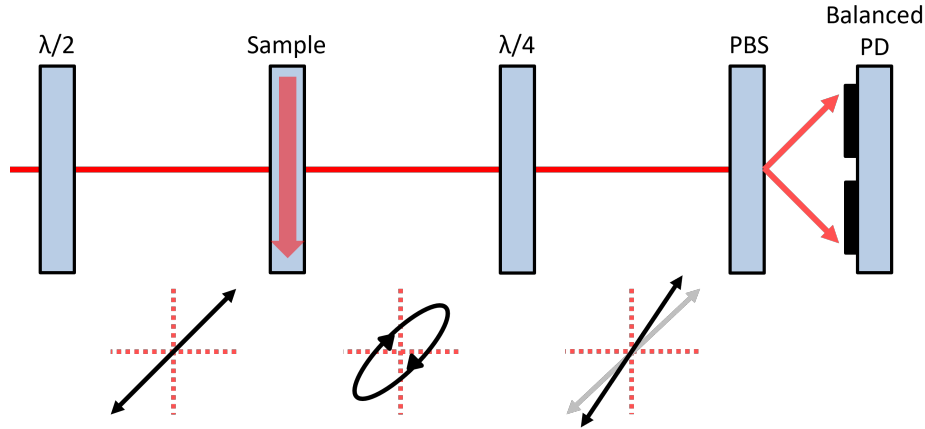


Figure 3.6: Concept of the M-E induced birefringence experiment. The probe beam is linearly polarized at 45° by the first $\lambda/2$ waveplate. The presence of the M-E rectification field in the sample modifies the probe polarization state by adding ellipticity. The $\lambda/4$ waveplate converts this ellipticity into a linear polarization rotation. The horizontal and vertical components of the pump beam are separated and the difference in power between them is measured.

3.2.2 Experimental Setup

A diagram of the experimental setup is shown in Fig. 3.7. The same ultrafast Ti:Sapphire laser that was described in Sec. 3.1 was used in this experimental design. The beam travelled through the pulse-front tilt setup and acquired a 45° pulse front tilt. The laser beam was then split into the pump and probe beams. The pump beam passed through a chopper and a delay stage before it hit the sample, which allowed adjustment of the relative timing of the pump and probe beams. The probe beam was rotated to 45° and then passed through the sample. The sample to be used in this experiment was liquid CCl_4 . The liquid was placed in a quartz cuvette with lateral dimensions of $10 \times 10 \text{ mm}^2$. The cuvette of liquid was held in place by a Thorlabs cuvette holder. When the probe beam passed through the sample, its polarization state was changed by the presence of a pump-induced M-E rectification field. The original 45° linear polarization was modified by the addition of a small amount of ellipticity. The probe beam then passed through a series of waveplates which converted the induced ellipticity into a rotation of the linear polarization. The probe beam was then focused into an all-fiber polarized beamsplitter. This beamsplitter separated the probe beam into horizontal and vertical components, which were sent into the plus and minus ports of a balanced photodetector. The balanced photodetector generated an output signal proportional to the difference in intensity of the light on the plus and minus ports.

In order for the photodetector to properly subtract the two signals, it is critical that the two polarization components were incident on the two ports of the detector at the same time. The photodetector used in the experiment has a slight asymmetry where the response times of the plus

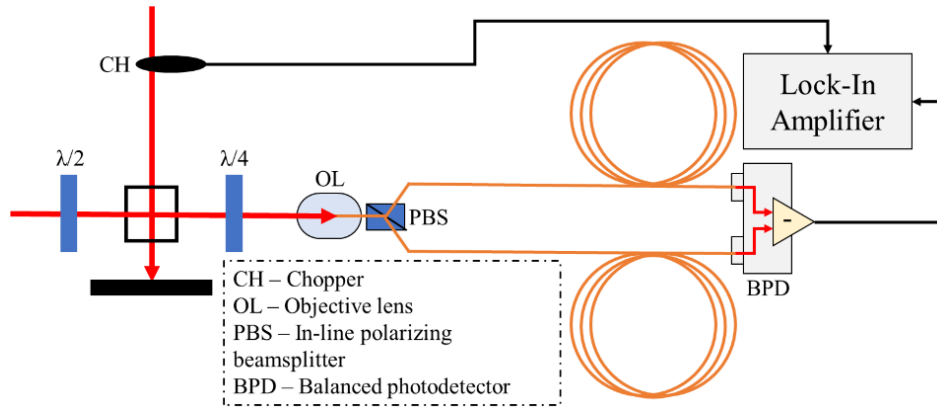


Figure 3.7: Diagram of the experimental setup for the M-E induced birefringence experiment. After passing through the sample, the probe beam was focused into a polarization maintaining fiber (PMF) which was coupled into an in-line polarized beamsplitter. The two polarization components then travelled through 1 m of PMF to the two input ports of the balanced photodetector and the amplified difference between the photocurrent generated in each port is sent to the lock-in amplifier.

and minus ports were not identical. To partially counteract this difference in response time, an extra 1 m length of fiber could be added to the port with the faster rise time. A fiber with length 0.5 m would be added to the other port so that coupling losses on the two ports remained the same. The signal from the balanced photodetector would subsequently be sent to a lock-in amplifier to filter out signals that occurred at frequencies other than the chopping frequency. To carry out the experiment, the position of the pump delay stage would be varied, and the signal from the lock-in amplifier would be recorded along with the position of the delay stage. The pump-induced M-E rectification field could be characterized by looking at the lock-in signal as a function of the delay stage positioning.

3.2.3 Alignment of the Experimental Setup

The experimental setup can be aligned by measuring the two photon fluorescence produced in a solution of Rhodamine 6G dye in methanol. Because a liquid sample was used, a different alignment procedure from the one outlined in section 3.1.3 is required. As in the second harmonic radiation experiment, the experimental setup is very sensitive to the alignment of the pump and probe beams on the sample. The pump and probe beams must overlap both spatially and temporally for the maximum M-E induced birefringence signal to be achieved. The Rhodamine 6G solution was chosen for the alignment procedure because strong two-photon fluorescence was visible when overlapped pulses were incident at the laser wavelength of 800 nm.

A diagram of the alignment process is displayed in Fig. 3.8. For coarse alignment, pinholes

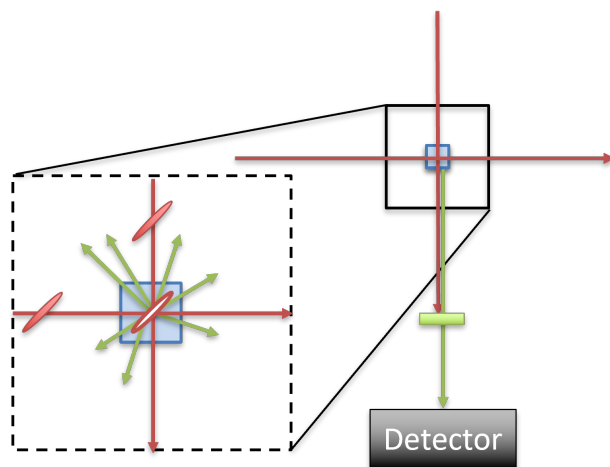


Figure 3.8: Diagram of the two-photon alignment setup. The pump and probe beam temporally and spatially overlap in the Rhodamine 6G solution in methanol. The pump output port is used to collect the two-photon fluorescence (shown by green arrows). The pump beam at 800 nm is filtered out by a narrow band pass filter centered at the fluorescence wavelength.

are attached to each of the four ports of the cuvette holder. The pump and probe beam are aligned through the pinholes and are confirmed visually to spatially overlap in the dye solution. Once the beams were coarsely aligned, a fiber coupling lens was attached to the output port of the pump beam. A band pass filter is also installed to filter out the pump beam so that only the two-photon fluorescence would reach the fiber coupling lens. The lens couple the fluorescence into a 1 m multimode fiber. The fiber is attached to the input port of an avalanche photodiode. The output of the photodiode is next sent to a lock-in amplifier whose output is recorded. The position of the delay stage was varied over a wide range in order to find the position of the delay stage that resulted in the highest lock-in signal. Once this point is found, fine adjustment of the pump and probe beams can be performed to maximize the lock-in signal. The position of the stage that generated the best temporal overlap is recorded as the zero delay position and the dye solution is removed.

3.2.4 Calibration of the Experimental Setup

Before the experimental sample was put in place following alignment, calibration was performed to determine the settings of the waveplates and probe polarization that resulted in the most sensitive detection of birefringence. The proportionality constants that related the lock-in voltage signal to the magnitude of the M-E induced birefringence were also measured. A conceptual diagram of the setup used for the experimental calibration is shown in Fig. 3.9. The sample and $\lambda/4$ waveplate were replaced by a second $\lambda/2$ waveplate. A rotation of the second waveplate by an angle α

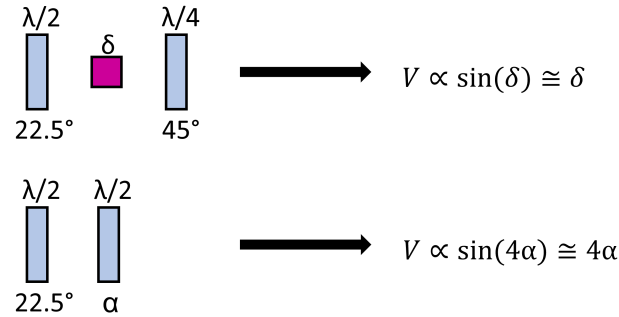


Figure 3.9: Concept of the calibration setup. The experimental setup is shown on top while the modifications made for calibration are shown on the bottom. For a pump-induced phase delay in the experimental sample of δ , the lock in voltage signal will be proportional to $\sin(\delta)$. Replacing the sample and the $\lambda/4$ waveplate with a second $\lambda/2$ waveplate at an angle α from 22.5° results in a voltage signal proportional to $\sin(4\alpha)$.

introduced the same amount of polarization rotation as a M-E induced phase delay of $\alpha/4$. By measuring the lock-in amplifier signal as a function of the angle α , its magnitude was related to the amount of phase delay and thus the birefringence induced in the sample. This allowed the direct measurement of the magnitude of the M-E rectification field. To perform this calibration, the following technique was used:

1. Remove all waveplates from the probe beam path. While monitoring the signal from the balanced photodetector on the oscilloscope, rotate the all-fiber beamsplitter until the signal from the Input(+) channel of the photodetector is maximized and the signal from the Input(-) channel is minimized. This aligns the axes of the polarization maintaining fiber with the laser polarization axis.
2. Add the first $\lambda/2$ waveplate. Rotate the waveplate until the signals in the Input(+) and Input(-) channel are equal. Once the signals are equal, fine-tune the waveplate angle by minimizing the signal in the amplified different output. Record the waveplate angle at which the amplified difference output is minimized
3. Remove the first $\lambda/2$ waveplate and put in the second $\lambda/2$ waveplate. Repeat the previous step for the second waveplate.
4. Add the first $\lambda/2$ waveplate back into the setup. Rotate the chopper so it chops the probe beam and turn on the chopper. Monitor the signals from the Input(+) and Input(-) channels on the oscilloscope and monitor the amplified difference signal on the lock-in amplifier.
5. Block the laser beam and record the background noise of the laser.

6. Rotate the second $\lambda/2$ waveplate in one direction until the signal from either the Input(+) or Input(-) channels just begins to saturate.
7. Rotate the second $\lambda/2$ waveplate in the opposite direction and record the lock-in signal at each position of the $\lambda/2$ waveplate. Continue doing this until reaching a waveplate position at which the other Input channel saturates. Discard any data points that were recorded with either Input channel saturated, as this can introduce error into the amplified difference signal.

A sinusoidal function of the theoretical detector response function $V = m \sin(\alpha) + b$ was fitted to the data recorded in the calibration procedure. The data and sinusoidal fit are displayed in Fig. 3.10. The sinusoidal fit is a good match to the data. For a very small induced birefringence, the detector response can be approximated as the linear function $V = m\alpha + b$. The sensitivity of the detector $\frac{dV}{d\alpha}$ is then simply m . This sensitivity is defined in terms of the rotation angle α of the second $\lambda/2$ waveplate in the calibration procedure. The sensitivity of the detector response with respect to a pump-induced phase δ can be found by observing that $\frac{dV}{d\alpha}$ is 4 times larger than $\frac{dV}{d\delta}$. Using the values shown in Fig. 3.10, the detector sensitivity to an induced phase delay is

$$\frac{dV}{d\delta} = 5 \cdot 10^{-4} V / rad \quad (3.12)$$

For measured voltage V , the phase delay that induced it is given by

$$\delta = \frac{V}{\frac{dV}{d\delta}} \quad (3.13)$$

The phase delay can be related to the induced birefringence Δn by the laser wavelength λ and the interaction length L .

$$\Delta n = \frac{\lambda \delta}{2\pi L} \quad (3.14)$$

The above equations can be rearranged to obtain an expression for the induced birefringence as a function of the voltage signal

$$\Delta n = \frac{\lambda V}{2\pi L \frac{dV}{d\delta}} \quad (3.15)$$

The induced birefringence can be directly related to the magnitude of the M-E rectification field. For more details, see Appendix A. Background noise was measured to be $V \approx 10^{-7}$ V, so the minimum resolvable birefringence signal assuming a signal to noise ratio of 1 was $\Delta n_{min} = 1.6 \cdot 10^{-8}$ for a interaction length of 2 mm. This is comparable to the resolution observed in birefringence experiments with similar methods of detection [58].

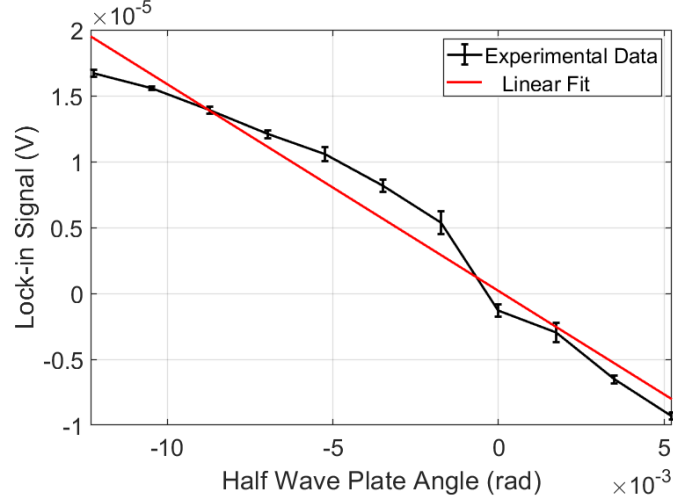


Figure 3.10: Plot of the voltage signal from the lock-in amplifier as a function of the angle of the second $\lambda/2$ waveplate. The experimental data is shown in black, while a linear fit $ax + b$ is shown in red with fitting parameters $a = -1.57 \cdot 10^{-3}$ and $b = 1.9 \cdot 10^{-7}$. A linear fit is appropriate given the small angles involved. The error bars on the experimental data correspond to the X_{noise} value calculated by the lock-in amp.

3.2.5 Isolation of the M-E Induced Birefringence

To prove that the pump-induced birefringence was indeed caused by the M-E rectification moment, it is crucial that other mechanisms for obtaining pump-induced birefringence were ruled out or minimized. Second-order, all-electric nonlinearities such as the electro-optic effect that would induce rectification in the sample were ruled out by choosing a sample that did not support these nonlinearities. The sample chosen for the experiment was carbon tetrachloride (CCl_4). Due to the symmetric structure of this molecule, it is totally isotropic and the electro-optic coefficient is zero. The other nonlinear effect that could induce birefringence is the Kerr effect. The Kerr-induced birefringence takes place in all materials, so the choice of a symmetric sample cannot rule out the presence of this effect. Additionally, the magnitude of the Kerr birefringence has the same dependence on pump power as the magnitude of the M-E induced birefringence. The nonlinear polarization moment $P^{(3)}(\omega)$ responsible for Kerr-induced birefringence is proportional to the square of the pump field E_{pump} .

$$P^{(3)}(\omega) = \chi_{\text{Kerr}} E_{\text{pump}}(\omega) E_{\text{pump}}^*(-\omega) E_{\text{probe}}(\omega) \propto E_{\text{pump}}^2 \quad (3.16)$$

Similarly, the magneto-electric induced birefringence is shown in Eqn. 3.11 to be proportional to $EH^* \propto E^2$. Thus the contribution to the pump-induced birefringence that arose from the Kerr effect must be separated from the M-E induced birefringence in other ways.

3.2.5.1 Signal Timescale

It is worth noting that the extended timescale of the M-E rectification nonlinearity potentially distinguishes it from the much faster timescale of the Kerr interaction. In experiments measuring the optical Kerr effect, there are two components of the birefringence signal. The first is the coherent part of the signal, which is observed only when the pump and probe directly overlap. This component of the signal will have a timescale that matches the timescale of the pump pulse. The second is the reorientational component which has an extended timescale that depends on the molecular properties of the sample. However the sample in this work is isotropic so no reorientational component of the signal is expected. Thus the only finite contribution to the Kerr birefringence signal is the coherent component which has a timescale that matches the pulse duration. The M-E rectification field on the other hand will have an extended timescale that is related to molecular rotational motion, so a birefringence signal that persists well after the pump beam has passed through the sample can only be caused by a pump-induced M-E rectification field.

3.2.5.2 Sign of Signal

In addition to the difference in timescale, the birefringence induced by the M-E rectification field should have the opposite sign as birefringence induced by the Kerr effect. In the lab coordinate system, the pump polarization lay in the xy plane and the rectification field was always oriented in the \hat{z} direction. Because the probe beam crossed the sample at 90° from the pump beam, the probe beam travelled in the \hat{y} direction and was polarized such that the \hat{x} and \hat{z} components of the probe were equal. Due to the symmetry of the sample, the \hat{y} component of the pump beam cannot induce birefringence as the induced polarization moments along \hat{x} and \hat{z} are equal.

$$P_x = \chi_{xyyx} E_y E_y E_x = \chi_{zyyz} E_y E_y E_z = P_z \quad (3.17)$$

Thus only the \hat{x} component of the pump polarization will contribute to Kerr-induced birefringence. This means that the Kerr effect can only increase the index of refraction for the component of the probe beam aligned along \hat{x} as the diagonal tensor element χ_{xxxx} is greater than the off diagonal χ_{zxzx} . Since the probe beam is polarized at 45° from the \hat{x} axis on the xz plane, the Kerr effect will cause clockwise rotation of the probe polarization as shown in Fig. 3.11. Similarly, the M-E rectification field can only increase the index of refraction for the \hat{z} component of the probe, so M-E induced birefringence will cause counterclockwise rotation of the probe polarization. The voltage signal from the lock-in amplifier would be positive when the probe polarization is rotated counterclockwise and negative when the probe polarization is rotated clockwise. Thus a positive voltage signal would be indicative of M-E induced birefringence.

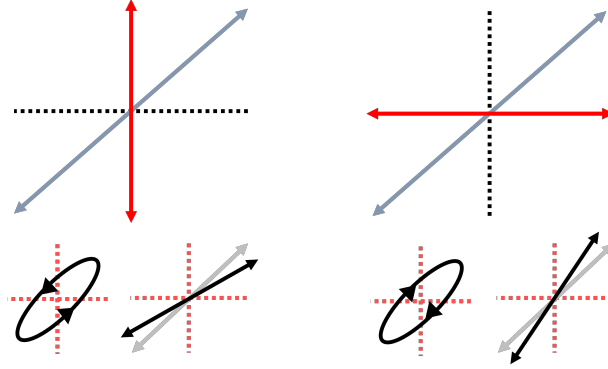


Figure 3.11: Sensitivity of the signal to direction of polarization rotation. If phase delay is accumulated on the \hat{x} -polarized component of the probe beam as shown on the left, the polarization will undergo clockwise rotation. For phase delay that accumulates on the \hat{z} -polarized component of the probe, the polarization is rotated in a counterclockwise direction

3.2.5.3 Pump Polarization Dependence

The use of a crossed-beam geometry also implies that the Kerr effect contribution to the birefringence signal depends on the pump polarization, while the M-E birefringence signal should be polarization-independent. If the pump polarization was rotated in the xy plane, the component of the pump that lies in the same plane as the probe polarization changed. This changed the strength of the Kerr contribution to the birefringence, as it was directly proportional to the magnitude of the pump beam that lay in the same plane as the probe polarization. As discussed in Chapter 2, the M-E rectification field does not depend on the polarization of the pump field because it always developed parallel to the direction of propagation of the pump beam. So the M-E birefringence signal would not show any dependence on the pump polarization. For a more detailed analysis of the polarization dependence of the signal, see Appendix A.

3.3 Computer Simulations of M-E Rectification

In addition to the second harmonic generation experiment described above in Sections 3.1, two computational models were used to study the temporal development of the M-E rectification field. The parameters of these simulations could be varied more widely than could be achieved experimentally, which provided a broad understanding of the physics of M-E interactions. A classical model first described in Ref. [1] was updated to simulate pulsed excitation. By numerically solving the coupled oscillator equations of motion from Chapter 2, the model provided an intuitive understanding of the dynamics that occur in M-E interactions. The density matrix theory from Chapter 2 was modified to include a time-dependent excitation pulse. The differential equations

for the populations and coherences of the time-dependent system were numerically solved to find the nonlinear M-E rectification moment.

3.3.1 Classical Model of M-E Rectification

The equations of motion for the coupled oscillator model of M-E rectification described in Chapter 2 were numerically solved by a Matlab differential equation solver. The time-dependent solution for the M-E rectification moment was extracted, and the process was repeated over a wide range of values of the model parameters. The changes in the numerical solution for the M-E rectification moment were analyzed to understand the processes that most affect the development of the M-E rectification field.

In order to use the built-in Matlab differential equation solver, the equations of motion first needed to be expressed in a form that the equation solver could recognize. While the coupled differential equations described in Chapter 2 are second order in time, the built-in Matlab solvers can only process first order differential equations. Thus the equations needed to be rewritten as a collection of first order differential equations. This was accomplished by introducing \vec{v}_e , Ω_{\parallel} , and Ω_{\perp} to represent the electron velocity and rigid rotor angular velocity.

To improve computational stability, several approximations to the equations of motion were made. The location of the rest position of the electron was tracked in Cartesian coordinates, separate from the rotational position of the rigid rotor oscillator. The rotational position of the rigid rotor was expressed in terms of the angles between its original and current position for all three Cartesian axes. These changes were made because the Matlab differential equation solver could not simultaneously solve the coupled equations of motion in both Cartesian and spherical coordinates. The approximation of the position of the rigid rotor was valid as long as the motion of the rigid rotor was largely confined to a single plane. The validity of the approximation was tested by varying the ratio between I_{\perp} and I_{\parallel} and measuring the residual energy in the model at the end of the simulation time. Fig. 3.12 shows the result of the test. For large values of $\frac{I_{\perp}}{I_{\parallel}}$, the residual energy is low. This indicates both the electron and rigid rotor oscillator returned to their original position, so the remaining potential energy in the simulation approaches zero. For lower values of $\frac{I_{\perp}}{I_{\parallel}}$, residual energy is high. The high residual energy occurs when the motion of the rigid rotor is no longer confined to a single plane. The approximation of the rigid rotor position breaks down, and the electron oscillator and rigid rotor oscillator decouple. To avoid this instability, the value of $\frac{I_{\perp}}{I_{\parallel}}$ was fixed to 1000 where the approximations remained valid.

The modified versions of the differential equations were then:

$$\dot{x}_e = v_{xe} \tag{3.18}$$

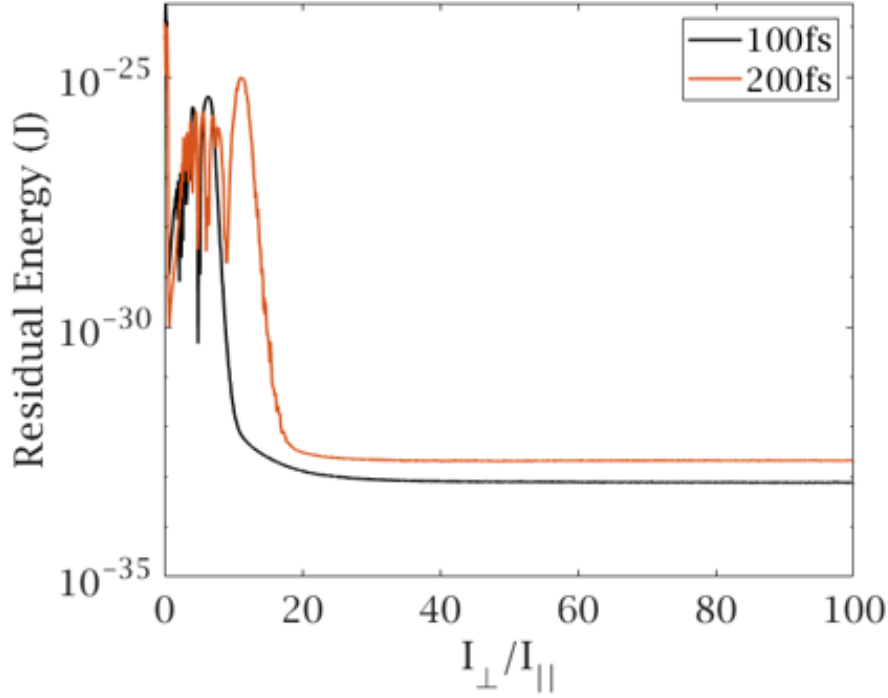


Figure 3.12: Stability of the classical model for pulsed excitation for 100 fs (black) pulses and 200 fs (red) pulses. For values of the ratio $\frac{I_{\perp}}{I_{\parallel}}$ below 20, the residual energy in the system rises sharply. For larger values of $\frac{I_{\perp}}{I_{\parallel}}$, the residual energy levels off at a low value.

$$\dot{y}_e = v_{ye} \quad (3.19)$$

$$\dot{z}_e = v_{ze} \quad (3.20)$$

These equations for the electron position \vec{x}_e are required to convert the second order equations of motion into a system of first order equations. The rest of the equation of motion can be stated as a first order differential equation in terms of the electron velocity \vec{v}_e .

$$v_{xe} = \frac{e}{m} E_x(t) - \omega_0^2(x_e - x_r) - \frac{e}{m} \frac{E_x(t)}{c} v_{ze} - \gamma_e v_{xe} \quad (3.21)$$

$$v_{ye} = -\omega_0^2(y_e - y_r) - \gamma_e v_{ye} \quad (3.22)$$

$$v_{ze} = -\omega_0^2(z_e - z_r) + \frac{e}{m} \frac{E_x(t)}{c} v_{xe} - \gamma_e v_{ze} \quad (3.23)$$

The position of the restoring point \vec{x}_r needed to be tracked in Cartesian coordinates to use in Eqns. 3.21-3.23.

$$\dot{x}_r = (z_r \Omega_y - y_r \Omega_z) \quad (3.24)$$

$$\dot{y}_r = (-z_r\Omega_x + x_r\Omega_z) \quad (3.25)$$

$$\dot{z}_r = (y_r\Omega_x - x_r\Omega_y) \quad (3.26)$$

The equations of motion for the rigid rotor oscillator must similarly be written as a system of first order differential equations by introducing the angular velocity Ω_i around a cartesian axis \hat{i} .

$$\dot{\theta}_x = \Omega_x \quad (3.27)$$

$$\dot{\theta}_y = \Omega_y \quad (3.28)$$

$$\dot{\theta}_z = \Omega_z \quad (3.29)$$

The rest of the rigid rotor equations can be written in terms of Ω_i .

$$\dot{\Omega}_x = \frac{m}{I_{\parallel}}\omega_0^2(y_r z_e - y_e z_r) - \gamma_m \Omega_x - \omega_m \theta_x \quad (3.30)$$

$$\dot{\Omega}_y = \frac{m}{I_{\perp}}\omega_0^2(-x_r z_e + x_e z_r) - \gamma_m \Omega_y - \omega_m \theta_y \quad (3.31)$$

$$\dot{\Omega}_z = \frac{m}{I_{\perp}}\omega_0^2(x_r y_e - x_e y_r) - \gamma_m \Omega_z - \omega_m \theta_z \quad (3.32)$$

For the complete Matlab code used, see Appendix B.

3.3.2 Density Matrix Model of M-E Rectification

The development of the density matrix theory of M-E interactions permitted the development of a time-dependent numerical model that solved the equations of motion the sample three level system laid out in Chapter 2. The density matrix equations of motion were solved using the built-in Mathematica differential equation solver. A time-dependent solution for the M-E rectification moment was computed from the third order coherence ρ_{13} . The time-dependent density matrix equations of motion are obtained by swapping the original expression for the driving field from Chapter 2 for a simulated Gaussian pulse.

$$V = -\frac{\hbar\Omega}{2} e^{-2\ln(2)\left(\frac{t-t_0}{\tau}\right)^2} e^{i\omega t} \quad (3.33)$$

The first order coherence ρ_{12} that arises from this driving field has an analytic solution. The analytic solution is used to minimize the amount of numerical error introduced in to the solution.

$$\rho_{12} = -\frac{\sqrt{\pi}}{4\ln(4)} e^{(-\Gamma_{12} + i\omega_{12})t} e^{\frac{(\Gamma_{12} + i(\omega - \omega_{12}))(\Gamma_{12}\tau^2 + i\tau^2(\omega - \omega_{12}) + 4t_0\ln(4))}{4\ln(4)}} \Omega t$$

$$\left(\operatorname{Erfi} \left[\frac{i\Gamma_{12}\tau^2 + \tau^2(\omega - \omega_{12}) + 4it_0\ln(2)}{2\tau\ln(4)} \right] - \operatorname{Erfi} \left[\frac{i\Gamma_{12}\tau^2 + \tau^2(\omega - \omega_{12}) - 4i(t - t_0)\ln(2)}{2\tau\ln(4)} \right] \right) \quad (3.34)$$

Given this analytic expression for the first order coherence, Eq. 2.70 for the second order term for ρ_{13} were solved. A numerically solution for the rectification field can then be obtained using Eq. 2.72. The complete Mathematica code used can be seen in Appendix C.

CHAPTER 4

Results

This chapter covers the experimental and theoretical results from the methods described in Chapter 3. Results from the induced second harmonic generation experiment are presented in Section 4.1 and have been published in Ref. [2]. A strong pump-induced second harmonic signal was observed when the pump and probe beams overlapped temporally in the thin film sample, in addition to a static background signal. The power and polarization dependence of the pump-induced signal were found to be consistent only with M-E induced SHG. The duration of the pump-induced signal was larger than the duration of the pump beam or the temporal resolution of the detector which matched the theoretical predictions from Chapter 2. These experimental results provided the first observation of the magneto-electric rectification moment.

Theoretical results from the coupled oscillator model and the density matrix model are covered in Sections 4.2 and 4.3. The outputs from both models exhibited an extended rectification duration that was greater than that of the driving pulse. The duration of the output of the coupled oscillator model depended most on the electronic damping rate and the molecular rotational frequency. Analysis of the peak rectification moment reached for different driving pulse widths showed the ultrafast torque completion time. The temporal duration of density matrix model output was solely dependent on the values of the Γ_{13} decoherence rate and the molecular rotational frequency. Results from the two computational models are compared in Section 4.4.

4.1 SHG Experiment

4.1.1 Sample Properties

The sample used in this experiment was a polycrystalline pentacene thin film. Polycrystalline pentacene was chosen because it possessed inversion symmetry on the scale of the laser wavelength. It also exhibited low absorption at the laser wavelength of 800 nm. The pentacene was deposited on a glass substrate by vacuum thermal evaporation. After preparation, the sample was sealed in an

inert gas environment and stored away from light to avoid degradation. The total thickness of the thin film was approximately 400 nm. Individual crystallites within the thin film had sizes between 100 nm and 200 nm, as seen in Fig. 4.1. The sizes of the crystallites were much smaller than the 800 nm wavelength of the laser, so the orientation of the individual pentacene molecules was effectively random on the scale of the laser beam. This meant that the sample possessed inversion symmetry, because if the sample was rotated by 180° it would not change the random orientation of the crystallites. All-electric SHG in samples with inversion symmetry is prohibited because any second order interaction of the field with the sample that produces a nonlinear polarization moment also produces a symmetric response in the opposite direction. These two polarization moments have equal magnitude but opposite sign and thus cancel out.

The absorption spectrum of the sample was measured with a spectrophotometer and is shown in Fig. 4.1. The absorption peak was found at 670 nm, with a tail that extended only out to 750 nm. The absorption at the laser wavelength of 800 nm was negligible, so the pump and probe beams could not cause a transition to an excited state that could generate a charge separation field in the sample. Additionally, the absorption of the pentacene at the second harmonic wavelength of 400 nm is also low. This meant that most of the generated second harmonic radiation would escape the sample and could be measured at the PMT.

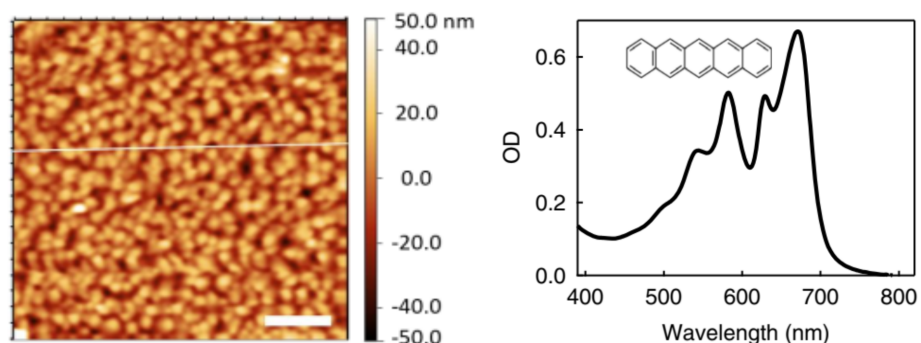


Figure 4.1: (a) AFM height image of the 400 nm thick pentacene film deposited on glass. The scan size is $5 \times 5 \mu\text{m}^2$ and the scale bar in the image corresponds to $1 \mu\text{m}$. The individual crystallites have a size between 100 nm and 200 nm. (b) The absorption spectrum of the sample. The absorption of the sample is very low at the laser wavelength of 800 nm, and relatively low at the second harmonic wavelength of 400 nm.

4.1.2 Observation of M-E Induced Second Harmonic Generation

A plot of the measured intensity of the second harmonic radiation as the delay time between the pump and probe beam was scanned is shown in Fig. 4.2(a). The intensity is comprised of two distinct signals. The first component is a pump-induced signal which appears when the relative

delay time is close to zero and the pump and probe hit the sample simultaneously. It should be noted that the total duration of the pump-induced signal is much greater than either the 100 fs pulse duration of the pump and probe beam or the instrumental response, with a rise time around 0.5 ps and a slightly longer decay time around 0.6 ps. This ruled out the possibility that free charges generated by weak two-photon absorption could be producing a charge separation field with a quadratic dependence on pump power which would be similar to the expected behavior from an M-E rectification field. However in this case, the signal rise time would be as fast as the pulse duration, contrary to the observed rise time of about 0.5 ps. The decay time of pump-induced second harmonic generation would then be either that of the singlet exciton lifetime (24 ns) [59; 60] or the singlet fission time scale (80 fs) [61]. Since the signal decay time in Fig. 4.2 was about 0.6 ps, it is clearly quite different from either of these possibilities.

The second component is a static background intensity which does not change in magnitude as the delay time is scanned. The magnitude of this static background is much higher than that of the pump-induced signal. The intensity of the background signal is plotted with respect to the probe power in Fig. 4.2(b). The quadratic fit to the data is shown by the black dashed line. Because the background signal is well fitted by a quadratic curve, it is caused by a quadratic nonlinear process, consistent with second harmonic generation. Although the sample possessed inversion symmetry as detailed in Section 4.1, the surface of the thin film could support surface second harmonic generation by the probe beam alone. This mechanism qualitatively matches the observed behavior in Fig. 4.2 where the intensity of the background remained constant as the relative timing of the pump and probe beam were varied.

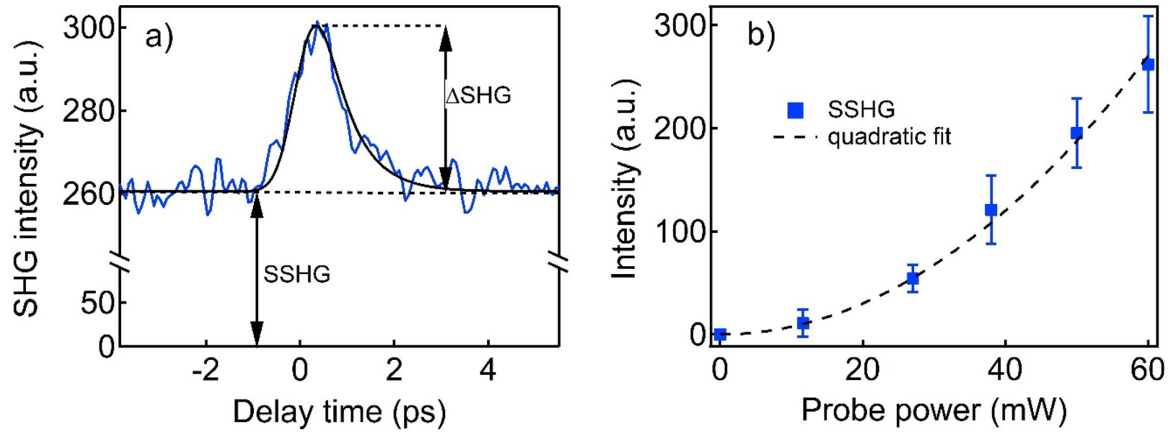


Figure 4.2: (a) Intensity of second harmonic radiation versus delay time between pump and probe beams. There are two distinct components: the static background SSHG and the pump-induced signal Δ SHG. The black curve shows a convolution of the simulated M-E rectification field using the classical model and the instrumental response. (b) Intensity of the static background versus probe beam power.

However, it was possible to quantitatively determine that the source of the static background signal was surface second harmonic generation (SSHG). As discussed in Section 3.1.5, changes in the second harmonic radiation signal changes as the probe polarization was varied could be used to distinguish all-electric second harmonic generation at the surface of the sample from M-E SHG. To that end, the magnitude of the second harmonic radiation signal was measured as the probe polarization angle was rotated from 0° to 180° . The magnitude of the pump-induced signal versus delay time is shown in Fig. 4.3(a) for three different values of the probe polarization. The peak intensity of the second harmonic signal decreases as the probe polarization is rotated from 90° to 0° . The static second harmonic signal (not shown) shows a similar decrease. The peak value of the pump-induced signal and the static signal are plotted versus the probe polarization angle in Fig. 4.3(b). The dashed lines show $\sin^2(\alpha)$ and $\sin^4(\alpha)$ fits to the data for the pump-induced and static signals, respectively. These fitting functions that were derived in Section 3.1.5 are in excellent agreement with the experimental data. Thus, the static background observed in Fig. 4.2(a) is entirely caused by surface second harmonic generation. The $\sin^2(\alpha)$ dependence pump-induced signal, in contrast, shows that it is directly proportional to the M-E rectification field as detailed in Section 3.1.5.

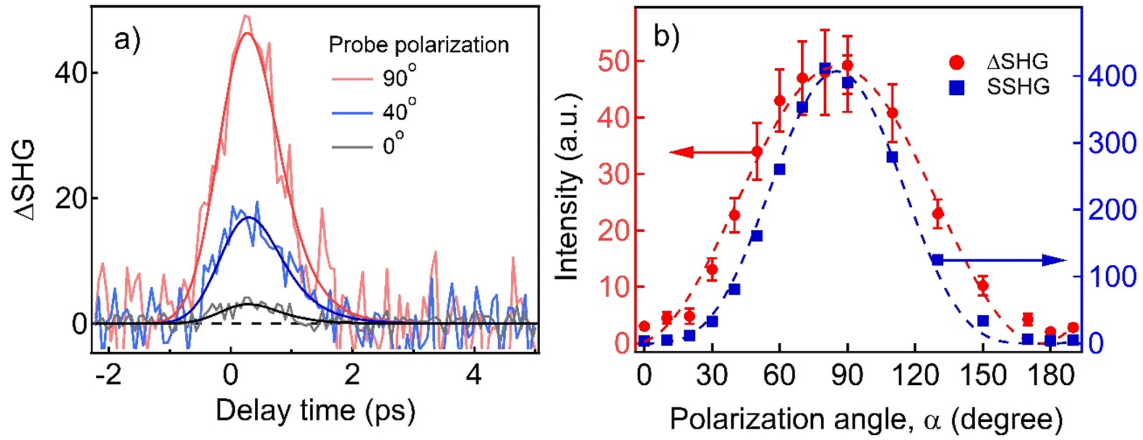


Figure 4.3: Dependence of the second harmonic radiation on probe polarization. (a) Intensity of second harmonic radiation versus delay time for different probe polarization angles. The angles for the red, blue, and black curves were $\alpha = 90^\circ$, $\alpha = 40^\circ$, and $\alpha = 0^\circ$. (b) Peak second harmonic radiation intensity versus the probe polarization angle α . The red and blue data points show the peak experimental signal for the pump-induced signal and the static background respectively. The red and blue dashed lines show a $\sin^2(\alpha)$ fit to the pump-induced signal and a $\sin^4(\alpha)$ fit to the background signal.

The characteristics of the pump-induced second harmonic signal were further investigated by measuring the dependence of the signal on the power and polarization of the pump beam. The peak intensity of the pump-induced signal is plotted versus pump power in Fig. 4.4(a). The dashed line shows a quadratic fit to the data which agrees with the experimental data. The quadratic power dependence ruled out the possibility that the signal was caused by electron-hole pair generation. Even if electron-hole pairs were excited as the result of absorption at 800 nm and resulted in a charge separation field, the field strength would exhibit a linear dependence on pump power. Additionally, the quadratic power dependence ruled out any other all-electric quadratic nonlinearities such as pump-induced rectification. The polarization dependence is plotted in Fig. 4.4(b). The magnitude of the pump-induced signal does not change as the pump polarization is varied. The observed (lack of) polarization angle dependence was in excellent agreement with the prediction for a magneto-electric rectification field, and also served to rule out other all-electric processes. Signals arising from hyper-Rayleigh scattering or pump-induced surface second harmonic generation would have a strong dependence on the pump polarization angle.

In theory, quadrupolar electric interactions could theoretically give rise to second order nonlinear response that could explain the presence of a pump-induced rectification signal. However this is not possible as quadrupole interactions can lead to frequency-doubling but not to rectification.

Consider an x -polarized pump field

$$E_x = E_{x0} (e^{i(\omega t - kz)} + e^{-i(\omega t - kz)}) \quad (4.1)$$

A second order polarization that points along the pump propagation axis and results from a quadrupole interaction [62] then has the form

$$P_z^{(q)} = \epsilon_0 \chi_{zxzx}^{(q)} E_x \frac{\partial}{\partial z} E_x \quad (4.2)$$

In an isotropic material the tensor susceptibility element $\chi_{zxzx}^{(q)}$ does not vanish. However, upon substitution of the pump field, the nonlinear polarization is found to be

$$P_z^{(q)} = \epsilon_0 \chi_{zxzx}^{(q)} (E_{x0} (e^{i(\omega t - kz)} + c.c.)) (-ik E_{x0} e^{i(\omega t - kz)} + c.c.) \quad (4.3)$$

$$P_z^{(q)} = \epsilon_0 \chi_{zxzx}^{(q)} (-ik E_{x0}^2 e^{2i(\omega t - kz)} + ik E_{x0}^2 e^{-2i(\omega t - kz)}) \quad (4.4)$$

This nonlinear polarization consists exclusively of second harmonic terms as the static field terms vanish. Hence the quadrupole interaction does not support rectification. Moreover harmonic radiation from this interaction yields no second harmonic generation signal from the probe alone because the polarization cannot radiate along the propagation axis of the probe, the direction in which the detector is located. While quadrupolar second harmonic generation from the pump alone could reach the detector directly, it would not give rise to a pump-induced change in the second harmonic signal from the probe. Therefore quadrupole interactions cannot account for observed pump-induced signal.

The results of the induced second harmonic generation experiment are thus uniquely consistent with M-E rectification. Analysis of the probe polarization dependence shows that the pump-induced signal originates in the bulk of the material. The dynamic symmetry breaking that occurs in the bulk of the material is shown to be a polarization-insensitive quadratic process. A pump-induced magneto-electric rectification field is the only effect consistent with the observed results that could induce dynamic symmetry breaking in the bulk of the sample.

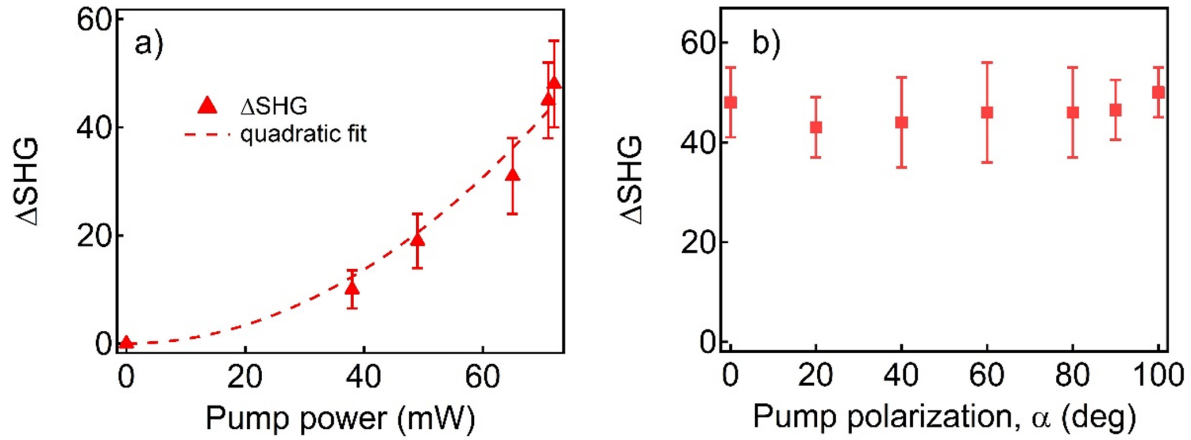


Figure 4.4: Dependence of the second harmonic radiation on the pump beam. The red data points show experimental data. (a) Peak second harmonic radiation intensity versus pump power. The red dashed line shows a quadratic fit to the data. (b) Peak second harmonic radiation versus pump polarization angle.

4.2 Time Dependence from the Coupled Oscillator Simulations

The numerical implementation of the coupled oscillator model described in Section 3.3.1 was used to simulate the M-E response of a molecule to an arbitrary optical field. A standard set of input parameters shown in Table 4.1 was chosen. The incident optical field took the form of a Gaussian pulse with

$$E(t) = E_0 e^{2\log(2)\frac{(t-t_0)^2}{\tau_p^2}} \cos(\omega(t-t_0)) \quad (4.5)$$

The induced rectification field is calculated as the product of the electron charge and the total distance from the simulation origin to the current electron position. The temporal duration of the rectification field was found to depend most on the electronic damping rate γ_e and the molecular rotational frequency ω_m . Changes in these parameters also affect the peak magnitude of the M-E rectification field. The largest rectification magnitude was obtained when the driving field was tuned to the electronic resonance frequency ω_0 . The total enhancement due to molecular torque was found to increase as the pulse width of the driving pulse was increased until the torque enhancement was saturated at a finite pulse width. This charge separation is shown with respect to simulation time in Fig 4.5.

Symbol	Value	Parameter
E_0	10^9 V/m	Electric field magnitude
ω	$0.9\omega_0$	Optical Frequency
t_0	0.5 ps	Zero delay time
τ_p	100 fs	Pulse width
ω_0	$1.63 \cdot 10^{16} \text{ rad/s}$	Electronic resonance frequency
γ_e	$0.25\omega_0$	Electronic damping constant
ω_m	$5 \cdot 10^{-3}\omega_0$	Molecular resonance frequency
γ_m	$0.4\omega_m$	Molecular damping constant
I_{\perp}/I_{\parallel}	1000	Ratio of moments of inertia
\vec{r}_0	{0,15 pm, 0}	Coupling vector

Table 4.1: Standard input parameters for the coupled oscillator model.

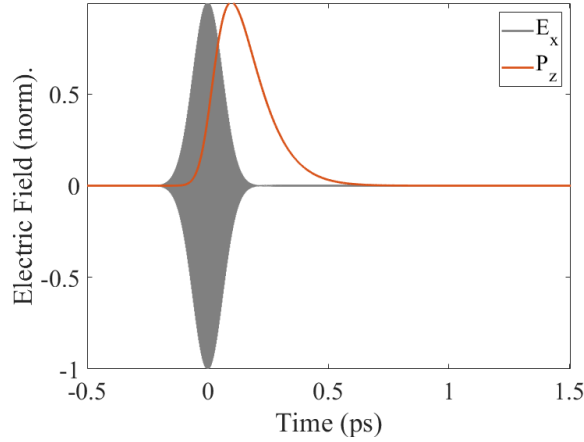


Figure 4.5: Evolution of charge separation (red curve) versus time in the coupled oscillator model when driven by a 100 fs excitation pulse (gray curve). Each curve was individually normalized. All parameters were set to the values specified in Table 4.1.

The incident electric field is shown in gray and is centered around the zero-delay time. Simulation time is adjusted so that the zero-delay time is at $t = 0$. The timescale for development of fully-enhanced rectification and magnetization moments is neither instantaneous nor exactly coincident with the excitation pulse. When illuminated by a Gaussian pulse, there is a delay of 100 fs between the peak electric field of the excitation pulse and the peak value of the magneto-electric rectification moment. Moreover, the rectification moment persists after the excitation pulse, decaying completely only after 500 fs. The delay and asymmetry of this response are indicative of the underlying torque dynamics. It takes time for the driving field to generate enough molecular torque and electron drift for the rectification moment to become fully developed. Similarly, the rectification field does not fall off on the same timescale as the driving pulse, as the intra-molecular

dynamics take time to return to equilibrium.

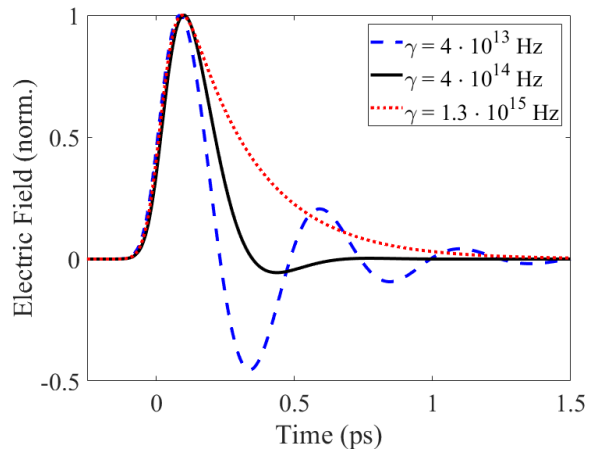


Figure 4.6: Coupled oscillator model simulations of charge separation versus time for different values of the electronic damping rate γ_e . Rates for the blue (dashed), black (solid), and red (dotted) curves were $\gamma = 0.015\omega_0$, $\gamma = 0.15\omega_0$, and $\gamma = 0.5\omega_0$ respectively. All parameters except γ_e were set to the values specified in Table 4.1. Each curve was individually normalized.

Having established the behavior of the model for the standard set of parameters, the parameter space of the model was explored by varying one of the input parameters and observing how the simulation results changed. The first input parameter investigated in this way was the electronic damping rate γ_e . The simulation output is plotted versus time in Fig. 4.6 for rising values of γ_e . Changing the electronic damping rate significantly changes the decay behavior of the charge separation field. While the decay time for the base case is about 500 fs, both the low and high damping cases show extended dynamics where the rectification moment persists for 1 ps after the arrival of the excitation pulse. What differs in the low and high damping cases is the oscillatory behavior. For low damping, multiple overshoots of the equilibrium position take place. For high damping, there are no overshoots. The system simply returns to equilibrium monotonically. These responses exemplify underdamped and overdamped dynamics respectively.

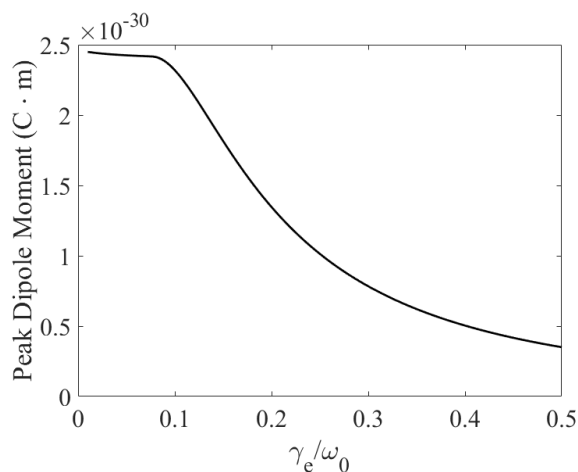


Figure 4.7: Peak magnitude of the rectification moment versus the electronic damping rate γ_e . All parameters except γ_e were set to the values specified in Table 4.1.

Fig. 4.7 shows the peak value of the rectification moment as γ_e is varied. In addition to the change in duration of the charge separation, there is also a clear decrease in the peak magnitude of the rectification moment as γ_e increases. The decrease is slow for values of γ_e below $0.1\omega_0$, but further increases in γ_e result in a steep decrease in the peak rectification moment.

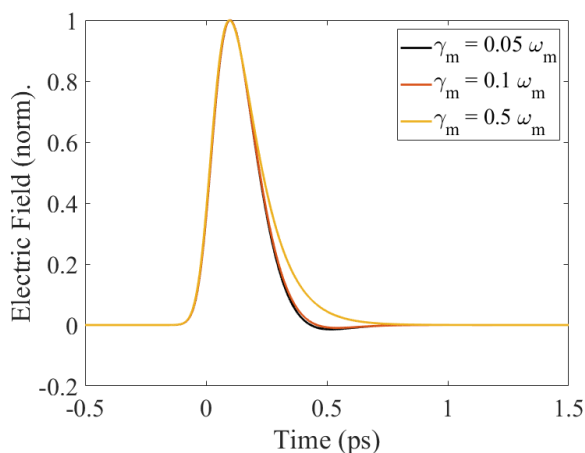


Figure 4.8: Coupled oscillator model simulations of the charge separation field versus time for different values of rotational damping rate γ_m . Frequencies for the black, red, and yellow curves were $\gamma_m = 0.05\omega_m$, $\gamma_m = 0.1\omega_m$, and $\gamma_m = 0.5\omega_m$, respectively. All parameters except γ_m were set to the values specified in Table 4.1. Each curve was individually normalized.

Next, the molecular damping rate γ_m was varied. The simulated rectification field is plotted in Fig. 4.8 versus simulation time. Changes in the molecular damping rate do not have a significant effect on the simulation output. Large values of the molecular damping rate do slightly increase the

rise time, but not to the same extent as seen for changes in the electronic damping rate. It should be noted that the electron exerts a damping force on molecular motion proportional to γ_e due to the coupling between the electronic and molecular oscillators. Because $\gamma_e \gg \gamma_m$, this electronic damping force dominates the molecular dynamics. This coupling behavior is described further in Section 4.4.

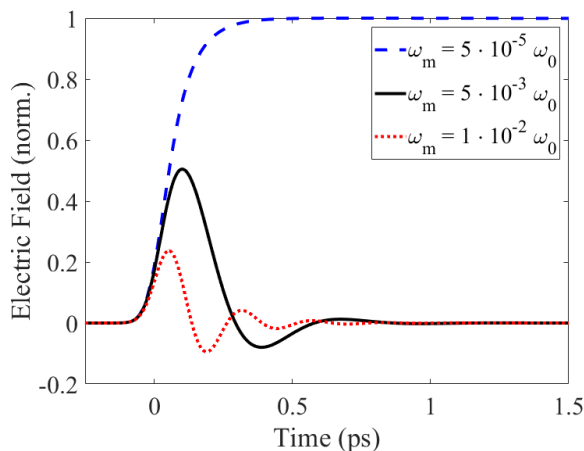


Figure 4.9: Coupled oscillator model simulations of the charge separation field versus time for different values of rotation frequency ω_m . Frequencies for the blue (dashed), black (solid), and red (dotted) curves were $\omega_m = 5 \cdot 10^{-5} \omega_0$, $\omega_m = 5 \cdot 10^{-3} \omega_0$, and $\omega_m = 1 \cdot 10^{-2} \omega_0$, respectively. All parameters except ω_m were set to the values specified in Table 4.1. Each curve was normalized to the dashed blue curve

Changes in the molecular rotation frequency ω_m were also investigated. Fig. 4.9 shows the simulated rectification field plotted versus time for different values of the ω_m . Changes in ω_m have similar effects of the rectification dynamics as changes in γ_e . Reducing the value of ω_m causes a dramatically extended timescale as shown in the dashed blue curve. Additionally, the rise time is longer and the peak rectification is reached about 400 fs after the peak of the driving field. Increasing ω_m from the base case does not significantly change the total duration of the rectification transient. However, increasing ω_m does cause more overshooting to occur during the decay period. The peak magnitude of the field also changes, as increasing the value of ω_m decreases the peak magnitude of the rectification transient.

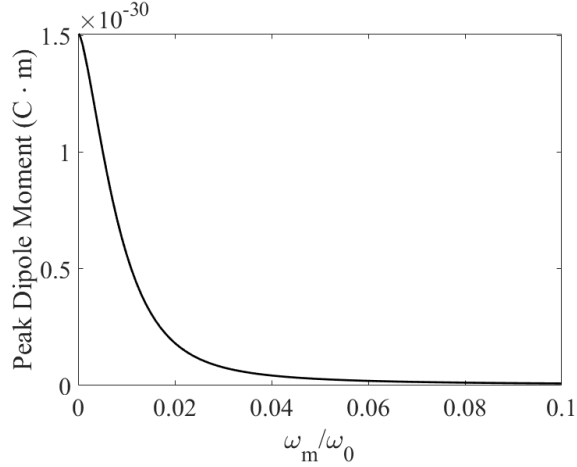


Figure 4.10: Peak value of the rectification moment versus molecular rotational frequency. All parameters except ω_m were set to the values specified in Table 4.1.

The dependence of the peak rectification magnitude on ω_m is shown explicitly in Fig. 4.10. For low values of ω_m the peak rectification field is at its maximum. This peak value quickly decreases as the molecular rotational frequency increases. This decrease is caused by the increase of the restoring force in the torsional oscillator proportional to ω_m^2 . The relaxation behavior of the magneto-electric rectification moment thus depends strongly on both molecular and electronic properties.

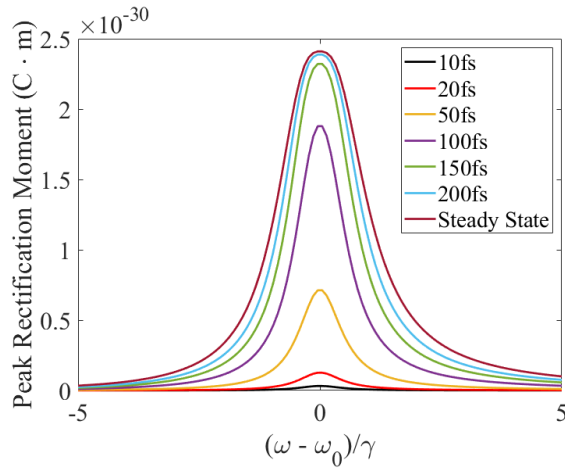


Figure 4.11: Magnitude of the rectification dipole moment versus detuning for different values of τ_p . The steady-state response is also shown for comparison. All parameters except τ_p and ω were set to the values specified in Table 4.1.

Because M-E nonlinearities involve molecular dynamics with long reponse and decay times, ultrashort pulses may not drive the system long enough to saturate the M-E response. For extremely

short pulses, the peak rectification moment is limited by pulse duration. A compelling demonstration of the ultrafast torque dynamics are required for the M-E rectification field to become fully enhanced can be made by tracking development of the rectification dipole moment versus pulse duration. A plot of the peak rectification moment versus optical frequency is shown in Fig. 4.11 for different values of the pulse duration. The steady state response curve is shown as well to illustrate the saturated response. For pulse durations between 10 fs and 200 fs, the M-E response grows steadily with τ_p until it saturates for pulses longer than a well-defined "torque completion time" $\tau_c = \frac{2\pi\hbar}{\mu E}$ [48]. For the coupled oscillator simulation with the parameters set as specified in Table 4.1, this saturation occurs at a pulse duration $\tau_p \approx 250$ fs. The torque completion time calculated from the peak on-resonance steady state value of $2.4 \cdot 10^{-30}$ (C · m) and the parameters in Table 4.1 is $\tau_c = 276$ fs which is in excellent agreement with the saturating pulse duration of 250 fs.

4.3 Time Dependence from the Density Matrix Simulations

The numerical implementation of the density matrix model described in Section 3.3.2 was used to simulate the M-E response of a molecule to an arbitrary optical field. A standard set of input parameters shown in Table 4.2 was chosen. The incident optical field took the form of a Gaussian pulse with

$$V(t) = -\frac{\hbar\Omega}{2} e^{-2\log(2)\frac{(t-t_0)^2}{\tau_p^2}} e^{i\omega(t-t_0)} \quad (4.6)$$

The induced rectification field was calculated as the trace of the density matrix with the magneto-electric transition moment as laid out in Chapter 2. The temporal duration of the rectification field was found to depend most on the molecular properties of the three level system. In the model described in Chapter 2, these were the magneto-electric decoherence rate Γ_{13} and the molecular rotational frequency ω_{13} . The electronic decoherence rate Γ_{12} had no effect on the timescale of the generated M-E polarization, but did affect the peak magnitude of the rectification field. The magnitude of rectification was also found to be affected by Γ_{13} , but ω_{13} had no significant impact on the peak rectification moment. As was found in simulations with the coupled oscillator model, the largest rectification magnitude was obtained when the driving field was tuned to the electronic resonance frequency ω_{12} . The rise time of the rectification moment was found to be approximately equal to the width of the driving pulse. This rectification moment is shown with respect to simulation time in Fig 4.12.

Symbol	Value	Parameter
Ω	$4.235 \cdot 10^{13}$ rad/s	Rabi Frequency
ω	$0.9\omega_0$	Optical Frequency
t_0	1 ps	Zero delay time
τ_p	100 fs	Pulse width
ω_{12}	$1.63 \cdot 10^{16}$ rad/s	Electronic resonance frequency
Γ_{12}	$0.25\omega_0$	Electronic decoherence rate
ω_{13}	$10^{-7}\omega_0$	Molecular resonance frequency
Γ_{13}	10^{12} rad/s	M-E decoherence rate

Table 4.2: Standard input parameters for the density matrix model.

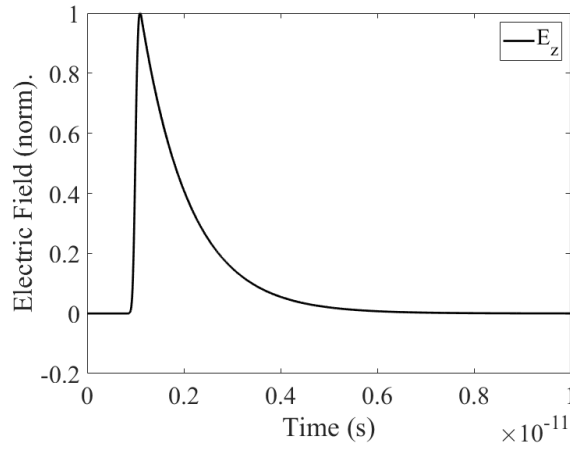


Figure 4.12: Evolution of charge separation versus time in the density matrix model when driven by a 100 fs excitation pulse. All parameters were set to the values specified in Table 4.2.

The timescale of the rectification transient predicted by the density matrix simulation is significantly longer than the timescale of the 100 fs driving pulse. The induced rectification moment exhibits significant asymmetry between the rise time and the decay time. The initial development of the rectification moment takes about 100 fs, similar to the pulse duration of the incident optical field. The decay period is 4 ps. This asymmetry is caused by the transfer of energy from $|1\rangle \leftrightarrow |2\rangle$ coherence to the $|1\rangle \leftrightarrow |3\rangle$ coherence. The decay period of the $|1\rangle \leftrightarrow |3\rangle$ coherence is determined by molecular dynamics which are much slower than the electron dynamics that determine the properties of the $|1\rangle \leftrightarrow |2\rangle$ coherence.

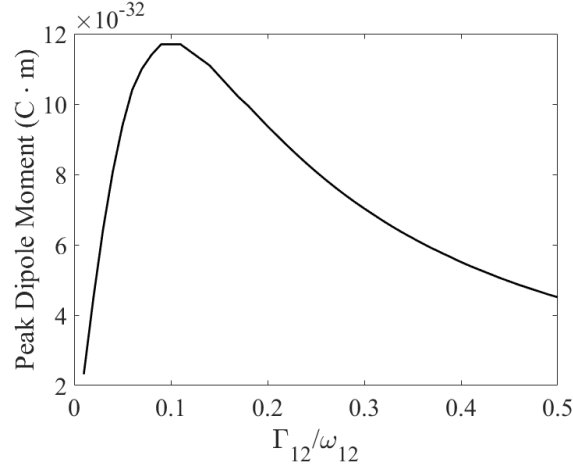


Figure 4.13: Peak magnitude of charge separation versus the decoherence rate Γ_{12} in the density matrix model. All parameters other than Γ_{12} were set to the values specified in Table 4.2.

The first parameter sweep for the quantum model was over the electronic decoherence rate Γ_{12} . The timescale of the rectification transient does not change as Γ_{12} is varied. Fig. 4.13 shows the peak rectification moment plotted versus the decoherence rate as a fraction of the resonance frequency ω_{12} . For small values of the decoherence the peak rectification is low. Because the frequency of the driving field is $\omega = 0.1\omega_{12}$, the peak rectification magnitude is maximized for $\Gamma_{12} = 0.1\omega_{12}$ and the driving frequency falls within the linewidth of the $|1\rangle \leftrightarrow |2\rangle$ transition. Beyond $\Gamma_{12} = 0.1\omega_{12}$, the peak rectification moment decreases gradually as the decoherence increases. Large values of the decoherence cause the $|1\rangle \leftrightarrow |2\rangle$ coherence to decay before the magnitude field can transfer energy to the $|1\rangle \leftrightarrow |3\rangle$ transition via molecular torque.

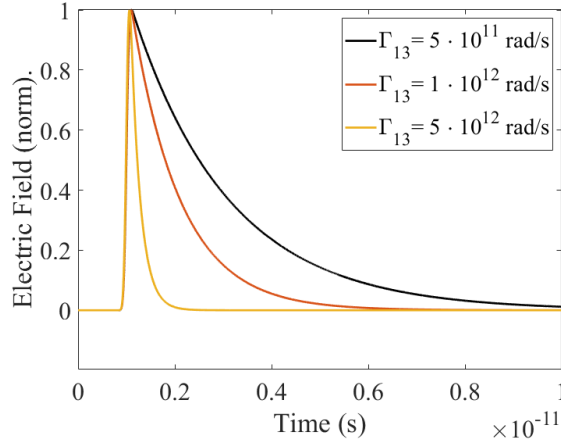


Figure 4.14: Evolution of charge separation versus time in the density matrix model for different values of the decoherence rate Γ_{13} . Decoherence rates for the black, red, and yellow curves were $\Gamma_{13} = 5 \cdot 10^{11}$ rad/s, $\Gamma_{13} = 1 \cdot 10^{12}$ rad/s, and $\Gamma_{13} = 5 \cdot 10^{12}$ rad/s respectively. All parameters other than Γ_{13} were set to the values specified in Table 4.2. Each curve was individually normalized.

Next, the relationship between the rectification moment and the magnetic decoherence rate Γ_{13} was examined. The peak magnitude of the rectification does not change significantly as the Γ_{13} is varied. Fig. 4.14 shows the temporal development of the rectification field for different values of Γ_{13} . The rise time of the rectification moment does not change as Γ_{13} is varied. However, the decay time is significantly affected by changes in the magnetic decoherence rate. The total duration of the rectification field for low values of Γ_{13} can be as long as 9 ps, as shown in the black curve. Increasing Γ_{13} decreases the total duration of the rectification moment, reaching as short as 1 ps as shown in the yellow curve. This matches the predicted analytic behavior as the density matrix element ρ_{13} should decay exponentially as shown in Eqn. 2.88.

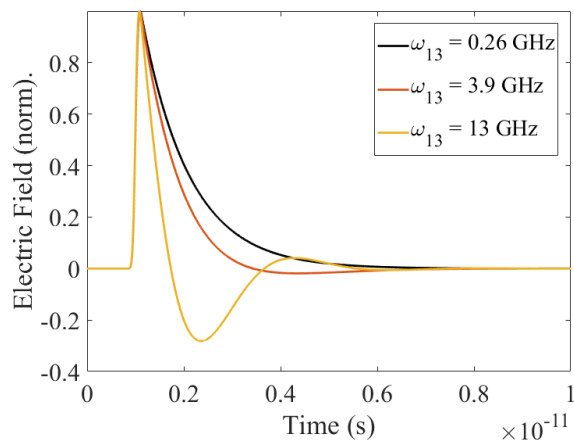


Figure 4.15: Evolution of charge separation versus time in the density matrix model for different values of the rotational frequency ω_{13} . Decoherence rates for the black, red, and yellow curves were $\omega_{13} = 0.26$ GHz, $\omega_{13} = 3.9$ GHz, and $\omega_{13} = 13$ GHz respectively. All parameters other than ω_{13} were set to the values specified in Table 4.2. Each curve was individually normalized.

Fig. 4.15 shows the dependence of the rectification moment on the value of the rotational frequency ω_{13} . Changes in ω_{13} do not significantly change the peak magnitude of the rectification transient. The total duration of the rectification moment increases slightly as ω_{13} is increased from the value of $10^{-7}\omega_0$ from Table 4.2, but otherwise is largely unchanged. This again matches the expected decay behavior predicted from Eqn. 2.88. However, decreasing ω_{13} causes a transition from monotonic decay to an oscillatory decay pattern where rectification field begins to overshoot. Molecular properties have a significant impact on the timescale of the rectification transient.

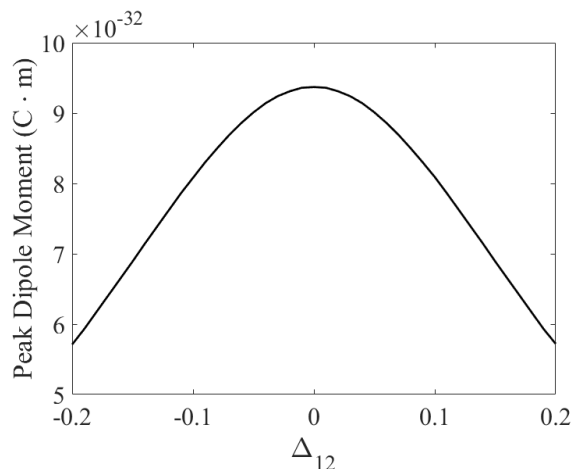


Figure 4.16: Peak magnitude of charge separation versus the detuning Δ_{12}/ω_{12} . All parameters other than ω were set to the values specified in Table 4.2.

The resonance behavior of the rectification moment predicted by the density matrix simulation is shown in Fig. 4.16. Changes in the detuning were implemented by varying the frequency of the incident optical field and fixing the frequency of the electric transition ω_{12} . The peak dipole moment was reached exactly on resonance when $\omega = \omega_{12}$, and the peak value decreases symmetrically as the optical frequency is detuned in either direction from the electronic transition.

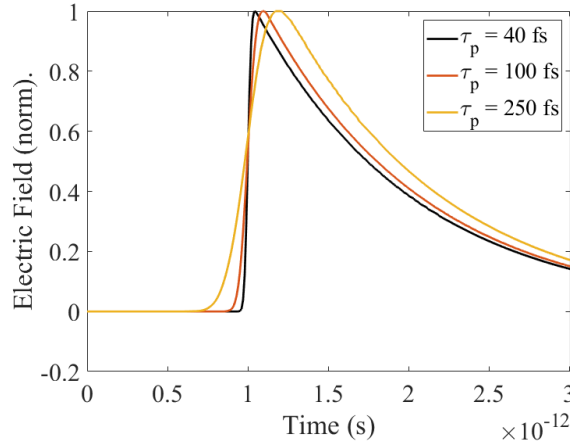


Figure 4.17: Evolution of charge separation versus time in the density matrix model for different pulse widths τ_p . The pulse widths for the black, red, and yellow curves were $\tau_p = 40$ fs, $\tau_p = 100$ fs, and $\tau_p = 250$ fs respectively. All parameters other than τ_p were set to the values specified in Table 4.2. Each curve was individually normalized.

Finally, the dependence of the rectification field on the incident pulse duration is examined in Fig. 4.17. The pulse width was varied from 40 fs to 250 fs, with the base case shown by the red curve. In all cases, the field strength and the position of the zero-delay time were fixed to the values specified in Table 4.2. For the 40 fs pulse, the rise time of the field matches the pulse duration of the driving pulse. The time at which the rectification begins to increase is also right around the zero-delay time. For the base case of 100 fs, the rise time is increased relative to the 40 fs case. The rectification moment begins to increase before the zero-delay time and reaches its maximum about 100 fs after the zero-delay time. These trends continue for the 250 fs case, with the total rise time of about 0.5 ps. The rectification moment begins to develop about 250 fs before the zero-delay point, and the peak rectification value is reached about 250 fs after the zero-delay point.

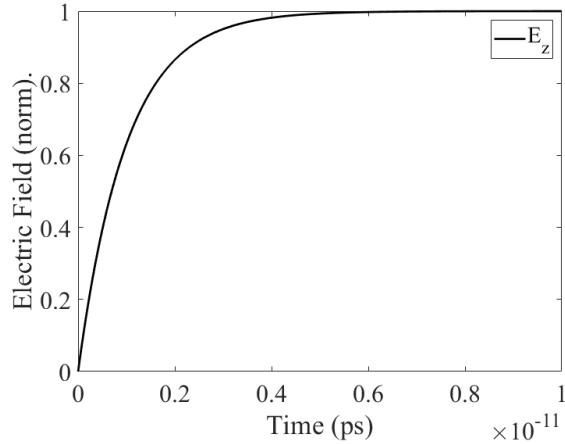


Figure 4.18: Evolution of charge separation versus time in the density matrix model for steady state excitation. All parameters were set to the values specified in Table 4.2. The driving field was assumed to be $V(t) = -\frac{\hbar\Omega}{2}e^{i\omega(t-t_0)}$.

The development of the rectification field in response to steady state excitation is shown in Fig. 4.18. Up until about 1 ps, the rectification field increases quickly and nearly linearly with respect to time. After 1 ps, the rate of increase slows. The magnitude of the rectification field reaches 90% of its peak value at around 2.5 ps, and slowly approaches its steady state peak. This produces a ”torque completion time” of about 4 ps.

4.4 Comparison of Simulation Results

The results described above offer insight into how the M-E rectification nonlinearity develops and what material properties affect the magnitude and duration of the rectification signal. The results of the coupled oscillator and density matrix simulations are largely consistent with one another and show that the M-E rectification moment depends strongly on both the electronic and molecular properties of the material under study. While the parameters of the coupled oscillator model and density matrix model are not directly equivalent, some of the parameters have analogues that are present in both models. These parameters are shown in Table 4.3. Where possible, the values of these analogous parameters were chosen to be equivalent to one another so a direct comparison between the models was possible. The timescale and duration of the simulated results from both the coupled oscillator model and the density matrix model are consistent with the experimentally measured rectification moment.

Changes in the electronic damping rate present a slightly more complex picture. While increasing or decreasing the value of Γ_{12} in the density matrix model has little effect on the temporal characteristics of the M-E rectification field, changes in γ_e in the coupled oscillator model have a

Coupled Oscillator Parameter	Density Matrix Parameter	Notes
Ω	E_0	Strength of the incident optical field
ω_0	ω_{12}	Electronic transition frequency
Γ_{12}	γ_e	Damping/decoherence rate for the electric transition
ω_{13}	ω_m	Molecular resonance frequency
Γ_{13}	γ_m	Molecular damping/decoherence rate

Table 4.3: Analogous parameters between the coupled oscillator and density matrix models.

substantial effect on the decay behavior of the rectification field. This difference in response between the models is due to the method by which the electronic and torsional oscillators are coupled in the coupled oscillator model and is discussed further later in this section. Varying the electronic damping rate in both models does result in changes to the peak magnitude of the M-E rectification field. The changes in the peak rectification as γ_e and Γ_{12} are varied are shown in Figs. 4.7 and 4.13. In both models, there is a steep monotonic decrease in the peak rectification magnitude once the damping rate is increased above $0.1\omega_0$. This decrease is caused by decay of electronic motion before it can be converted by the magnetic field into molecular motion. One difference between the coupled oscillator model and the density matrix model can be seen for values of the damping rate below $0.1\omega_0$. The coupled oscillator model predicts little to no change in the peak rectification magnitude as γ_e is varied below that value, while the density matrix model predicts a peak at $\Gamma_{12} = 0.1\omega_{12}$ with an even sharper decrease in the rectification field as Γ_{12} decreases below $0.1\omega_{12}$. The difference between the model results for this region is caused by linewidth effects. Decreases in Γ_{12} cause the linewidth of the $|1\rangle \leftrightarrow |2\rangle$ transition to decrease. Because the base case uses a driving frequency $\omega = 0.9\omega_{12}$, the detuning falls within the linewidth of $0.1\omega_{12}$. If the linewidth is decreased and the detuning held constant, the detuning will begin to fall below the linewidth and there will be a decreased driving efficiency of the $|1\rangle \leftrightarrow |2\rangle$ coherence. Because this is a quantum effect, the classical model has no mechanism which can capture this behavior.

The molecular damping has little effect on the peak rectification magnitude but does have a significant effect on the timescale of the rectification moment. The most appropriate comparison of the molecular damping is actually between the electronic damping rate γ_e in the coupled oscillator model and the M-E decoherence rate Γ_{13} in the density matrix model. This is due to the method by which the two models are coupled. The electron drives molecular motion by exerting a force on

its restoring position, which manifests as a torque on the molecular system. When the electron is being driven by the incident optical field, this torque drives molecular motion which enhances the rectification field as described in Section 2.1. After the driving field passes through the system, the molecular oscillator begins to return to its original position due to the restoring force proportional to ω_m^2 . Because the electron is coupled to its restoring point, it too returns to its original position in the simulation at a non-zero velocity. This non-zero velocity means that the electron motion is dissipating energy at a rate proportional to $\gamma_e \vec{v}_e$. The rate of energy dissipation due to the electron velocity is much greater than the rate of dissipation due to molecular motion which is proportional to $\gamma_m \dot{\theta}_m$ because $\gamma_e \gg \gamma_m$. The electron damping rate γ_e thus acts as the effective damping rate of the molecular motion instead of γ_m . For this reason, changing γ_e in the coupled oscillator model is most directly comparable to changing Γ_{13} in the density matrix model in terms of evaluating the effect of changing the damping rate on the temporal properties of the M-E rectification field.

A comparison between Figs. 4.6 and 4.14 appears to show an inconsistency in how the two models respond to a change in the molecular damping. Increasing γ_e in the coupled oscillator model increases the decay period of the rectification moment but increasing Γ_{13} in the density matrix model decreases the decay period. This apparent contradiction is due to the different structure of the differential equations in each model and is discussed in further detail in Appendix D. If the damping rate in the coupled oscillator model is kept below the critical damping rate, both models are in agreement that increasing the molecular damping rate decreases the duration of the rectification nonlinearity. Because these parameters are not equivalent, the timescale of the base cases for the coupled oscillator and density matrix models cannot be directly compared. The two models agree best on the temporal duration of rectification when the value of the Γ_{13} in the density matrix model is increased from $1 \cdot 10^{12}$ rad/s to $7 \cdot 10^{12}$ rad/s. The rectification field predicted by the two models when this change is made are overlaid on one another in Fig. 4.19.

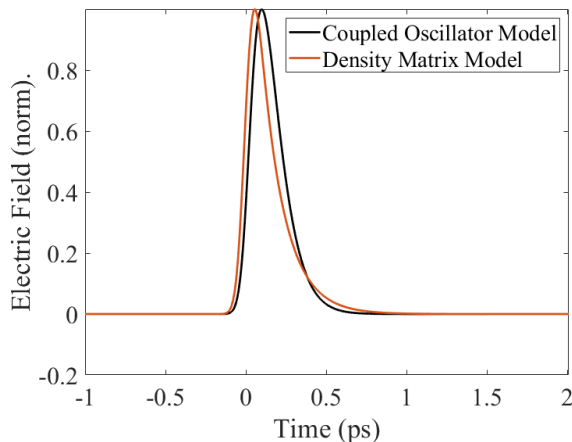


Figure 4.19: Comparison between the coupled oscillator and density matrix model predicts for the rectification field. All parameters were set to the values specified in Tables 4.1 and 4.2 except for $\Gamma_{13} = 7 \cdot 10^{12}$ rad/s.

In a related way, the molecular rotational frequency cannot be directly compared in the coupled oscillator and density matrix models. As laid out in Appendix D, the structure of the differential equations in each model is responsible for the difference in how the rectification field responds to changes in the molecular rotational frequency. The coupling between the rotational frequency ω_m and the molecular damping γ_m in the coupled oscillator model is responsible for the behavior seen in Fig. 4.10. Increasing the molecular rotational frequency also increases the effective damping rate of the molecular model. However, both of the models agree on the qualitative change in the decay behavior as seen in Figs. 4.9 and 4.15. Increasing the rotational frequency increases the number and magnitude of the overshoots as the rectification field decays.

In both models, the magnitude of the M-E rectification moment is enhanced when driven exactly on the electronic transition frequency. This is consistent with the theoretical predictions from Section 2.3. The frequency response of the coupled oscillator and density matrix models around the electronic resonance is shown in Figs. 4.11 and 4.16 respectively. Due to limited computational resources, the density matrix simulation was only able to be carried out for a detuning $\Delta_{12} = \pm 2\Gamma_{12}$. However, both models predict a similar Lorentzian lineshape. M-E rectification can be induced in a material even if the optical field is off resonance. This is further borne out in the experimental results, as rectification is observed even though the pentacene thin film is excited below the bandgap. Although a nonzero torque completion time can be observed in the output from both models as shown in Figs. 4.11 and 4.18, the torque completion time is significantly different. The coupled oscillator model predicts a torque completion time of around 250 fs, while the density matrix model predicts a value of 4 ps. This discrepancy can be reduced by adjusted the parameters of the density matrix model so the timescale of the rectification decay more closely matches the

coupled oscillator model as seen in Fig. 4.19. The development of the rectification field in response to steady state excitation is shown in Fig. 4.20 for the modified value of $\Gamma_{13} = 7 \cdot 10^{12}$ rad/s.

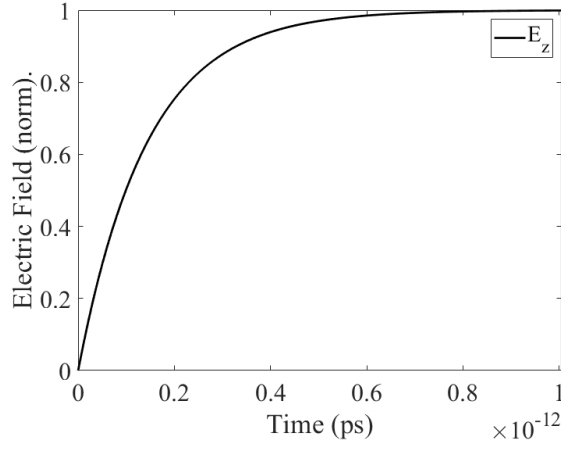


Figure 4.20: Evolution of charge separation versus time in the density matrix model for steady state excitation. All parameters were set to the values specified in Table 4.2 except for $\Gamma_{13} = 7 \cdot 10^{12}$ rad/s. The driving field was assumed to be $V(t) = -\frac{\hbar\Omega}{2}e^{i\omega(t-t_0)}$.

The torque completion time is reduced to 700 fs. While this is much lower than the value predicted by the base case of the density matrix model, it is still longer than the value predicted by the coupled oscillator model. Further increasing Γ_{13} can reduce this torque completion time to values closer to those predicted by the coupled oscillator model, but the temporal duration of the rectification nonlinearity would be further reduced beyond the predictions of the classical model.

CHAPTER 5

Conclusion

In this chapter, a summary of the results and future direction of research into M-E nonlinearities is presented. Experimental and computational results are summarized in Section 5.1. The first experimental measurement of M-E rectification was made by detecting M-E induced second harmonic generation in a pentacene thin film. The characteristics of the measured rectification field agree with the theoretical predictions made in Chapter 2 as well as the simulation results from Sections 4.2 and 4.3. The results from the two computational models, one classical and the other quantum mechanical, illustrate how the electronic and molecular properties of a material affect the development of the rectification field. Both models are capable of simulating the M-E response in a material under experimental conditions, and thus can be used to predict the M-E response of molecular materials. A discussion of future areas of research into M-E nonlinearities is presented in Section 5.2 along with potential applications of the findings of this thesis. The M-E rectification field could be used in areas such as ultrafast all-optical switching, energy conversion, and terahertz generation. The results of this thesis show the existence and properties of the M-E rectification nonlinearity and what molecular properties are optimal for these applications. The computational models presented in this thesis can be used to find the optimal material properties for these and other potential applications.

5.1 Summary of Results

An experiment was carried out to measure the second harmonic radiation induced by the M-E rectification effect in a pentacene thin film sample. Due to the unique geometry of M-E nonlinearities, the experiment used a crossed-beam pump probe geometry. This design allowed the rectification field to develop in the same plane as the probe polarization, so the electric field of the probe could interact with the M-E rectification field. The crossed-beam experimental geometry retained the ultrafast temporal resolution characteristic of co-propagating pump-probe geometries through the use of pulse-front tilt. A 45° pulse front tilt was applied on both the pump and probe pulse to

achieve a temporal resolution equal to the pulse duration.

The pentacene thin film sample was chosen because its structure made it effectively centrosymmetric on the scale of the laser wavelength. Individual crystallites in the sample were oriented in a specific direction, but the size of these crystallites is 100 to 200 nm, four to eight times smaller than the 800 nm wavelength of the laser. The crystallites had a random orientation relative to one another, so the sample possessed inversion symmetry on the scale of the laser wavelength. The effective symmetry of the sample meant that all-electric rectification or second harmonic generation were not supported. Thus, the only possible second order effects that could contribute to a second harmonic radiation signal would be surface second harmonic generation or M-E induced second harmonic generation.

The detected second harmonic radiation signal showed a clear pump-induced transient along with a static background field. The background signal showed a quadratic dependence on probe power, which was clearly indicative of second harmonic generation from the probe beam. The pump-induced signal has a slightly asymmetric shape, with a shorter rise time than decay time. This asymmetry agrees with both the classical and quantum theories of M-E rectification.

To distinguish the source of second harmonic radiation, the magnitude of the second harmonic signal was measured as a function of the probe polarization. It was found that the pump-induced transient had a $\sin^2(\alpha)$ dependence on the probe polarization while the static background signal had a $\sin^4(\alpha)$ dependence. A analysis of the geometry of the probe-sample interaction showed that the $\sin^4(\alpha)$ background signal was caused by surface second harmonic generation, while the pump-induced transient with the $\sin^2(\alpha)$ dependence was consistent with a signal arising from dynamic symmetry breaking in the bulk of the sample. The only source of this dynamic symmetry breaking could be a pump-induced polarization moment.

To determine the nature of the pump-induced asymmetry, the dependence of the magnitude of the transient second harmonic radiation signal on the pump beam properties were measured. The pump-induced transient was shown to have no dependence on the pump polarization, and it possessed a quadratic dependence on the pump power. The quadratic power dependence indicated that a second order process was responsible for the induced asymmetry. Because all-electric second order processes could be ruled out by the sample symmetry, the pump induced transient must be caused in part by the optical magnetic field. Further evidence for the role of the optical magnetic field is provided by the pump-polarization dependence of the transient signal. An all-electric process should exhibit a dependence on the pump polarization as the direction of the electric field of the pump would change the orientation of the generated polarization moment. This change in orientation would subsequently change the amount of detected second harmonic radiation. Taken together, the measured dependence of the transient field on the pump beam show direct evidence of the involvement of the optical magnetic field in the rectification dynamics.

The results of the induced second harmonic generation experiment are thus uniquely consistent with a M-E rectification process that induces a quasi-static polarization moment in the sample. Surface second harmonic generation is responsible for the static background signal, but the pump-induced signal is shown to originate in the bulk of the material. The only mechanism that would permit bulk second harmonic generation would be pump-induced symmetry breaking, consistent with the P-T symmetry of magneto-electric interactions [63]. This dynamic symmetry breaking is shown to be a polarization-insensitive quadratic process, so it cannot be caused by an all-electric effect. Thus a pump-induced magneto-electric rectification field must be the cause of the induced second harmonic generation. Additionally, the temporal characteristics of the experimentally measured M-E rectification moment were found to agree with the predictions of the computational models and ruled out the possibility that excited electron dynamics could be responsible for the observed pump-induced signal. The work in this thesis therefore provides for the first time an unambiguous experimental observation of the M-E rectification field.

In addition to the experimental results, two computational models were used to investigate the properties of M-E rectification. The first computational model is based on a coupled oscillator theory of M-E interactions. The electron response to a driving optical field is modelled using a classical electron oscillator model of an atom. The optical magnetic field in the electron oscillator model couples energy from motion parallel to the optical electric field to longitudinal motion. This energy transfer exhibits a parametric resonance which seeds M-E nonlinearities. Molecular motion is modelled by a rigid rotor model in which the angular motion of a molecular is tracked by a torsional oscillator. The two models are coupled by fixing the restoring point of the electron oscillator to a point on the surface of the rigid rotor model. The force between the electron and its restoring point exerts torque on the molecule and thereby allows the electron to drive molecular motion. This coupling represents the transfer of orbital angular momentum to rotational angular momentum in the molecule. The M-E nonlinearities that were seeded by parametric resonance are enhanced by this exchange of angular momentum. The combined effect of these two enhancement mechanisms significantly reduces the intensity threshold of magnetic effects by several orders of magnitude.

The second computational model is based on a density matrix model of M-E interactions. A model three level system of a molecule is presented in which rotational coupling between the ground and excited states allows for a magnetic dipole transition to exist at approximately the same energy level as the electric dipole transition. The optical electric field excites the electric dipole transition, adding energy and angular momentum to the molecular system. The magnetic field then exchanges orbital angular momentum and rotational angular momentum, completing the M-E transition and returning the molecular to near its ground state energy. The dynamics of the three level system are analyzed using the density matrix. Perturbation theory is used to calcu-

late the density matrix elements. Because the electric and magnetic transitions occur in different quadratures, the M-E polarization is obtained by taking the projection of the trace of the M-E coherence along the direction of optical propagation.

For the first time, computational simulations of M-E nonlinearities were carried out under pulsed excitation conditions. The properties of the rectification moment predicted by these time-dependent simulations was shown to depend strongly on both electronic and molecular properties of the system under study. Both the classical coupled oscillator model as well as the quantum density matrix model were used to simulate the M-E response to a incident optical field. The temporal characteristics of the rectification moment were influenced most strongly by variations in the molecular properties including the molecular damping or decoherence rate and the frequency of molecular rotation. High values of the molecular damping rate cause rapid decay of the M-E polarization moment and reduce the temporal duration of the rectification field. Changes in the molecular rotational frequency have a similar effect, as large values of ω_m cause ringing and overshooting as the molecule coherently rotates within the decay period. These two parameters do also have a effect on the peak magnitude of M-E rectification. A faster decay of the rectification period will limit the buildup of energy and reduce the maximum amplitude of the polarization moment. Also, because the value of ω_m is directly equal to the two-photon detuning, changes in ω_m can slightly affect the resonance conditions. However this effect is small because the energy scale of the electronic transition is much larger than the energy of molecular rotations. The largest impact on the peak rectification magnitude is caused by the electron damping or decoherence rate. Because the magnetic field needs to act after the electric field, any decrease in the magnitude of the electronic interaction will also affect the amount of energy transferred to the M-E polarization moment. The peak rectification field was also found to be strongest when the driving field was in resonance with the electronic transition, confirming that M-E interactions offer a pathway to strong magnetic effects on electronic transitions. Increasing the duration of the driving pulse was also found to increase the peak magnitude of the rectification field up until the "torque completion time" beyond which the magnetic response is saturated. Differences in simulation trends between the coupled oscillator and density matrix models were attributed to the different forms of the differential equations underlying each model.

5.2 Future Work

In this dissertation, the first experimental observation of M-E was accomplished and two computational models of M-E rectification were developed. Future work can further characterize the M-E rectification field and verify the validity of the two models. In particular, implementing the birefringence experiment described in Section 3.2 would provide a more sensitive measurement of

the M-E rectification field that could also directly measure the magnitude of the field. The magnitude of the rectification field could then be compared to results from the computational models for materials for which the electronic and molecular properties used in the simulations are known. Additional work can focus on applying the understanding of the properties of the rectification field to photonic applications. The unique geometry of M-E nonlinearities offer the potential for ultrafast all-optical switching at right angles, as well as for novel methods of terahertz generation. The charge separation effect could also be used for new methods of energy conversion where optical energy is converted to electrical energy.

5.2.1 Ultrafast Photonic Switching at Right Angles

The induced birefringence experiment outlined in Section 3.2 offers a proof of concept for the potential use of the M-E rectification field for ultrafast photonic switching at right angles. The results presented in this thesis confirm that the rectification field has a rise time similar to the pulse duration of the optical pulse that drives M-E rectification. The experimentally observed sub-picosecond rise times are significantly faster than the timescale that can be achieved with electronic switching, while the computational results show that the duration of the induced refractive index change can be adjusted to some extent by the choice of the interaction medium. Theoretical calculations of the M-E susceptibility have shown that the tensor element responsible for the M-E rectification field is equal to the off-diagonal Kerr tensor element [64]. Thus an M-E photonic switch should have similar power requirements and switching efficiency as an all-optical Kerr switch with the added benefit of being able to switch at right angles. Full polarization rotation may be difficult or inefficient to achieve using M-E induced refractive index changes. However, the switching efficiency of such a device could be greatly enhanced by integrating the interaction medium in a photonic crystal structure near the sharp edge of a stop band [65]. Kerr switching has previously been demonstrated to work efficiently at low powers [66; 67]. Then the M-E induced increase in refractive index could modify the properties of the stop band and either enable or disable transmission with high efficiency.

5.2.2 Terahertz Generation

Another future avenue of research into the M-E rectification field is its use in terahertz generation. The potential for the use of M-E rectification in terahertz generation has been investigated before [46]. The computational work described in this thesis can be used to accurately model the M-E response to an ultrafast optical pulse. The simulated rectification field can then be analyzed to determine the spectral properties of a potential M-E generated terahertz pulse. Preliminary simulation results from the coupled oscillator model are shown in Fig. 5.1. The magnitude of

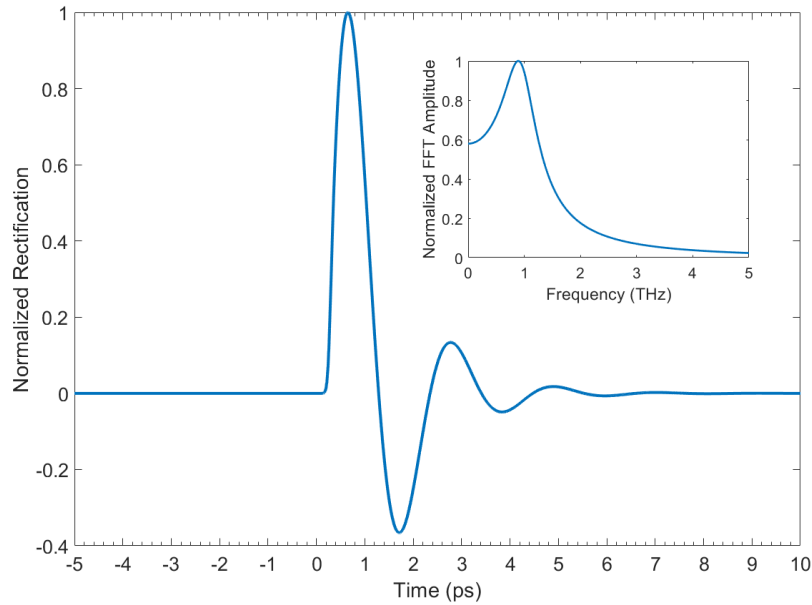


Figure 5.1: Simulated rectification moment from coupled oscillator model. Inset: Frequency composition of the rectification signal obtained via a Fast Fourier Transform.

the simulated rectification moment is shown versus time, while the inset shows the frequency composition of the signal as obtained through a Fast Fourier Transform (FFT) of the rectification signal. The FFT shows that the simulated pulse has a large frequency component around 1 THz which gradually falls off as the frequency approaches 5 THz. Using a different target material with different material properties would alter the THz spectrum and could be tailored to find the desired properties. Additional tuning could be achieved by changing the pulse front tilt of the incident laser source [68]. Because the M-E rectification effect can occur in all dielectric materials, the use of M-E rectification for terahertz generation could open up new classes of interaction materials for terahertz generation.

5.2.3 Energy Conversion in Insulators

One intriguing potential use of the M-E rectification field is for energy conversion. This possibility has been previously investigated by Fisher [46]. Unlike rectification that occurs parallel to the optical electric field, M-E rectification is longitudinal. Thus the relevant length scale across which charge separation occurs is not the diameter of the beam, but rather the distance travelled by the beam through the interaction medium. Because the magnitude of the induced rectification field is the same at all points along the interaction medium, the total voltage across the medium will be proportional to the length of the medium. Focusing a laser into a long fiber could extend

this interaction length and produce large voltages between either end of the fiber. This energy conversion approach would likely be limited by material considerations. The damage threshold of the conversion medium would need to exceed the strength of the induced rectification field. M-E rectification is greatly enhanced when the incident field is tuned close to an electronic resonance, so the highest energy conversion possible would occur for an intense monochromatic continuous-wave source tuned close to resonance. Thus M-E rectification could be used to beam power across long distances using a CW laser source.

APPENDIX A

Calculation of M-E Induced Birefringence

To derive the expected birefringence signal arising from M-E rectification, a complete mathematical treatment of the pump-induced birefringence that includes all possible nonlinear effects must be developed. Because the probe beam is polarized in the xz plane, the total index of refraction only needs to be calculated along these two directions. The total birefringence is the difference of the index of refraction along the x and z directions.

The pump beam is assumed to be arbitrarily polarized in the xy plane while the probe beam is polarized at 45° from the z axis in the xz plane. Mathematically, this means

$$\vec{E}_{pump} = E_x(\omega)\hat{x} + E_y(\omega)\hat{y} \quad (\text{A.1})$$

$$\vec{E}_{probe} = \frac{E_{probe}(\omega)}{\sqrt{2}}\hat{x} + \frac{E_{probe}(\omega)}{\sqrt{2}}\hat{z} \quad (\text{A.2})$$

The probe beam is assumed to be weak enough that nonlinear polarization moments that are generated only from the beam can be neglected. Because the sample is assumed to be isotropic, second order all-electric effects such as the electro-optic effect are not supported. Thus the only nonlinear pump-induced effects that must be included are the M-E rectification moment and all possible Kerr terms. The form of the nonlinear polarization induced by M-E rectification is given in the Supplementary Information of Ref. [64].

$$P_{ME}^{(3)}(\omega) = \epsilon_0 \left\{ \frac{[\chi_{zyx}^{(eme)}(0; -\omega, \omega)]^2}{\epsilon_r(0) - 1} \right\} E_0^*(-\omega) E_0(\omega) E_z(\omega) \hat{z} \quad (\text{A.3})$$

where $\chi_{zyx}^{(eme)}$ is the second order magneto-electric susceptibility, $E_0(\omega)$ is the total pump field $E_0 = \sqrt{E_x^2 + E_y^2}$, and $E_z(\omega)$ is the z component of the probe field. For simplicity, the term in brackets will be defined such that $\left\{ \frac{[\chi_{zyx}^{(eme)}(0; -\omega, \omega)]^2}{\epsilon_r(0) - 1} \right\} = \chi_{ME}$. The Kerr terms are generally

$$P_i(\omega) = \epsilon_0 \chi_{ijkl}^{(3)} E_j(\omega) E_k^*(-\omega) E_l(\omega) \quad (\text{A.4})$$

where χ_{ijkl} is the third order susceptibility tensor. Because the sample is isotropic and is non-resonantly excited, the only nonzero elements of this tensor are χ_{iiii} and $\chi_{iiij} = \chi_{ijji} = \chi_{ijij}$. The total polarization along x is then

$$P_x(\omega) = \epsilon_0 \chi_{xx}^{(1)} \frac{E_{probe}(\omega)}{\sqrt{2}} + \epsilon_0 \chi_{xxxx}^{(3)} E_x(\omega) E_x^*(-\omega) \frac{E_{probe}(\omega)}{\sqrt{2}} + \epsilon_0 \chi_{xyyx}^{(3)} E_y(\omega) E_y^*(-\omega) \frac{E_{probe}(\omega)}{\sqrt{2}} \quad (\text{A.5})$$

while the polarization along z is

$$P_z(\omega) = \epsilon_0 \chi_{zz}^{(1)} \frac{E_{probe}(\omega)}{\sqrt{2}} + \epsilon_0 \chi_{zxxz}^{(3)} E_x(\omega) E_x^*(-\omega) \frac{E_{probe}(\omega)}{\sqrt{2}} + \epsilon_0 \chi_{zyyz}^{(3)} E_y(\omega) E_y^*(-\omega) \frac{E_{probe}(\omega)}{\sqrt{2}} + \epsilon_0 \chi_{ME} E_0(\omega) E_0^*(-\omega) \frac{E_{probe}(\omega)}{\sqrt{2}} \quad (\text{A.6})$$

The common factor of $\epsilon_0 \frac{E_{probe}(\omega)}{\sqrt{2}}$ can be factored out to obtain

$$P_x(\omega) = \epsilon_0 \frac{E_{probe}(\omega)}{\sqrt{2}} (\chi_{xx}^{(1)} + \chi_{xxxx}^{(3)} E_x(\omega) E_x^*(-\omega) + \chi_{xyyx}^{(3)} E_y(\omega) E_y^*(-\omega)) \quad (\text{A.7})$$

$$P_z(\omega) = \epsilon_0 \frac{E_{probe}(\omega)}{\sqrt{2}} (\chi_{zz}^{(1)} + \chi_{zxxz}^{(3)} E_x(\omega) E_x^*(-\omega) + \chi_{zyyz}^{(3)} E_y(\omega) E_y^*(-\omega) + \chi_{ME} E_0(\omega) E_0^*(-\omega)) \quad (\text{A.8})$$

The terms inside the parentheses can be treated as an effective susceptibility.

$$\chi_{x,eff} = \chi_{xx}^{(1)} + \chi_{xxxx}^{(3)} E_x(\omega) E_x^*(-\omega) + \chi_{xyyx}^{(3)} E_y(\omega) E_y^*(-\omega) \quad (\text{A.9})$$

$$\chi_{z,eff} = \chi_{zz}^{(1)} + \chi_{zxxz}^{(3)} E_x(\omega) E_x^*(-\omega) + \chi_{zyyz}^{(3)} E_y(\omega) E_y^*(-\omega) + \chi_{ME} E_0(\omega) E_0^*(-\omega) \quad (\text{A.10})$$

Assuming weak magnetization i.e. $\mu = \mu_0$, the refractive indices along x and z seen by the component of the probe pulse polarized in those directions is given by the square root of these effective susceptibilities. If the nonlinear contributions to the effectively susceptibility are small compared to the linear susceptibility, the small argument approximation can be taken. This gives the following expressions for the indices of refraction

$$n_x \approx n_0 + \frac{1}{2n_0} (\chi_{xxxx}^{(3)} E_x(\omega) E_x^*(-\omega) + \chi_{xyyx}^{(3)} E_y(\omega) E_y^*(-\omega)) \quad (\text{A.11})$$

$$n_z \approx n_0 + \frac{1}{2n_0} (\chi_{zxxz}^{(3)} E_x(\omega) E_x^*(-\omega) + \chi_{zyyz}^{(3)} E_y(\omega) E_y^*(-\omega) + \chi_{ME} E_0(\omega) E_0^*(-\omega)) \quad (\text{A.12})$$

where the unperturbed index $n_0 = \sqrt{1 + \chi_{xx}} = \sqrt{1 + \chi_{zz}}$. The total birefringence Δn is then the difference $n_x - n_z$

$$\Delta n = \frac{1}{2n_0} \left((\chi_{xxxx}^{(3)} - \chi_{zxxx}^{(3)}) E_x(\omega) E_x^*(-\omega) - \chi_{ME} E_0(\omega) E_0^*(-\omega) \right) \quad (\text{A.13})$$

The Kerr contributions induced by E_y cancel, so the only Kerr contribution to the birefringence is caused by E_x . If the pump polarization is set along the y axis, only the M-E term will contribute to the birefringence because it has no dependence on the pump polarization.

$$\Delta n = -\frac{1}{2n_0} \chi_{ME} E_0(\omega) E_0^*(-\omega) \quad (\text{A.14})$$

Additionally, the sign of the birefringence due to the M-E term is negative, while the Kerr contribution is positive.

APPENDIX B

Coupled Oscillator Model

B.1 Main Program

```
% ME_ClassicalTheory_v1_RealVals_NoDim
% Elizabeth Dreyer
% 2017-07-10
% Magneto-Electric Scattering Experiment
% Purpose: Simulate the classical equations for the
% Magneto-electric scattering

% Edited 2019-03-1 by Greg Smail
% Changed filename
% Added parameter sweep capability
% Rearranged input files

plots = 0;

%% ODE Set-up
% ODE solver parameters
abserr = 1.0e-22;
relerr = 1.0e-20;
stoptime = 10e-12;
numpoints = 5e4;
t = linspace(0, stoptime, numpoints);

scanpoints = 1;
```

```

% Load in molecular values, default parameters,
$ and initial conditions
Arbitrary_Molecular_Values_TRS_FEF;
Default_Parameters_TRS_FEF;
Initial_Conditions_TRS_FEF;

% Parameter Scans
lightIntv = linspace(1e9,1e9,scanpoints);
Ev = linspace(1e9,1e9,scanpoints);
tauPv = linspace(1e-14,25e-14,scanpoints);
gv = linspace(0.08*w0,0.8*w0,scanpoints);
gmolv = linspace(0.05*wm,0.5*wm,scanpoints);
w0v = linspace(.5*w0,5.0*w0,scanpoints);
wmv = linspace(1e-3*w0,1e-1*w0,scanpoints);
wv = linspace(w0-5*g,w0+5*g,scanpoints);
iPerv = linspace(1,200,scanpoints);

% Create arrays to store solution at all points
x1s_scan = zeros([scanpoints,numpoints]);
y1s_scan = zeros([scanpoints,numpoints]);
z1s_scan = zeros([scanpoints,numpoints]);
x2s_scan = zeros([scanpoints,numpoints]);
y2s_scan = zeros([scanpoints,numpoints]);
z2s_scan = zeros([scanpoints,numpoints]);
oxs_scan = zeros([scanpoints,numpoints]);
oys_scan = zeros([scanpoints,numpoints]);
ozs_scan = zeros([scanpoints,numpoints]);
xds_scan = zeros([scanpoints,numpoints]);
yds_scan = zeros([scanpoints,numpoints]);
zds_scan = zeros([scanpoints,numpoints]);
txs_scan = zeros([scanpoints,numpoints]);
tys_scan = zeros([scanpoints,numpoints]);
tzs_scan = zeros([scanpoints,numpoints]);

m2x_scan = zeros([scanpoints,numpoints]);
m2y_scan = zeros([scanpoints,numpoints]);

```

```

m2z_scan = zeros([scanpoints,numpoints]);
m2xC_scan = zeros([scanpoints,numpoints]);
m2yC_scan = zeros([scanpoints,numpoints]);
m2zC_scan = zeros([scanpoints,numpoints]);
p0x_scan = zeros([scanpoints,numpoints]);
p0y_scan = zeros([scanpoints,numpoints]);
p0z_scan = zeros([scanpoints,numpoints]);
m2xt_scan = zeros([scanpoints,numpoints]);
m2yt_scan = zeros([scanpoints,numpoints]);
m2zt_scan = zeros([scanpoints,numpoints]);
p0xt_scan = zeros([scanpoints,numpoints]);
p0yt_scan = zeros([scanpoints,numpoints]);
p0zt_scan = zeros([scanpoints,numpoints]);
pf_scan = zeros([scanpoints,numpoints]);
Ex_scan = zeros([1,scanpoints]);
pulse_energy = zeros(1,scanpoints);

% Choose value over which to perform parameter sweep
plotv = wv;
xname = 'Frequency';
xunits = 'Hz';
xaxis = strcat(xname,xunits);
for counter = 1:scanpoints
disp(counter)
%Ex_scan(counter) = Ev(counter); %Electric field strength
%lightInt = lightIntv(counter);
%epulse = epulsev(counter);
%tauP = tauPv(counter);
%g = gv(counter);
%wm = wmv(counter);
%gmol = gmolv(counter);
w = wv(counter);
%w0 = w0v(counter);
%iPar = iParv(counter);
%iPer = iPerv(counter)*iPar;

```

```

Ex = Ex_scan(counter);

% Pack up the parameters and initial conditions:
p = [w0, w, g, c, e, m, iPar, iPer,
     Ex, kz, freq, tauP, gmol, wm, rb];
s0 = [x1, y1, z1, x2, y2, z2, ox, oy,
     oz, xd, yd, zd, tx, ty,tz];

syms s

%% Run ODE 23s
options = odeset('RelTol',relerr,'AbsTol',abserr);
wsol = ode23(@ (t,s)
            mes_ODE_WithDim_func_GS_TRS_centered(t,s,p),t,s0);
reg_sol = deval(t,wsol);
%% Define Solutions
% Assign solution to separate arrays
tSol = t;
x1s_scan(counter,:) = reg_sol(1,:);
y1s_scan(counter,:) = reg_sol(2,:);
z1s_scan(counter,:) = reg_sol(3,:);
x2s_scan(counter,:) = reg_sol(4,:);
y2s_scan(counter,:) = reg_sol(5,:);
z2s_scan(counter,:) = reg_sol(6,:);
oxs_scan(counter,:) = reg_sol(7,:);
oys_scan(counter,:) = reg_sol(8,:);
ozs_scan(counter,:) = reg_sol(9,:);
xds_scan(counter,:) = reg_sol(10,:);
yds_scan(counter,:) = reg_sol(11,:);
zds_scan(counter,:) = reg_sol(12,:);
txs_scan(counter,:) = reg_sol(13,:);
tys_scan(counter,:) = reg_sol(14,:);
tzs_scan(counter,:) = reg_sol(15,:);

```

```

% Dimensionalized vectors
m2x_scan(counter,:) =
    e/2 (z1s_scan(counter,:).*yds_scan(counter,:))
    +y1s_scan(counter,:).*zds_scan(counter,:));
m2y_scan(counter,:) =
    e/2*(z1s_scan(counter,:).*xds_scan(counter,:))
    -x1s_scan(counter,:).*zds_scan(counter,:)); %MD
m2z_scan(counter,:) =
    e/2*(-y1s_scan(counter,:).*xds_scan(counter,:))
    +x1s_scan(counter,:).*yds_scan(counter,:));
m2xC_scan(counter,:) =
    e/2*(-z1s_scan(counter,:).*yds_scan(counter,:))
    +y1s_scan(counter,:).*zds_scan(counter,:))/c;
m2yC_scan(counter,:) =
    e/2*(z1s_scan(counter,:).*xds_scan(counter,:))
    -x1s_scan(counter,:).*zds_scan(counter,:))/c; %MD/c
m2zC_scan(counter,:) =
    e/2*(-y1s_scan(counter,:).*xds_scan(counter,:))
    +x1s_scan(counter,:).*yds_scan(counter,:))/c;
p0x_scan(counter,:) = e*x1s_scan(counter,:); %ED
p0y_scan(counter,:) = e*y1s_scan(counter,:);
p0z_scan(counter,:) = e*z1s_scan(counter,:); %Charge Separation

%pf_scan(counter,:) =
    exp(-2*log(2)*(t-2.5*tauP).^2/tauP^2).*cos(w*(t-2.5*tauP));
pf_scan(counter,:) =
    (1./(1+exp(-5e13*(t-2e-13))))
    - 1./(1+exp(-5e13*(t-(2e-13+tauP))))).*sin(w*t);
pulse_energy(counter) =
    eps0/2 * Ex^2 *sum(pf_scan(counter,:).^2);
end
E0_scan = p0z_scan/(eps0) * 6e23/278.36 * 1.3 * 1e6; %Pentacene
%E0_scan = p0z_scan/(eps0) * 6e23/153.82 * 1.59 * 1e6; %CCL4
if plots == 1
    intensity_plot_code;
end

```

B.2 ODE Solver

```
Addifunction[dy] = mes_ODE_WithDim_func_GS_TRS_centered(t,s,p)
% mes_ODE_func
% Elizabeth Dreyer, edited by Greg Smail
% 2019-02-4
% Magneto-Electric Scattering Experiment
% Purpose: System of ODEs for solving
% Input Parameters: t = time, s = functions, p = parameters

%Initialize dy
dy = zeros(12,1);

%Expand s and p in terms of other variables
%pn = [w0n, wn, gn, cn, en, mn, iParn,
      iPern, Exn, kz, freqn, tauPn, t0, q0, me, rb];
%s0n = [x1, y1, z1, x2, y2, z2, ox, oy, oz, xd, yd, zd];
x1 = s(1); y1 = s(2); z1 = s(3);
x2 = s(4); y2 = s(5); z2 = s(6);
ox = s(7); oy = s(8); oz = s(9);
xd = s(10); yd = s(11); zd = s(12);
tx = s(13); ty = s(14); tz = s(15);

w0 = p(1); w = p(2); g = p(3); c = p(4);
e = p(5); m = p(6); iPar = p(7); iPer = p(8);
Ex = p(9); k = p(10); freq = p(11); tauP = p(12);
gmol = p(13); wm = p(14); rb = p(15);

% Define pulse function
%pulseFunc = sin(w*t);
pulseFunc =
    exp(-2*log(2)*((t-1e-12)).^2/tauP^2).*cos(w*((t-1e-12)));

%Write the equations
dy(1,1) = xd;
dy(2,1) = yd;
```

```

dy(3,1) = zd;
dy(4,1) = (z2*oy - y2*oz);
dy(5,1) = (-z2*ox + x2*oz);
dy(6,1) = (y2*ox - x2*oy);
dy(7,1) = m/(iPar) * w0*w0 *(y2*z1-y1*z2)
        - gmol*ox - wm*wm*tx; % azimuthal component
dy(8,1) = m/(iPer) * w0*w0 *(-x2*z1+x1*z2) - gmol*oy - wm*wm*ty;
dy(9,1) = m/(iPer) * w0*w0 *(x2*y1-x1*y2) - gmol*oz - wm*wm*tz;
dy(10,1) = e/m*Ex*pulseFunc-w0*w0*(x1-x2)
        -e*Ex*k/(c*m)*pulseFunc*zd-g*xd;
dy(11,1) = -w0*w0*(y1-y2)-g*yd;
dy(12,1) = -w0*w0*(z1-z2)+e*Ex*k/(c*m)*pulseFunc*xd-g*zd;
dy(13,1) = ox;
dy(14,1) = oy;
dy(15,1) = oz;
end

```

B.3 Input Files

B.3.1 Molecular Values

```

w0 = 2.594e+15;           %Arbitrary Oscillator 1.533e+15 1/s
w0R = w0*2*pi;          %w0 in radians per second
g = 0.25*w0;
wm = w0*1e-3;
gmol = 0.5*wm;
n1 = 1;

```

B.3.2 Simulation Parameters

```

%% Define Intitial Conditions and Parameters for System
% Fundamental Constants
c = 299792458;           %Speed of Light in m/s
e = 1.61e-19;           %Electron charge in C

```

```

m = 9.11e-31;           %Electron mass in kg
eps0 = 8.85e-12;       %Electric permitivity in Vacuum
M = 1.674e-27;         %Mass of Hydrogen in Kg
R = 2*0.0375e-9;       %Bond length of diatomic Hydrogen
rb = 5.292e-11;        % Bohr Radius
hbar = 1.0545718e-34;

```

```
% Default Laser Parameter Values
```

```

var = 1;
freq = 80.0E6;         %Laser Rep Rate
tauP = 100e-15;       %Pulse Duration
lightInt = 1e8;       %Pulse Intensity
Ex = 1e9;
pulse_spot = 20e-6;   %Laser Spot Size
w = 0.9*w0;           %Laser Frequency
kz = 1;

```

```
% Default MOI Parameter Values
```

```

iPar = hbar/w0R;       %Molecular ratio arb
iPer = 1000*iPar;%M/2*R*R;           %Molecular ratio arb

```

B.3.3 Initial Conditions

```
% Initial Conditions
```

```
% x1, y1, z1 are the position of the electron wrt. the foot point
```

```
x1 = 0.0;
```

```
y1 = 15e-12; %15e-12;
```

```
z1 = 0.0;
```

```
% x2, y2, z2 are the initial displacement
```

```
of the footpoint wrt. the COM
```

```
x2 = 0.0;
```

```
y2 = 15e-12;
```

```
z2 = 0.0;
```

```
% ox, oy, oz are the initial angular momentums of the electron
```

```
ox = 0.0;
```

```
oy = 0.0;
```

```
oz = 0.0;
% xd, yd, zd are the initial velocities of the electron
xd = 0.0;
yd = 0.0;
zd = 0.0;
% tx, ty, tz are initial angles away from footpoint at rest
tx = 0.0;
ty = 0.0;
tz = 0.0;
```

APPENDIX C

Density Matrix Model

C.1 Mathematica Code (Output Omitted)

```
vals = {Ω →  $\frac{4235}{1000} * 10^{13}$ , ω →  $\frac{147}{100} * 10^{16}$ , ω12 →  $\frac{163}{100} * 10^{16}$ , τ →  $\frac{10}{10} * 10^{-13}$ , a →  $1 * 10^{-12}$ ,
  Γ12 →  $\frac{25}{100} * \frac{163}{100} * 10^{16}$ , γ2 →  $10^{13}$ , γ3 →  $10^6$ , ω13 →  $20 * 10^{-7} * \frac{163}{100} * 10^{16}$ , Γ13 →  $1 * 10^{12}$ ,
  q →  $-1.6 * 10^{-19}$ , a0 →  $5.29 * 10^{-11}$ };
```

```
q =  $-1.6 * 10^{-19}$ ;
```

```
a0 =  $5.29 * 10^{-11}$ ;
```

```
V[Ω-, ω-, τ-, a-, t-]:= -  $\frac{\hbar * \Omega}{2} e^{-2\text{Log}[2] \left(\frac{t-a}{\tau}\right)^2} e^{i * \omega * t}$ ;
```

```
Vc[Ω-, ω-, τ-, a-, t-]:= -  $\frac{\hbar * \Omega}{2} e^{-2\text{Log}[2] \left(\frac{t-a}{\tau}\right)^2} e^{-i * \omega * t}$ ;
```

```
eqn = {x'[t] == (i * ω12 - Γ12) * x[t] +  $\frac{i}{\hbar} V[\Omega, \omega, \tau, a, t]$ , x[0] == 0};
```

```
sol = DSolve[eqn, x, t];
```

```
specSol = x[t]/.sol;
```

```
ρ12[Γ12-, ω12-, a-, τ-, ω-, Ω-, t-]:= -  $\frac{1}{4} e^{t(-\Gamma12+i\omega12)+\frac{(\Gamma12+i(\omega-\omega12))(\Gamma12\tau^2+i\tau^2(\omega-\omega12)+8a\text{Log}[2])}{\text{Log}[256]}} \tau \Omega$ 
  ( Erfi  $\left[ \frac{i\Gamma12\tau^2+\tau^2(-\omega+\omega12)+4ia\text{Log}[2]}{2\tau\sqrt{\text{Log}[4]}} \right]$  - Erfi  $\left[ \frac{i\Gamma12\tau^2+\tau^2(-\omega+\omega12)-4i(-a+t)\text{Log}[2]}{2\tau\sqrt{\text{Log}[4]}} \right]$  )  $\sqrt{\frac{\pi}{\text{Log}[4]}}$ ;
```

```
Block[{$MaxExtraPrecision = ∞}, ρ13sol = NDSolve [
```

```
  {ρ'[t] == ((i * ω13 - Γ13) * ρ[t] +  $\frac{i}{\hbar} \rho12[\Gamma12, \omega12, a, \tau, \omega, \Omega, t]$  * Vc[Ω, ω, τ, a, t]) /.vals,
```

```
  {ρ[0] == 0}, {ρ, p}, {t, 0,  $10 * 10^{-12}$ }, WorkingPrecision →
```

```
50, Method->“StiffnessSwitching”];
```

```
Plot [ $\frac{128}{243} * q * a0$ (Conjugate[Evaluate[ρ[t]]/.ρ13sol] + Evaluate[ρ[t]]/.ρ13sol), {t, 0,  $5 * 10^{-12}$ },
```

PlotRange→ Full, PlotPoints → 400

Plot [$\frac{128}{243} * q * a0(\text{Conjugate}[\text{Evaluate}[\rho[t]]/.rho13sol] + \text{Evaluate}[\rho[t]]/.rho13sol)$, {t, 0, $10 * 10^{-12}$ },

PlotRange→ Full, PlotPoints → 400

Plot [Re[$\rho12[\Gamma12, \omega12, a, \tau, \omega, \Omega, t]$]/.vals], {t, 0, $10 * 10^{-12}$ },

PlotRange→ Full, PlotPoints → 400

PSweepOutput1 = N [Table [{t, Re [$\frac{128}{243} * q * a0(\text{Conjugate}[\text{Evaluate}[\rho[t]]/.rho13sol] +$

Evaluate[$\rho[t]$]/.rho13sol)/.vals, {t, 0, $10 * 10^{-12}$, 10^{-14} };

PSweepOutput = Transpose[PSweepOutput1/.{x_, {{y_}}}->{x, y}];

Export["filename.csv", PSweepOutput]

APPENDIX D

Effects of the Different Form of Coupled Oscillator and Density Matrix Models

While the results of the two computational models are largely consistent, there are a few scenarios in which the two models exhibit different behavior in response to a change in the simulation parameters. This is most apparent for changes in the damping parameters γ_e and Γ_{12} and changes in the molecular rotational frequencies ω_m and ω_{13} . This difference is due to the different forms of the differential equations used in the two models. The equations of motion for the coupled oscillator model are second order in time, while the density matrix model equations of motion are first order in time. The damping parameter and molecular frequencies thus appear in different forms in the analytic and numerical solutions to these differential equations, which causes the observed differences in the responses of the models to changing input parameters.

The coupled oscillator model has the equations of motion detailed in Eqns. 2.23 - 2.27. For pulsed illumination, the driving electric and magnetic fields on the right hand side of Eqns. 2.23 - 2.27 will go to zero after the pulse passes through. The decay behavior of the electronic part of the coupled oscillator model is thus described by the second order homogeneous differential equation.

$$\ddot{x} + \gamma_e \dot{x} + \omega_0^2 x = 0 \quad (\text{D.1})$$

The general solution in terms of γ_e and ω_0 is then

$$x(t) = Ae^{\frac{-\gamma_e - \sqrt{\gamma_e^2 - 4\omega_0^2}}{2}t} + Be^{\frac{-\gamma_e + \sqrt{\gamma_e^2 - 4\omega_0^2}}{2}t} \quad (\text{D.2})$$

This general solution has two branches corresponding to the two possible signs of $\sqrt{\gamma_e^2 - 4\omega_0^2}$. For the underdamped cases where $\gamma_e^2 < 4\omega_0^2$, this term is entirely imaginary and causes oscillatory decay behavior within a $e^{-\frac{\gamma_e}{2}t}$ envelope. In this case, increasing γ_e increases the rate at which the total solution decays. However in the overdamped case where $\gamma_e^2 > 4\omega_0^2$, the square root takes on a real value. Increasing γ_e in this case decreases the total rate of decay, as the second term in

Eqn. D.2 will decay slower than the $e^{-\frac{\text{gamma}ae}{2}t}$ envelope present in the underdamped case. The equation of motion for the torsional oscillator of the rigid rotor model has a similar solution as it also a second order differential equation.

$$\theta(t) = Ae^{-\frac{\gamma_m - \sqrt{\gamma_m^2 - 4\omega_m^2}}{2}t} + Be^{-\frac{\gamma_m + \sqrt{\gamma_m^2 - 4\omega_m^2}}{2}t} \quad (\text{D.3})$$

It should be noted that the sign of $\gamma_m^2 - 4\omega_m^2$ depends on both γ_m and ω_m , so the transition from underdamped to overdamped behavior can be caused by a change of ω_m .

In contrast, the equation of motion for the coherence ρ_{13} in the density matrix model takes the form of a first order differential equation. The general form of the homogeneous equation that controls the decay behavior is thus

$$\dot{\rho}_{13} + (i\omega_{13} + \Gamma_{13})\rho_{13} = 0 \quad (\text{D.4})$$

This has the simple solution

$$\rho_{13} = Ae^{-i\omega_{13}t - \Gamma_{13}t} \quad (\text{D.5})$$

In this equation, Γ_{13} will only affect the decay rate of the solution, while ω_{13} changes only the frequency of the oscillatory behavior. Notably, the decoherence rate of the electron transition Γ_{12} has no effect on the decay behavior of ρ_{13} .

Because the two models have different forms, they respond differently to changes in the input parameters. The coupling between the damping parameter and the resonance frequency in the coupled oscillator model means that an increase in the damping rate can paradoxically decrease the rate of decay. This also means that changes in the resonance frequency can affect the rate of decay by changing the value of $\sqrt{\gamma^2 - 4\omega^2}$. The density matrix model exhibits no such complications, so increasing or decreasing the damping parameter will result in a corresponding increase or decrease of the rate of decay. Similarly, changes in the resonance frequency will have no effect on the rate of decay.

BIBLIOGRAPHY

- [1] E. F. C. Dreyer, A. A. Fisher, G. Smail, P. Anisimov, and S. C. Rand, “Optical magnetization, part III: theory of molecular magneto-electric rectification,” *Optics Express*, vol. 26, pp. 17755–17771, July 2018.
- [2] M. T. Trinh, G. Smail, K. Makhal, D. S. Yang, J. Kim, and S. C. Rand, “Observation of magneto-electric rectification at non-relativistic intensities,” *Nature Communications*, vol. 11, pp. 1–6, Oct. 2020. Number: 1 Publisher: Nature Publishing Group.
- [3] A. Boltasseva and V. M. Shalaev, “Fabrication of optical negative-index metamaterials: Recent advances and outlook,” *Metamaterials*, vol. 2, no. 1, pp. 1 – 17, 2008.
- [4] V. G. Veselago and E. E. Narimanov, “The left hand of brightness: past, present and future of negative index materials,” *Nature Materials*, vol. 5, pp. 759–762, Oct. 2006.
- [5] B. Cappello, A. K. Ospanova, L. Matekovits, and A. A. Basharin, “Mantle cloaking due to ideal magnetic dipole scattering,” *Scientific Reports*, vol. 10, p. 2413, Dec. 2020.
- [6] J. B. Pendry, “Negative Refraction Makes a Perfect Lens,” *Phys. Rev. Lett.*, vol. 85, pp. 3966–3969, Oct. 2000.
- [7] Z. Liu, H. Lee, Y. Xiong, C. Sun, and X. Zhang, “Far-Field Optical Hyperlens Magnifying Sub-Diffraction-Limited Objects,” *Science*, vol. 315, pp. 1686–1686, Mar. 2007.
- [8] A.-P. Fang, W. Ge, M. Wang, F.-l. Li, and M. S. Zubairy, “Negative refraction without absorption via quantum coherence,” *Physical Review A*, vol. 93, p. 023822, Feb. 2016. Publisher: American Physical Society.
- [9] W. P. Leemans, B. Nagler, A. J. Gonsalves, C. Tóth, K. Nakamura, C. G. R. Geddes, E. Esarey, C. B. Schroeder, and S. M. Hooker, “GeV electron beams from a centimetre-scale accelerator,” *Nature Physics*, vol. 2, pp. 696–699, Oct. 2006.
- [10] A. Gonsalves, K. Nakamura, J. Daniels, C. Benedetti, C. Pieronek, T. de Raadt, S. Steinke, J. Bin, S. Bulanov, J. van Tilborg, C. Geddes, C. Schroeder, C. Tóth, E. Esarey, K. Swanson, L. Fan-Chiang, G. Bagdasarov, N. Bobrova, V. Gasilov, G. Korn, P. Sasorov, and W. Leemans, “Petawatt Laser Guiding and Electron Beam Acceleration to 8 GeV in a Laser-Heated Capillary Discharge Waveguide,” *Physical Review Letters*, vol. 122, p. 084801, Feb. 2019.
- [11] G. A. Mourou, T. Tajima, and S. V. Bulanov, “Optics in the relativistic regime,” *Reviews of Modern Physics*, vol. 78, pp. 309–371, Apr. 2006. Publisher: American Physical Society.

- [12] A. V. Arefiev, V. N. Khudik, A. P. L. Robinson, G. Shvets, L. Willingale, and M. Schollmeier, “Beyond the ponderomotive limit: Direct laser acceleration of relativistic electrons in sub-critical plasmas,” *Physics of Plasmas*, vol. 23, p. 056704, May 2016.
- [13] A. E. Hussein, A. V. Arefiev, T. Batson, H. Chen, R. S. Craxton, A. S. Davies, D. H. Froula, Z. Gong, D. Haberberger, Y. Ma, P. M. Nilson, W. Theobald, T. Wang, K. Weichman, G. J. Williams, and L. Willingale, “Towards the optimisation of direct laser acceleration,” *New Journal of Physics*, vol. 23, p. 023031, Feb. 2021. Publisher: IOP Publishing.
- [14] M. J. Weber and R. F. Schaufele, “Radiative and Nonradiative Transitions in the Fluorescence Decay of Eu^{3+} in SrTiO_3 ,” *The Journal of Chemical Physics*, vol. 43, pp. 1702–1709, May 2004.
- [15] W. T. Carnall, P. R. Fields, and K. Rajnak, “Spectral Intensities of the Trivalent Lanthanides and Actinides in Solution. II. Pm^{3+} , Sm^{3+} , Eu^{3+} , Gd^{3+} , Tb^{3+} , Dy^{3+} , and Ho^{3+} ,” *The Journal of Chemical Physics*, vol. 49, pp. 4412–4423, Sept. 2003.
- [16] M. Kasperczyk, S. Person, D. Ananias, L. D. Carlos, and L. Novotny, “Excitation of Magnetic Dipole Transitions at Optical Frequencies,” *Physical Review Letters*, vol. 114, p. 163903, Apr. 2015. Publisher: American Physical Society.
- [17] N. R. Brewer, Z. N. Buckholtz, Z. J. Simmons, E. A. Mueller, and D. D. Yavuz, “Coherent Magnetic Response at Optical Frequencies Using Atomic Transitions,” *Physical Review X*, vol. 7, p. 011005, Jan. 2017.
- [18] Z. N. Buckholtz and D. D. Yavuz, “Linear and nonlinear crystal optics using the magnetic field of light,” *Physical Review A*, vol. 101, p. 023831, Feb. 2020. Publisher: American Physical Society.
- [19] M. Fiebig, “Revival of the magnetoelectric effect,” *Journal of Physics D: Applied Physics*, vol. 38, p. R123, Apr. 2005.
- [20] C.-W. Nan, “Magnetoelectric effect in composites of piezoelectric and piezomagnetic phases,” *Physical Review B*, vol. 50, pp. 6082–6088, Sept. 1994.
- [21] D. R. Tilley and J. F. Scott, “Frequency dependence of magnetoelectric phenomena in BaMnF_4 ,” *Physical Review B*, vol. 25, pp. 3251–3260, Mar. 1982.
- [22] S. Shastry, G. Srinivasan, M. I. Bichurin, V. M. Petrov, and A. S. Tatarenko, “Microwave magnetoelectric effects in single crystal bilayers of yttrium iron garnet and lead magnesium niobate-lead titanate,” *Physical Review B*, vol. 70, p. 064416, Aug. 2004. Publisher: American Physical Society.
- [23] U. Laletsin, N. Padubnaya, G. Srinivasan, and C. DeVreugd, “Frequency dependence of magnetoelectric interactions in layered structures of ferromagnetic alloys and piezoelectric oxides,” *Applied Physics A*, vol. 78, pp. 33–36, Jan. 2004.

- [24] N. Cai, C.-W. Nan, J. Zhai, and Y. Lin, “Large high-frequency magnetoelectric response in laminated composites of piezoelectric ceramics, rare-earth iron alloys and polymer,” *Applied Physics Letters*, vol. 84, pp. 3516–3518, Apr. 2004.
- [25] N. Cai, J. Zhai, C.-W. Nan, Y. Lin, and Z. Shi, “Dielectric, ferroelectric, magnetic, and magnetoelectric properties of multiferroic laminated composites,” *Physical Review B*, vol. 68, p. 224103, Dec. 2003. Publisher: American Physical Society.
- [26] D. Talbayev, S. A. Trugman, S. Lee, H. T. Yi, S.-W. Cheong, and A. J. Taylor, “Long-wavelength magnetic and magnetoelectric excitations in the ferroelectric antiferromagnet BiFeO₃,” *Physical Review B*, vol. 83, p. 094403, Mar. 2011.
- [27] D. R. Smith, J. B. Pendry, and M. C. K. Wiltshire, “Metamaterials and Negative Refractive Index,” *Science*, vol. 305, pp. 788–792, Aug. 2004. Publisher: American Association for the Advancement of Science.
- [28] J. B. Pendry, A. J. Holden, D. J. Robbins, and W. J. Stewart, “Magnetism from conductors and enhanced nonlinear phenomena,” *IEEE Transactions on Microwave Theory and Techniques*, vol. 47, pp. 2075–2084, Nov. 1999.
- [29] V. G. Veselago, “THE ELECTRODYNAMICS OF SUBSTANCES WITH SIMULTANEOUSLY NEGATIVE VALUES OF ϵ AND μ ,” *Soviet Physics Uspekhi*, vol. 10, no. 4, p. 509, 1968.
- [30] K. Becharef, K. Nouri, H. Kandouci, B. S. Bouazza, M. Damou, and T. H. C. Bouazza, “Design and Simulation of a Broadband Bandpass Filter Based on Complementary Split Ring Resonator Circular “CSRRs”,” *Wireless Personal Communications*, vol. 111, pp. 1341–1354, Apr. 2020.
- [31] A. I. Kuznetsov, A. E. Miroshnichenko, Y. H. Fu, J. Zhang, and B. Luk’yanchuk, “Magnetic light,” *Scientific Reports*, vol. 2, p. 492, Dec. 2012.
- [32] J. B. Pendry, D. Schurig, and D. R. Smith, “Controlling Electromagnetic Fields,” *Science*, vol. 312, pp. 1780–1782, June 2006. Publisher: American Association for the Advancement of Science.
- [33] U. Leonhardt, “Optical Conformal Mapping,” *Science*, vol. 312, pp. 1777–1780, June 2006. Publisher: American Association for the Advancement of Science.
- [34] B. B. Tierney and A. Grbic, “Designing Anisotropic, Inhomogeneous Metamaterial Devices Through Optimization,” *IEEE Transactions on Antennas and Propagation*, vol. 67, pp. 998–1009, Feb. 2019. Conference Name: IEEE Transactions on Antennas and Propagation.
- [35] F. Callewaert, S. Butun, Z. Li, and K. Aydin, “Inverse design of an ultra-compact broadband optical diode based on asymmetric spatial mode conversion,” *Scientific Reports*, vol. 6, p. 32577, Sept. 2016. Number: 1 Publisher: Nature Publishing Group.

- [36] E. Beaurepaire, J.-C. Merle, A. Daunois, and J.-Y. Bigot, “Ultrafast Spin Dynamics in Ferromagnetic Nickel,” *Physical Review Letters*, vol. 76, pp. 4250–4253, May 1996. Publisher: American Physical Society.
- [37] P. Scheid, Q. Remy, S. Lebègue, G. Malinowski, and S. Mangin, “Light induced ultrafast magnetization dynamics in metallic compounds,” *Journal of Magnetism and Magnetic Materials*, vol. 560, p. 169596, Oct. 2022.
- [38] B. Koopmans, G. Malinowski, F. Dalla Longa, D. Steiauf, M. Fähnle, T. Roth, M. Cinchetti, and M. Aeschlimann, “Explaining the paradoxical diversity of ultrafast laser-induced demagnetization,” *Nature Materials*, vol. 9, pp. 259–265, Mar. 2010. Number: 3 Publisher: Nature Publishing Group.
- [39] Z. Chen and L.-W. Wang, “Role of initial magnetic disorder: A time-dependent ab initio study of ultrafast demagnetization mechanisms,” *Science Advances*, vol. 5, p. eaau8000, June 2019. Publisher: American Association for the Advancement of Science.
- [40] J.-Y. Bigot, M. Vomir, and E. Beaurepaire, “Coherent ultrafast magnetism induced by femtosecond laser pulses,” *Nature Physics*, vol. 5, pp. 515–520, July 2009. Number: 7 Publisher: Nature Publishing Group.
- [41] C. Dornes, Y. Acremann, M. Savoini, M. Kubli, M. J. Neugebauer, E. Abreu, L. Huber, G. Lantz, C. a. F. Vaz, H. Lemke, E. M. Bothschafter, M. Porer, V. Esposito, L. Rettig, M. Buzzi, A. Alberca, Y. W. Windsor, P. Beaud, U. Staub, D. Zhu, S. Song, J. M. Glownia, and S. L. Johnson, “The ultrafast Einstein–de Haas effect,” *Nature*, vol. 565, pp. 209–212, Jan. 2019. Number: 7738 Publisher: Nature Publishing Group.
- [42] S. R. Tauchert, M. Volkov, D. Ehberger, D. Kazenwadel, M. Evers, H. Lange, A. Donges, A. Book, W. Kreuzpaintner, U. Nowak, and P. Baum, “Polarized phonons carry angular momentum in ultrafast demagnetization,” *Nature*, vol. 602, pp. 73–77, Feb. 2022. Number: 7895 Publisher: Nature Publishing Group.
- [43] S. L. Oliveira and S. C. Rand, “Intense Nonlinear Magnetic Dipole Radiation at Optical Frequencies: Molecular Scattering in a Dielectric Liquid,” *Physical Review Letters*, vol. 98, p. 093901, Feb. 2007. Publisher: American Physical Society.
- [44] S. C. Rand, W. M. Fisher, and S. L. Oliveira, “Optically induced magnetization in homogeneous, undoped dielectric media,” *JOSA B*, vol. 25, pp. 1106–1117, July 2008.
- [45] S. C. Rand, “Quantum theory of coherent transverse optical magnetism,” *JOSA B*, vol. 26, pp. B120–B129, Dec. 2009. Publisher: Optica Publishing Group.
- [46] W. M. Fisher and S. C. Rand, “Optically-induced charge separation and terahertz emission in unbiased dielectrics,” *Journal of Applied Physics*, vol. 109, p. 064903, Mar. 2011.
- [47] W. M. Fisher and S. C. Rand, “Light-induced dynamics in the Lorentz oscillator model with magnetic forces,” *Physical Review A*, vol. 82, p. 013802, July 2010. Publisher: American Physical Society.

- [48] A. A. Fisher, E. F. C. Dreyer, A. Chakrabarty, and S. C. Rand, “Optical magnetization, Part I: Experiments on radiant optical magnetization in solids,” *Optics Express*, vol. 24, pp. 26055–26063, Nov. 2016.
- [49] A. A. Fisher, E. F. C. Dreyer, A. Chakrabarty, and S. C. Rand, “Optical magnetization, Part II: Theory of induced optical magnetism,” *Optics Express*, vol. 24, pp. 26064–26079, Nov. 2016.
- [50] A. A. Fisher, E. F. Cloos, W. M. Fisher, and S. C. Rand, “Dynamic symmetry-breaking in a simple quantum model of magneto-electric rectification, optical magnetization, and harmonic generation,” *Optics Express*, vol. 22, pp. 2910–2924, Feb. 2014.
- [51] A. Einstein and W. J. de Haas, “Experimenteller Nachweis der Ampèreschen Molekularströme,” *Deutsche Physikalische Gesellschaft*, vol. 17, pp. 152–170, Jan. 1915. ADS Bibcode: 1915DPhyG..17..152E.
- [52] M. T. Trinh, K. Makhal, E. F. C. Dreyer, A. Shanker, S.-J. Yoon, J. Kim, and S. C. Rand, “Optical torque induces magnetism at the molecular level,” *Optics Express*, vol. 27, pp. 21295–21305, July 2019.
- [53] W. Fisher, *Transverse Optical Magnetism*. Ph.D. dissertation, University of Michigan, Ann Arbor, MI, 2012.
- [54] T. Jentsch, H. J. Juepner, K. W. Brzezinka, and A. Lau, “Efficiency of optical second harmonic generation from pentacene films of different morphology and structure,” *Thin Solid Films*, vol. 315, pp. 273–280, Mar. 1998.
- [55] H. Purwar, S. Idlahcen, C. Rozé, D. Sedarsky, and J.-B. Blaisot, “Collinear, two-color optical Kerr effect shutter for ultrafast time-resolved imaging,” *Optics Express*, vol. 22, pp. 15778–15790, June 2014. Publisher: Optica Publishing Group.
- [56] C. Yang, H. Tang, and G. Magnotti, “Picosecond Kerr-gated Raman spectroscopy for measurements in sooty and PAH rich hydrocarbon flames,” *Proceedings of the Combustion Institute*, vol. 38, pp. 1797–1804, Jan. 2021.
- [57] Z. Huang, W. Tan, J. Si, S. Zeng, Z. Kang, and X. Hou, “High-Transmittance Femtosecond Optical Kerr Gate with Double Gate Pulses Based on Birefringence Effect,” *Photonics*, vol. 9, p. 71, Feb. 2022. Number: 2 Publisher: Multidisciplinary Digital Publishing Institute.
- [58] M. C. Hoffmann, N. C. Brandt, H. Y. Hwang, K.-L. Yeh, and K. A. Nelson, “Terahertz Kerr effect,” *Applied Physics Letters*, vol. 95, p. 231105, Dec. 2009.
- [59] C. Jundt, G. Klein, B. Sipp, J. Le Moigne, M. Joucla, and A. A. Villaeys, “Exciton dynamics in pentacene thin films studied by pump-probe spectroscopy,” *Chemical Physics Letters*, vol. 241, pp. 84–88, July 1995.
- [60] K. Broch, J. Dieterle, F. Branchi, N. J. Hestand, Y. Olivier, H. Tamura, C. Cruz, V. M. Nichols, A. Hinderhofer, D. Beljonne, F. C. Spano, G. Cerullo, C. J. Bardeen, and F. Schreiber, “Robust singlet fission in pentacene thin films with tuned charge transfer interactions,” *Nature Communications*, vol. 9, p. 954, Mar. 2018. Number: 1 Publisher: Nature Publishing Group.

- [61] M. Pirotta, F. Gütter, H. Gygax, A. Renn, J. Sepiol, and U. P. Wild, “Single molecule spectroscopy. Fluorescence-lifetime measurements of pentacene in p-terphenyl,” *Chemical Physics Letters*, vol. 208, pp. 379–384, June 1993.
- [62] P. S. Pershan, “Nonlinear Optical Properties of Solids: Energy Considerations,” *Physical Review*, vol. 130, pp. 919–929, May 1963.
- [63] K. Y. Bliokh, Y. S. Kivshar, and F. Nori, “Magnetolectric Effects in Local Light-Matter Interactions,” *Physical Review Letters*, vol. 113, p. 033601, July 2014. Publisher: American Physical Society.
- [64] A. J.-T. Lou, E. F. C. Dreyer, S. C. Rand, and T. J. Marks, “Molecular Design Principles for Magneto-Electric Materials: All-Electric Susceptibilities Relevant to Optimal Molecular Chromophores,” *The Journal of Physical Chemistry C*, vol. 121, pp. 16491–16500, Aug. 2017.
- [65] Z. Chai, X. Hu, F. Wang, X. Niu, J. Xie, and Q. Gong, “Ultrafast All-Optical Switching,” *Advanced Optical Materials*, vol. 5, no. 7, p. 1600665, 2017. eprint: <https://onlinelibrary.wiley.com/doi/pdf/10.1002/adom.201600665>.
- [66] W. Yoshiki and T. Tanabe, “All-optical switching using Kerr effect in a silica toroid micro-cavity,” *Optics Express*, vol. 22, pp. 24332–24341, Oct. 2014. Publisher: Optica Publishing Group.
- [67] K. Nozaki, T. Tanabe, A. Shinya, S. Matsuo, T. Sato, H. Taniyama, and M. Notomi, “Sub-femtojoule all-optical switching using a photonic-crystal nanocavity,” *Nature Photonics*, vol. 4, pp. 477–483, July 2010. Number: 7 Publisher: Nature Publishing Group.
- [68] J. Hebling, G. Almási, I. Z. Kozma, and J. Kuhl, “Velocity matching by pulse front tilting for large-area THz-pulse generation,” *Optics Express*, vol. 10, pp. 1161–1166, Oct. 2002. Publisher: Optica Publishing Group.